Single Photon Avalanche Diodes for Visible Light Communication



Long Zhang

Jesus College

University of Oxford

A thesis submitted for the degree of

Doctor of Philosophy

Michaelmas 2018

Abstract

The visible light communication (VLC) system has been considered as an alternative indoor communication method for future networks. The VLC system requires highly sensitive receivers. At present, the best existing VLC receiver is based on the Avalanche photodiode (APD). However, the excess noise generated within the APD limits its sensitivity. The excess noise can be avoided by biasing the APD over its breakdown voltage to create a single photon avalanche diode (SPAD). It is expected that the SPAD can be used to develop the more sensitive VLC receiver.

At present, the sensitivity of the current SPADs is limited by several non-idealities, and the circumstances in which the SPADs should be preferred to APDs are still unclear. In this thesis, the first attempt at comparing the sensitivity of the SPAD-based receiver and the APD-based receiver has been presented. To figure out the criteria that determine a SPAD-based receiver is more sensitive than an APD-based receiver, analytical models for estimating the impact of the non-idealities on the SPAD-based receiver's sensitivity have been introduced and verified. Based on those validated models, appropriate guidelines for making a SPAD-based receiver superior to the APD-based receiver in the typical indoor environment are presented.

Pulse amplitude modulation (PAM) is potentially an attractive modulation scheme for the SPAD-based receiver to meet the demand for the high data rate due to its simplicity in the transmitter and receiver design. In

this thesis, the efficient ways of using the SPAD-based receiver to support PAM are investigated.

The SPAD arrays tested in this project are not optimised for the VLC application. Since SPADs are a relatively new technology, unlike APDs, the newly released product has significantly better characteristics than their predecessors. Based on the validated analytical models, it is estimated that the newly released SPAD arrays have the potential to support Gbps data rate with a higher sensitivity than the conventional APD in the typical indoor environment.

I would like to dedicate this thesis to my loving parents,

and wife.

Acknowledgements

First and foremost, I would like to express my sincere gratitude to my supervisor Professor Steve Collins for his continuously support, invaluable inspiration and patient guidance during my four years' research. I also would like to thank my co-supervisor Professor Dominic O'Brien, for giving me this opportunity to join this group and providing me with helpful suggestions and comments. A special thank to Professor Hyunchae Chun for his encouragement, patient and creative advices.

Meanwhile, I would also like to thank Dr. Sujan Rajbhandari and Graham Faulkner for their technical help and assistance. My sincere thanks also go to, Mr. Jinchuan Tang, Mr. Paramin PM Sangwongngam and Mr. Zubair Ahmed as well as other colleagues for the interesting discussions and sharing ideas.

Moreover, I would like to thank the China Scholarship Council (CSC) for awarding me the scholarship (No.201608060248) to fund my research and my living cost in the UK.

Publications

[1] Zhang, L., Chun, H.,Ahmed, Z., Faulkner, G., O'Brien, D., and Collins, S. The future prospects for SiPM based receivers for visible light communications. . *(* Journal of Lightwave Technology) (Under review).

[2] Zhang, L., Chitnis, D., Chun, H., Rajbhandari, S., Faulkner, G., O'Brien, D., and Collins, S. (2018). A Comparison of APD-and SPAD-Based Receivers for Visible Light Communications. *(* Journal of Lightwave Technology), 36(12), 2435-2442.

[3] Zhang, L., Chun, H., Faulkner, G., O'Brien, D., and Collins, S. (2018, February). Efficient pulse amplitude modulation for SPAD-based receivers. *LIFI Congress (GLC), 2018 Global* (pp. 1-5). IEEE.

[4] Zhang, L., Chun, H., Faulkner, G., O'Brien, D., and Collins, S. (2017, October). A comparison between the sensitivities of VLC receivers containing an off-the-shelf SPAD array and an APD. *Photonics Conference (IPC), 2017 IEEE* (pp. 27-28). IEEE.

[5] Chitnis, D., Zhang, L., Chun, H., Rajbhandari, S., Faulkner, G., O'Brien, D., and Collins, S. (2015, July). A 200 Mb/s VLC demonstration with a SPAD based receiver. *Summer Topicals Meeting Series (SUM), 2015* (pp. 226-227). IEEE.

Contents

1 Introduction **1**

1.1 Motivation 1

1.2 Project Summary 3

1.3 Dissertation Organization 3

2 Background of using SPADs for VLC **6**

2.1 Introduction 6

2.2 Visible Light Communication system 6

2.3 Indoor VLC channel model 7

2.4 Motivation of using SPADs as a VLC receiver 10

2.5 Single Photon Avalanche Diodes 14

2.6 State-of-the-art SPADs for VLC 17

3 A comparison of APD and small SPAD-based receivers **20**

3.1 Introduction 20

3.2 Transmitter characterisation 21

3.3 The tested SPAD array 24

3.4 Nonlinear model of the active quenched SPAD 25

3.5 SPAD OOK measurement result 29

3.5.1 Eye diagram 29

3.5.2 Effect of dead time 30

3.5.3 Effect of ISI . . . 31
3.5.4 Effect of ambient light . . . 32
3.6 APD OOK measurement result . . . 37
3.7 Summary . . . 41

4 Performance of larger SPAD array 43
4.1 Introduction . . . 43
4.2 Photon counting methods . . . 44
4.2.1 Peak counting method . . . 45
4.2.2 Summation method . . . 47
4.2.3 Edge counting method . . . 49
4.2.4 Evaluation of the photon counting methods . . . 50
4.3 Comparison between Photon counting mode and Analogue mode . . . 53
4.4 OOK link results using an MPPC . . . 56
4.5 Sensitivity improvement by increasing PDE . . . 60
4.6 Summary . . . 65

5 4-PAM VLC with a SPAD-based receiver 67
5.1 Introduction . . . 67
5.2 Numerical model of 4-PAM . . . 68
5.2.1 Comparison between Gray Code and Binary Code . . . 69
5.2.2 Strategy to determine the optimum 4-PAM symbol levels . . . 70
5.2.3 Impact of background count on 4-PAM . . . 73
5.2.4 Comparison between Poisson model and Gaussian model . . . 76
5.3 A practical method to estimate the optimum 4-PAM symbol levels . . . 77
5.4 200 Mbps demonstration using 4-PAM . . . 83
5.4.1 Feasibility check . . . 84
5.4.2 Method to search 4-PAM symbol level . . . 97

5.4.3 Experimental results 98
5.5 Summary 101

6 Future Prospects of SPAD-based VLC receiver 103
6.1 Introduction 103
6.2 Estimated background counts from ambient light 104
6.3 Impact of dead time and pulse time 106
6.4 A general method to estimate the sensitivity of a given SPAD array . 109
6.5 Estimation results for OOK 111
6.6 Potential of supporting M-PAM 118
6.7 Summary 122

7 Conclusion and Future work 124
7.1 Conclusion 124
7.2 Future Work 129

References 137

List of Figures

2.1 A typical VLC link 7

2.2 VLC link configurations 8

2.3 Directed LOS link configuration 9

2.4 APD avalanche multiplication process 13

2.5 The I-V characteristic of the SPAD 14

2.6 Basic diagram of passive quenching and active quenching 15

2.7 Fill factor 16

2.8 Effect of dead time illustration 17

3.1 The modulation bandwidth of the tested RCLED (RC650-TO46FW) at different bias voltages 21

3.2 The measured operating range of the tested RCLED (RC650-TO46FW) 22

3.3 Measured frequency response of the tested RCLED (RC650-TO46FW) at the bias voltage of 1.3V fitted with the general LED model 23

3.4 Eye openings at different data rates when the RCLED bandwidth is 100 MHz 24

3.5 Simplified schematic for the tested SPAD array 24

3.6 The measured average number of counts as a function of the product of the intensity of the light falling on the SPAD array and the SPAD dead time for four different dead times. 28

3.7 Experimental set-up for the OOK link test. 30
3.8 A raw eye diagram at a data rate of 100Mbps when the BER is 7.9×10^{-4} 31
3.9 The measured BER at different dead times for a data rate of 100 Mbps, 50 Mbps and 17.9 Mbps. In each case the lowest BER is achieved for a dead time which is slightly shorter than the bit time. 32
3.10 The measured histograms of the number of SPADs that have fired within a dead time of the end of each bit period when the bit time is 10 ns, the dead time is 8.8 ns and the measured BER is 7.9×10^{-4}. . 33
3.11 Photon counts per bit required to maintain different target BERs at different background counts, the dashed line is calculated based on Gaussian model and the solid line is calculated based on Poisson model 34
3.12 Fractional error of the Gaussian model. 36
3.13 The signal penalty required for the SPAD to achieve a BER of 7.9×10^{-4} at different background light levels, shown in both $\mathrm{mW/m^2}$ (bottom x-axis) and lux (top x-axis), for 100 Mbps when equalization has been used to reduce ISI. 36
3.14 The measured BER of an APD-based VLC receiver at different bias voltages in the dark with a signal light intensity of 3.44 $\mathrm{mW/m^2}$. . . . 38
3.15 The required signal penalty for the tested APD to achieve a BER of 7.9×10^{-4} at various background light intensities. In this figure the data (stars) is compared to the predictions of equation 3.26. 40

4.1 The block diagram and key parameters of MPPC module C11209-110. 44
4.2 Output signal of the MPPC module from low light levels to high light levels. 44
4.3 Output signal from the MPPC module measured in the dark within 1 ms. There are 200 pulses within this period counted by hand. 45
4.4 Distribution of peak values within the captured signal shown in figure 4.3. 46

4.5 Distribution of a sum of single pulse amplitude over single pulse time (10 ns) generated from the data in figure 4.3. 48
4.6 The blue curve is the output signal from the MPPC module measured in the dark and the red curve refers to the difference between the adjacent samples within the received signal. 50
4.7 Distribution of the peak heights in $D[i]$ which is calculated using equation (4.3) based on the captured signal shown in figure 4.3. 51
4.8 a) Lower boundary of two SPADs fired b) Upper boundary of one SPAD fired where the blue curves are the original signal $S[i]$ and the red curve are the $D[i]$. 51
4.9 Performance evaluation of three photon counting methods at different light levels 52
4.10 Comparison between the photon counting mode and analogue mode at different data rates measured in the dark. 55
4.11 The transmitter signal intensity required to achieve a BER of 7.9×10^{-4} at different data rates in the dark when the MPPC module is used as the receiver. In the figure, the red curve refers to the signal intensities measured without using EQ, the green curve refers to the signal intensities measured after using EQ, the solid blue curve refers to the calculated signal intensity based on Poisson distribution when dark counts are considered and the dashed blue curve refers to the calculated signal intensity based on Poisson distribution without considering dark counts. 56
4.12 The impact of DCR accessed by the ratio between the signal counts required with and without dark counts at different data rates. 57

4.13 The required signal penalty for the MPPC to achieve a BER of 7.9×10^{-4} at various background light intensities. In this figure the data (stars) is compared to the predictions of equation (2.8). 58
4.14 The estimated signal intensities required by the tested APD-based receiver and receivers including MPPC to achieve the target BER at different intensities of background light. 60
4.15 APD noise power analyses at different background light intensities. . 61
4.16 Correction factor required to compensate the Q parameter calculated by equation (3.19). This figure is obtained using data in figure 3.11 at the BER of 10^{-3}. 62
4.17 The estimated signal intensities required by the tested APD-based receiver and receivers including MPPCs with different PDEs to achieve the target BER at different background light intensities. 64

5.1 BER differences between using Gray Code and Binary Code at the same symbol levels arrangement when background count is 1. 70
5.2 Signal levels arrangement to achieve a target BER of 10^{-3} when background count equals to 1.The dashed lines are the optimum signal levels based on comprehensive search. The solid lines refer to the signal levels which ensure errors are evenly distributed. 71
5.3 Signal levels change against background counts to achieve a BER of 10^{-3}. 74
5.4 Averaged photon counts per bit required to maintain different target BERs at different background counts 75
5.5 Photon counts per bit required to maintain different target BERs at different background counts, the dashed line is calculated based on Gaussian model equation (5.5) to (5.8), and the solid line is calculated based on Poisson model equation (5.2) and (5.4). 77

5.6 Fractional error of the Gaussian model equation (5.5) to (5.8). 78
5.7 Signal intensities required by the tested MPPC module to generate level 3 at different data rates to achieve the target BER of 10^{-3} in the dark when errors are evenly distributed. 79
5.8 The histograms of measured counts per symbol for the 3 signal symbol levels of 4-PAM when a BER of 10^{-3} is achieved in the dark with the data being Gray coded. 82
5.9 A comparison between the number of counts in 1 μs at 0.4 $\mathrm{mW/m^2}$ and three possible mathematical models. 83
5.10 Operating range measurement result of the tested MPPC module. . . 85
5.11 The effect of paralyzable dead time and non-paralyzable dead time. Photon arrived within the paralyzable dead time is not only missed but also restarts the dead time. Photons arrived within the non-paralyzable dead time are lost and there is on restarting of the dead time [50]. . . 86
5.12 The nonlinear response of the tested MPPC module with models fit assuming dead time equals to the pulse time of the C11209-110 module (10 ns). The red spots are calculated using the ratio 1000 counts/V and data in figure 5.10 90
5.13 The measured nonlinear response of the tested MPPC module with different model fit. 92
5.14 Comparision between the hybrid dead time model and the paralyzable dead time model. 92
5.15 The distributions of received 4-PAM symbol 1 after different received 4-PAM symbols measured at a 200 Mbps 4-PAM link in the dark before equalisation. 93
5.16 Block diagram of the tested MPPC module based 4-PAM system used for Monte Carlo simulation. 94

5.17 The ISI Power Penalty required at different RCLED bandwidth using 4-PAM at a data rate of 200 Mbps. 96
5.18 Method to search the 4-PAM symbol level. 97
5.19 Eye diagram of 200 Mbps 4-PAM link operated in the dark with a BER of 10^{-3} before equalisation. 99
5.20 Eye diagram of 200 Mbps 4-PAM link operated in the dark and in the 500 lux ambient light with a BER of 10^{-3} after equalisation. 99

6.1 The density of background photons per second measured by a 1 mm^2 detector from different lighting sources at 500 lux condition. 105
6.2 The estimated extra power needed to employ DFE when the symbol rate is higher than bandwidth of the SPAD array. 108
6.3 A general method to estimate the sensitivity of a given SPAD array. . 109
6.4 Signal intensities required by the SPAD arrays in table 1 in Appendix B to achieve a BER of 10^{-3} in the 500 lux ambient light condition at different data rates. 111
6.5 Signal intensities required by the SPAD arrays with the 36 mm^2 active area in table 1 in Appendix B to achieve a BER of 10^{-3} in the 500 lux ambient light condition at different data rates. 113
6.6 Effective PDP of the SPAD arrays with 36 mm^2 active area at different data rates. 114
6.7 Signal intensities required by the SPAD arrays with the 36 mm^2 active area in table 1 in Appendix B to achieve a BER of 10^{-3} in the 500 lux ambient light condition below 50 Mbps. 115

6.8 Signal intensities required by the S13360-6025CS and SensL B 60036 within higher ambient light conditions to achieve a target BER at different data rates. The symbol N_b in this figure refers to the averaged background counts generated in the 500 lux ambient light condition at a wavelength of 400 nm and the number in the legend refers to N times the averaged background counts generated in the 500 lux ambient light condition at a wavelength of 400 nm. 117
6.9 The data rate can be achieved by S13360-6025CS to get the target BER of 10^{-3} at different background conditions using OOK. The x-axis refers to the K times the averaged background counts generated in the 500 lux ambient light condition at a wavelength of 400 nm. . . 118
6.10 The highest signal level for different levels of PAM. 119
6.11 Operating range of S13360-6025CS. 120
6.12 The method used to estimate background counts per symbol detected by a particular SPAD array. 121
6.13 The number of background counts per symbol detected by S13360-6025CS at different background conditions using 4-PAM. The x-axis refers to the K times the averaged background counts generated in the 500 lux ambient light condition at a wavelength of 400 nm. 122

List of Tables

2.1 The minimum number of photons per bit required by ideal photodetector to achieve different BERs in the dark. 12

2.2 Recent demonstration based on the SPAD-based receiver. 19

3.1 Summary of key parameters of the tested SPAD array. 25

3.2 Summary of key parameters of the tested APD. 40

5.1 Gray Code vs Binary Code. 68

5.2 Total SER distribution between signal levels in figure 5.2. 72

5.3 Comparison between different signal level arrangements. 73

5.4 The searched power levels for generating 4-PAM symbols and the corresponding applied voltages used in the completed 4-PAM test. 80

5.5 A comparison between the predicted number of detected photons per symbol needed to achieve the target BER of 10^{-3} and experimental results with 0.2 counts per symbol due to dark counts. 81

5.6 A comparison between the estimated number of detected photons per symbol needed to achieve the target BER of 10^{-3} and experimental results. 84

5.7 Comparisons between measured 4-PAM symbol levels with estimated values in the dark. 100

5.8 Comparisons between measured 4-PAM symbol levels with estimated values at 500 lux. 100

6.1 Fitting parameters used in figure 6.2. 109

6.2 A list of newly released SPAD arrays with 36 mm^2 active area 113

B.1 A list of newly released SPAD arrays with better PDE than the tested MPPC 134

List of Acronyms

APD	Avalanche photodiode
AC	Alternating current
AWG	Arbitrary waveform generator
BER	Bit error rate
CSK	Color shift keying
CDF	Cumulative distribution function
CPS	Counts per second
DCR	Dark count rate
DC	Direct current
DFE	Decision feedback equalisation
EQ	Equalisation
EO	Eye opening
FF	Fill factor
FOV	Field of view
FEC	Forward error correction

Gbps	Gigabits per second
IC	Integrated circuit
ISI	Intersymbol interference
LPF	Low pass filtering
LED	Light emitting diode
MPPC	Multi-pixel photon counter
Mbps	Megabits per second
NLOS	None line of sight
ND	Neutral density
OFDM	Orthogonal frequency division multiplexing
OOK	On-off keying
PD	Photodiode
PMT	Photomultiplier tube
PDF	Probability denstiy function
PDP	Photon detection probability
PDE	Photon detection efficiency
PRBS	Pseudorandom binary sequence
PAM	Pulse amplitude modulation
QE	Quantum efficiency
RF	Radio frequency

SNR	Signal to niose ratio
SER	Symbol error rate
SPAD	Single photon avalanche diode
TIA	Transimpedance amplifier
VLC	Visible light communication

Chapter 1

Introduction

1.1 Motivation

Wireless services and applications have become an essential part of human's life. Due to the dramatically increasing demand for wireless services and applications, the global mobile data traffic has been increased 10-fold in the past ten years [1] and is expected to be increased by 8-fold in the next five years [2]. It has been estimated that the capacity of the existing wireless network will not be able to meet user's demand after 2020 [3]. More bandwidth is required to improve the capacity of the wireless network further. Radio frequency (RF) spectrum is a limited resource. Due to the explosive growth in wireless services and applications, the RF spectrum is nearly exhausted [3]. New spectrum is required to support the extended wireless capacity.

Visible light communications (VLC) that use the unlicensed spectral bands (380 nm-780 nm) have drawn significant attention in recent years. Compared to the traditional RF system, the main advantages of VLC are (1) using the unlicensed band, (2) ensuring high transmission security, and (3) using simple front-end devices [4, 5]. The potential applications that use VLC includes a) secure communication since light cannot propagate through walls and objectives b) the wireless communication system

deployed in RF signal prohibited or limited scenarios such as hospital, down-hole, oil field, underwater, etc. [4,6–8] c) high speed indoor communication which has already been demonstrated that using complexed modulation schemes the indoor VLC system can offer Gbps data rate. [9–11]. Since more than 70% of all the mobile traffic occurs indoors, there is a significant demand for using VLC to offload indoor mobile traffic within the future network [12]. Naturally, the most attractive application of VLC is for indoor communication.

In practical indoor VLC system deployment, the maximum optical power that is allowed to be transmitted is required to fulfill the eye-safe limit, the indoor illumination regulation and also the comfort of users [13]. As a result, the sensitivity of the receiver ultimately determines the maximum VLC system's data rate and transmission distance. So far, the most sensitive VLC receiver is based on the APD which exploits avalanche multiplication to create internal gain [14,15]. Unfortunately, avalanche multiplication generates excess noise that limits the maximum useful APD gain. SPADs are an array of APDs that are operated in Geiger mode. In this mode, the SPADs do not generate excess noise and are capable of detecting individual photons [16,17]. It is anticipated that a SPAD-based VLC receiver will require less optical power than an APD-based receiver to support a given data rate with a particular bit error rate (BER).

Although the SPADs are anticipated to be more sensitive than APDs, there are several non-idealities within the current SPADs that limit the SPAD-based receiver's sensitivity. First of all, the current SPADs have small active area and low Photon detection efficiency (PDE) due to the low fill factor when the SPADs are fabricated into arrays. Secondly, the current SPADs suffer from the impact of dead time. After a photon is detected, the SPAD will be blind for a particular duration (known as dead time). Thirdly, the high sensitivity makes the SPADs to be more susceptible to the ambient light. These are complex effects to analyse, and at present the circumstances

in which SPADs should be preferred to APDs are unclear. Additionally, the APD-based receiver is capable of supporting Gbps data rate [10, 11]. Therefore, to match the APD's performance, the SPAD-based receiver is required to offer Gbps data rate. One potential approach to increase the data rate is to use complex modulation schemes. PAM is an attractive modulation scheme in VLC due to the simplicity in the transmitter and receiver design [14]. However, at present, the efficient way of using SPADs to support PAM has not been determined.

1.2 Project Summary

The objective of this research project is to determine the appropriate SPAD-based receiver design guidelines for making the SPAD-based VLC receiver superior to the APD-based VLC receiver in the typical indoor environment. The research focuses on developing analytical models to estimate the impact of dead time, active area, PDE and background counts to the SPAD-based receiver (which can be used to determine the criteria that a SPAD-based receiver is more sensitive than an APD-based receiver), investigating a method of efficiently use SPADs to support PAM, and estimating the potential to achieve a data rate of 1 Gbps or even higher with a SPAD-based receiver in the typical indoor environment.

1.3 Dissertation Organization

The outline of this dissertation is described below. Note that, all nomenclatures and mathematical notations are independently defined and used in each chapter for clarity.

Chapter 2 contains the necessary background information needed to investigate using SPADs for VLC. This chapter briefly describes the typical configuration of VLC systems and the indoor VLC channel, analysis the ideal photodetector's performance,

the limitation in APDs, the physics behind SPAD operation, the motivation of using a SPAD array and reviews the recent research achievements of using SPAD-based receiver for VLC.

Chapter 3 compares the sensitivity of a small SPAD array with a typical APD. This chapter begins with a characterization of a small SPAD array with a variable dead time. A general model to estimate the output response from the active quenched SPAD array is built according to the characterization result. Then this chapter presents a detailed comparison between two analytical models which can be used to estimate the bit error rate (BER) performance of using SPADs, and demonstrates the link performance of using that small SPAD array. The sensitivity of that small SPAD array is then compared to a typical APD.

Chapter 4 evaluates the performance of receivers containing a large SPAD array. This chapter discusses two methods to process the output signal from that large SPAD array, verifies the analytical models presented in chapter 3 and compares the sensitivity of that large SPAD array with the tested APD both in the dark and in the typical ambient light condition. Based on the verified analytical models, a criterion that determines a SPAD-based receiver is more sensitive than an APD-based receiver in the typical indoor environment is presented.

Chapter 5 investigates an efficient way of using a SPAD-based receiver to support 4-PAM. It first discusses the optimum strategy for setting the 4-PAM symbol levels and thresholds. Based on the optimum strategy, a practical estimation method is then presented to estimate the actual 4-PAM power levels required to achieve a target BER. This practical method is verified at low data rate. In order to support 4-PAM at high symbol rate, the operating range of the tested SPAD array is checked. Based on the measured operating range of the SPAD array, a general model for expressing the output response from the passive quenched SPAD array is presented. Due to the limited pulse time of the tested SPAD array, the intersymbol interference (ISI) occurs

when the symbol rate is high. A method to estimate the power penalty required to compensate ISI by decision feedback equalisation (DFE) is presented. At the end of this chapter, a 200 Mbps data rate is demonstrated with a SPAD-based receiver using 4-PAM both in the dark and in the typical indoor ambient light condition, and the corresponding sensitivities are reported. Moreover, the accuracy of the estimated ISI power penalty is checked by the measurement result.

Chapter 6 estimates the potential of using a receiver with better SPADs to achieve a data rate of 1 Gbps or even higher with a sensitivity higher than the typical APD in the typical indoor lighting environment. In this chapter, a general method based on the validated models obtained in previous chapters is introduced to estimate the sensitivity of a particular SPAD array at the different data rates. This method is then used to estimate the feasibility of using a list of newly released SPADs with a higher PDE than the tested MPPC, to offer the Gbps data rate with a sensitivity higher than the typical APD, in the typical indoor environment.

Chapter 7 summaries the key conclusions in this thesis and discusses the future work.

Chapter 2

Background of using SPADs for VLC

2.1 Introduction

This chapter begins with a brief description of the VLC system and the indoor VLC link model. Then the motivation for using SPADs to replace APD as the VLC receiver is explained, include introducing the sensitivity of ideal photodetector, presenting the limitation in APDs and the principle of SPADs. Finally, a review of the recent research achievement in using SPADs for VLC is described.

2.2 Visible Light Communication system

A typical VLC link is illustrated in figure 2.1. At the transmitter, the modulated analogue signal drives the light source to emit the optical signal. The performance of the VLC link is affected by the ambient light which arises from sources including, sunlight, incandescent and fluorescent lighting [18]. To attenuate the ambient light, at the receiver, an aperture is required to narrow the field of view (FOV) so that the ambient light incident out of the FOV can be avoided, and an optical filter

is required to eliminate the signal at unwanted wavelengths and pass through the desired transmitted signal. In order to collect sufficient incident light, a concentrator may be placed before the photodetector. The received optical signal is then converted to the electrical signal by the photodetector according to the incident light intensity.

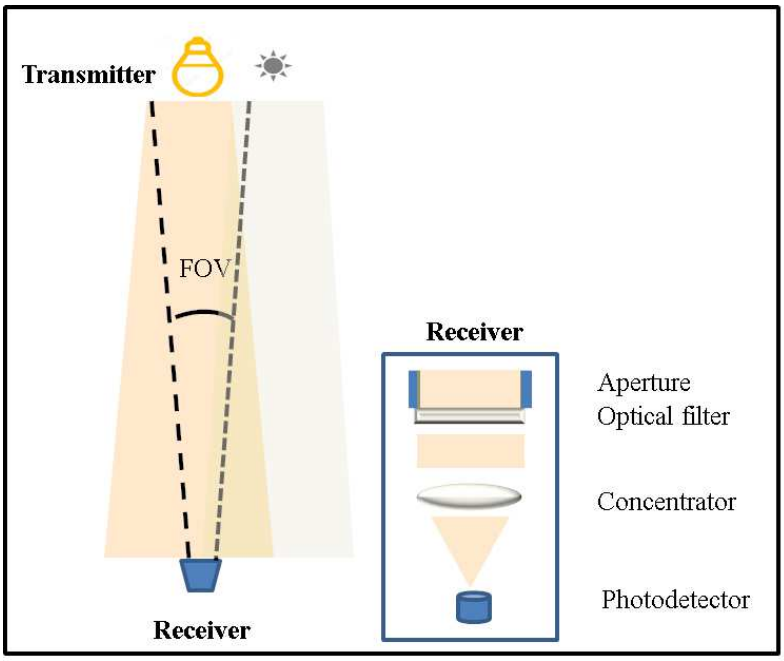


Figure 2.1: A typical VLC link.

2.3 Indoor VLC channel model

Based on the location and directionality of the transmitter and the receiver, the commonly used indoor VLC link configurations can be categorized as the directed line of sight(LOS), non-directed LOS, directed non-line of sight (NLOS), non-directed NLOS, hybrid LOS, and hybrid NLOS [19].

The corresponding link configurations are illustrated in figure 2.2. For the directed LOS link (figure 2.2a), both the transmitter and the receiver have a very narrow FOV. As a result, this configuration achieves a high received light intensity at the receiver and can efficiently reduce the ambient light. Furthermore, this configuration does

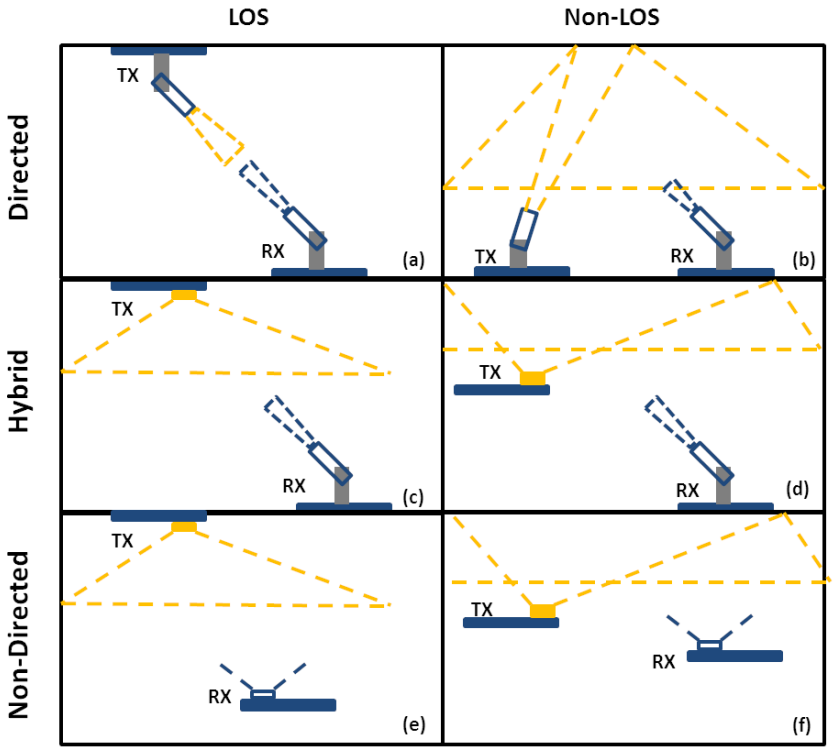


Figure 2.2: VLC link configurations [19].

not suffer from multipath dispersion [20]. However, because the transmitter and receiver have to be accurately aligned, the directed LOS link has a limited coverage area and mobility [19]. The directed NLOS (figure 2.2b) link and the hybrid link configurations (figure 2.2c-d) are the potential solutions to increase the mobility of the system. For the directed NLOS link and the hybrid links, in order to achieve the mobility, a tracking mechanism is still required at the receiver to appropriatly align the receiver with the transmitted beam. However, at present, the current tracking system is not convenient to be integrated into the portable mobile devices [19]. To avoid using tracking system, the non-directed link configuration was proposed [19]. For the non-directed NLOS link configuration (figure 2.2f), both the transmitter and the receiver have a wide FOV and hence the transmitter and the receiver do not have to be accurately aligned. Therefore, this configuration is more robust to the link blocking and can achieve high system mobility [4]. However, the non-directed

NLOS link configuration suffers from multipath dispersion and introduces the ISI, which limits the maximum achievable data rate [20]. A compromise configuration is the non-directed LOS link (figure 2.2e). However, this link configuration still requires a LOS path and still has to tolerate a small amount of multipath dispersion [19].

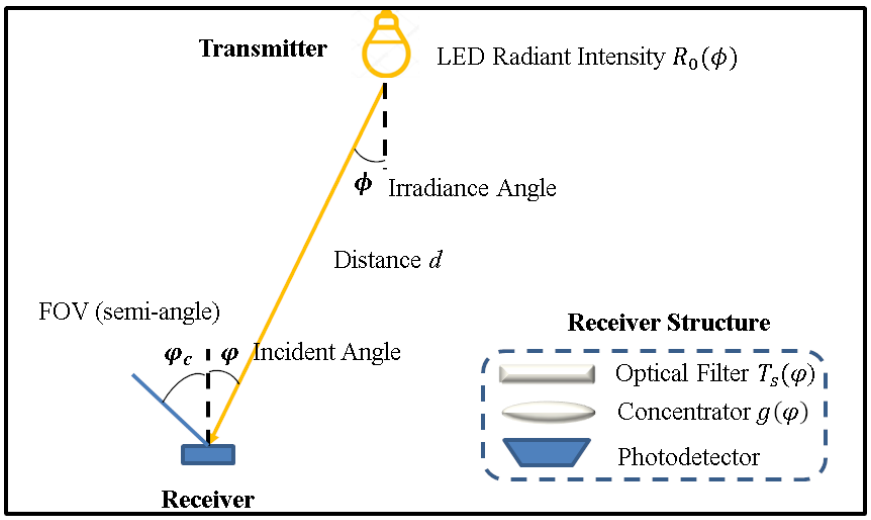


Figure 2.3: Directed LOS link configuration.

To simplify the study, the directed LOS link configuration is considered in this project. Figure 2.3 shows the channel model of the directed LOS link. The DC gain of the LOS channel is expressed as [19]

$$H_{LOS}(0) = \begin{cases} \frac{A}{d^2} \times R_0(\phi) T_s(\varphi) g(\varphi) \cos(\varphi), & \text{if } 0 < \varphi \leq \varphi_c \\ 0, & \text{if } \varphi > \varphi_c \end{cases} \tag{2.1}$$

where A is the detector area, d is the distance between the transmitter and the receiver, $R_0(\phi)$ is the Lambertian radiant intensity, $T_s(\varphi)$ is the optical filter gain, $g(\varphi)$ is the concentrator gain, ϕ is the angle of radiance, φ is the incident angle , φ_c is the FOV of the receiver. $R_0(\phi)$ is given by

$$R_0(\phi) = \frac{m+1}{2\pi} \cos^m(\phi), \qquad \phi \in [-\frac{\pi}{2}, \frac{\pi}{2}] \tag{2.2}$$

where m is the order of Lambertian emission given by

$$m = \frac{-\ln 2}{\ln(\cos(\phi_{\frac{1}{2}}))} \tag{2.3}$$

$\phi_{\frac{1}{2}}$ is the semiangle at half-power of the transmitter. For the indoor short range directed LOS channel, the multipath dispersion is negligible [20] and hence the channel response is non-frequency selective. As a result, the impulse response for the directed LOS channel is given by [20]

$$h(t) = H_{LOS}(0) \times \delta(t) \tag{2.4}$$

where $\delta(t)$ is the Dirac delta function.

2.4 Motivation of using SPADs as a VLC receiver

A VLC system requires high sensitive photodetector. The sensitivity of a VLC photodetector is defined as the minimum optical power required to achieve a given bit error rate (BER) [15]. In an on-off keying (OOK) system, the BER is defined as [21]

$$\text{BER} = P(0)P(1\,|0\,) + P(1)P(0\,|1\,) \tag{2.5}$$

where $P(0)$ and $P(1)$ are the probability of bit 0 and bit 1 being transmitted, $P(1|0)$ is the probability of receiving bit 1 when bit 0 is transmitted and $P(0|1)$ is the probability of receiving bit 0 when bit 1 is transmitted. When $P(1) = P(0) = 1/2$, equation (2.5) can be expressed as

$$\text{BER} = \frac{1}{2}[P(1\,|0\,) + P(0\,|1\,)] \tag{2.6}$$

An ideal photodetector is defined as a photodetecor which has no thermal noise,

no dark count, infinite bandwidth and 100% quantum efficiency [15]. The probability of k photons are detected within a bit slot by an ideal photodetector follows the Poisson distribution [15] which is given below

$$P(k) = \frac{N^k e^{-N}}{k!} \tag{2.7}$$

where N is the averaged number of detected photons within a bit slot.

Based on equation (2.7), the error probability of an ideal photodetector is given by [22]

$$\text{BER} = \frac{1}{2} \sum_{k=n_T+1}^{\infty} \frac{(N_0)^k}{k!} e^{-N_0} + \frac{1}{2} \sum_{0}^{k=n_T} \frac{(N_0 + N_1)^k}{k!} e^{-(N_0+N_1)} \tag{2.8}$$

where N_1 is the average number of detected signal photons per bit when bit 1 is transmitted, N_0 is the average number of background counts per bit and n_T refers to the optimum decision threshold [22]. When the ideal VLC photodetector is operated in the completely dark condition, if the transmitter is fully off at bit 0, no photon can be detected at bit 0 (N_0=0). As a result, the first term in equation (2.8) equals 0 which indicates that bit 0 is always correctly decoded. Correspondingly, the optimum decision threshold n_T is required to be set to 0 so that the second term in equation (2.8) is the minimum which gives the minimum BER. In this case, the BER is totally determined by the probability that no photon is detected when bit 1 is transmitted [23]. Based on equation (2.8), with N_0=0 and n_T=0, the BER for an ideal photodetector is given by

$$\text{BER} = \frac{1}{2} e^{-N_P} \tag{2.9}$$

Based on equation (2.9), at a given target BER, N_P can be solved by

$$N_P = -\ln(2 \times \text{BER}) \tag{2.10}$$

Equation (2.10) is known as the Poisson limit which determines the minimum number of photons per bit required to achieve a given BER using an ideal photodetector [23]. Table 2.1 shows the Poisson limit at different BERs calculated by equation (2.10). It can be seen that, in the dark, only 6.2 photons per bit are required by the ideal photodetector to achieve the target BER of 10^{-3} which is the BER limit that the Forward Error Correction (FEC) required [4].

BER	Photons per bit
10^{-3}	6.2
10^{-4}	8.5
10^{-5}	10.8
10^{-6}	13.1
10^{-7}	15.4
10^{-8}	17.7
10^{-9}	20

Table 2.1: The minimum number of photons per bit required by ideal photodetector to achieve different BERs in the dark.

The best existing VLC photodetector is the APD [14]. The bias voltage across the APD is close to the breakdown voltage. The physics behind the APD operation is illustrated in figure 2.4 [15]. When an incident photon is absorbed by the depletion region, it generates an electron-hole pair. The generated electron is then accelerated by a strong electric field within the multiplication region and gets sufficient energy. Once this accelerated electron collides with the lattice in multiplication region, a new electronhole pair is generated. Then the new generated electron and the primary electron are both accelerated within multiplication region and collided with the lattice again to generate more electron-hole pairs. This multiplication process significantly

increases the number of electron-hole pairs and hence generates the avalanche photocurrent. The multiplication gain is determined by the bias voltage. A higher bias voltage results in a higher gain. However, this multiplication process is a random process and generated a gain dependant excess noise. The excess factor $F(M)$ is expressed as

$$F(M) = kM + (1 - k) \times (2 - \frac{1}{M}) \tag{2.11}$$

where M is the average multiplication gain and k is the ionization ratio. Since increasing the multiplication gain of the APD will increase the desired photocurrent as well as the excess noise, there is an optimum APD gain to achieve the highest signal to noise ratio (SNR). For typical APDs, to get a BER of 10^{-9}, it requires more than 1000 photons per bit [24] which is at least 50 times more than the Poisson limit calculated by equation (2.10). This substantial performance gap offers a huge opportunity for the SPAD to replace the APD in the current VLC receiver.

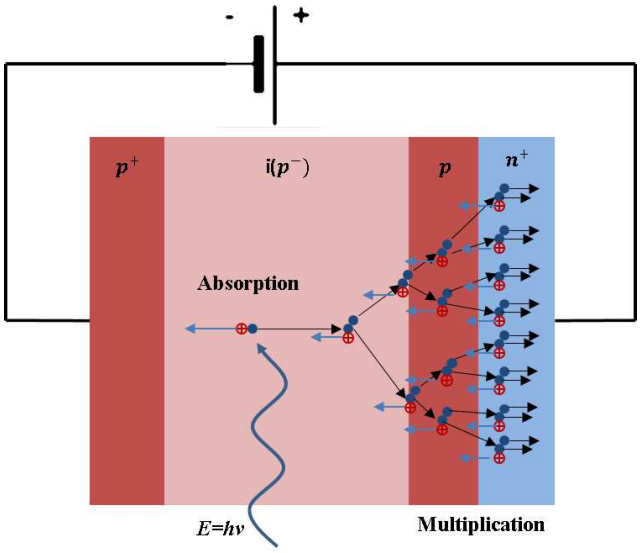


Figure 2.4: APD avalanche multiplication process.

2.5 Single Photon Avalanche Diodes

The sensitivity of the APD is limited by the excess noise [22, 25]. The the excess noise can be avoided by reversing bias the APD over its breakdown voltage to create a SPAD [22]. The gain of a SPAD is larger than 10,000 [25]. Comparing with the existing APDs, it is anticipated that, the SPAD-based VLC receiver requires less optical power to achieve a given BER. The SPADs are manufactured using the same process as consumer ICs [23], and hence the SPAD-based receiver is convenient for integration into consumer electronics.

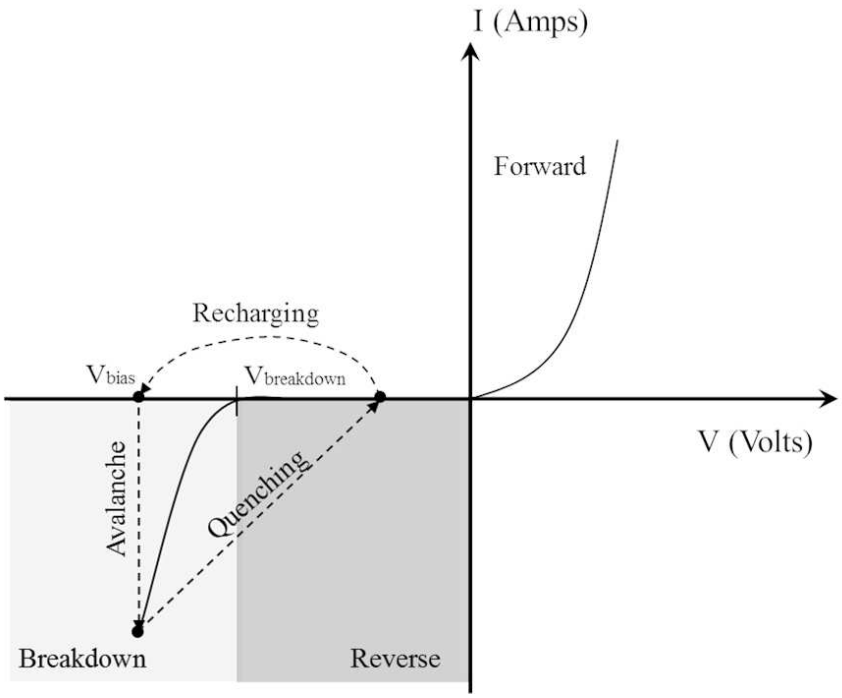


Figure 2.5: The I-V characteristic of the SPAD.

The simple schematic of the SPAD circuit and the I-V characteristic of the SPAD are shown in figure 2.5 [26]. Once a single photon is detected, a self-sustained avalanche current is generated. This self-sustained avalanche current passing through the SPAD is quenched by the external quenching circuit. The quenching circuit reduces the bias voltage across the SPAD below the breakdown voltage and hence terminates the self-sustained avalanche process. After the SPAD is quenched, it is

then recharged back to its initial state to prepare for the next photon detection. This whole quenching process takes a finite time which is known as the dead time. During the dead time, the SPAD is inactive, and no photon can be detected.

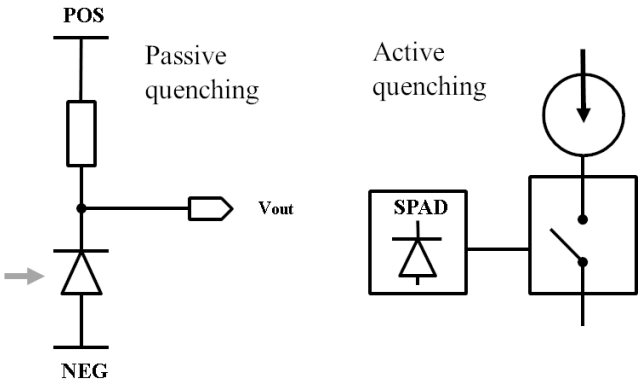


Figure 2.6: Basic diagram of passive quenching and active quenching.

There are two types of quenching circuits, passive quenching circuit, and active quenching circuit [23], which are shown in figure 2.6. Passive quenching circuit is implemented using a simple circuit such as a resistor in series with the SPAD. Active quenching circuit is implemented using the more sophisticated active circuit. Compared to passive quenching, SPAD with active quenching has a shorter dead time [23] but is more complicated to manufacture.

The impact of dead time can be mitigated by an array of SPADs as all the SPADs within an array are unlikely to be inactive at the same time. There are two approaches to combine the outputs of the SPADs within an array. For the digital approach, each SPAD cell has a dedicated counter to count the detected avalanche events and the counts from individual SPAD cell are then added together [23]. For analogue approach, the output currents from each SPAD cell are aggregated together at the common output [23]. Compare to the digital SPAD array, the analogue SPAD array is more easily produced and already commercially available [27]. At present, the primary application of the SPAD array is for low light level detection includes medical imaging [28, 29], distance ranging [30–32] and so on.

The metrics, PDE, dead time and background counts, will affect the system's performance when the SPAD array is used in a receiver. The PDE is the metric that determines the number of photons can be detected with a given number of incident photons at the total detector area of the detector [33]. It is expressed as

$$PDE = PDP \times FF \tag{2.12}$$

In equation (2.12), term PDP is the photon detection probability which is the probability that an incident photon impinge the active area of the SPAD generates an avalanche event. PDP is determined by the bias voltage of the SPAD, the operation wavelength and the material to make the SPAD [34]. FF refers to the fill factor of the SPAD which is the ratio of the active area to the total detector area [35]. A receiver that incorporates SPADs that have higher PDE will be more sensitive to the optical signal and also to the ambient light noise.

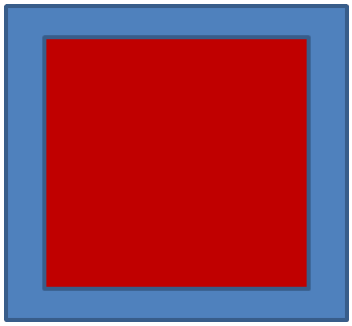


Figure 2.7: Fill factor.

After generating the avalanche process, the SPAD will be inactive during dead time. Consequently, dead time determines the operating range of the SPAD-based receiver. For the active quenched SPAD, the dead time is controlled by the applied voltage. For passive quenched SPAD, the dead time is determined by the quenching resistance and the capacitance of the SPAD. So far, the minimum dead time can be achieved is within a few ns [23].

Background counts determine the fundamental noise level for the SPAD-based

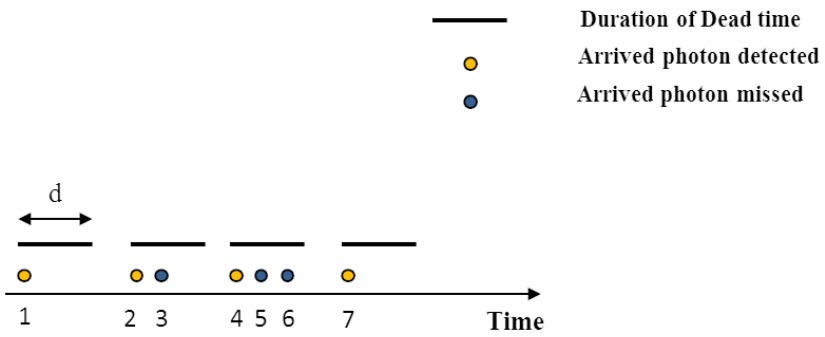


Figure 2.8: illustrates the effect of dead time. Photons 1, 2, 4, 7 are detected. Photons 3, 5, 6 are missed as they arrived in the dead time duration.

receiver. To achieve high sensitivity, the background counts are required to be minimised. The background counts are generated by the ambient light and the dark counts. The typical mechanism for reducing the impact of ambient light has been discussed in section 2.1. Dark counts are the avalanche events generated in the absence of incident light [34]. Dark counts are characterised by the dark count rate (DCR), which refers to the number of dark counts generated within a second. The DCR can be reduced by controlling the operation temperature, reducing the bias voltage of the SPAD, limiting the SPAD array size and optimising the device fabrication process [34].

2.6 State-of-the-art SPADs for VLC

Using a SPAD-based receiver for VLC is an emerging field in optical communication. The theoretical and experimental investigation of using SPADs for VLC starts in recent years. At the early stage, researchers interested in establishing the appropriate theoretical models for describing the signal distribution of the SPADs [36–38]. [36,37] state that the signal distribution of the SPADs follows the Poisson distribution with the mean value equal to the number of detected photons in the observation time. Apart from using Poisson distribution, [38] points out that the Gaussian distribution

is also a good approximation to the signal distribution of the SPADs. However, the statistical model which is more accurate to estimate the actual SPADs' output signal distribution is unclear. At present, most of the theoretical investigation in this field is based on the Poisson distribution [39–43].

Based on the proposed Poisson models and relevant channel models, the performance of using the SPAD-based receiver in different application scenarios was estimated. At present, applying the SPAD-based receiver in the low ambient light condition has drawn significant attention. [39] theoretically estimated the sensitivity of a SPAD-based receiver in a dark indoor environment. Results in this article predict that a SPAD-based receiver can be 30.5 dB better than a commercial PD based receiver at a data rate of 1 Mbps in the dark indoor environment when using OFDM. [40] estimated the performance of using the SPAD-based receiver in a down-hole environment. Simulation result predicts that only 8 dBm optical power is required by a SPAD-based receiver when the signal is sent through a 4000 meters long gas well pipe. Since the LED transmitter in the down-hole communication system is battery powered, this result suggests that the down-hole communication system using SPAD-based receiver can achieve a sufficiently long operation time.

Recently, researchers start to investigate using the SPAD-based receiver in the underwater VLC system. The advantage of using the SPAD-based receiver compared to other PDs in the underwater environment were discussed in [41, 42]. [41] compares the link performance between using SPAD (SPCM-AQRH-15-FC) and using APD (Hamamatsu S8664-30K) in a clean ocean channel. Results in [41] suggest that the SPAD-based receiver is more sensitive than the APD-based receiver. [42] compares the performance of a SPAD-based receiver (SensL B-series MicroSB 30020) with a photomultiplier tube (PMT) (Hamamatsu R12896) based receiver in the clear ocean water channel and coastal water channel using an exponential attenuation channel model. Due to the small active area of the SPAD array (SensL B-series MicroSB 30020),

the simulation results in [42] show that the SPAD array (SensL B-series MicroSB 30020) based receiver is worse than the PMT (Hamamatsu R12896). This result firstly points out that, although the SPAD array has an undebatable advantage, the small active area of the SPAD array can limit the SPAD array's sensitivity. Apart from the small active area, the background counts generated by the transmitter its self can also limit the SPAD-based receiver's performance. Results in [43] suggest that a better link performance is given when the extinction ratio is small. [41] estimates the performance of using the SPAD-based receiver for long distance transmission in the underwater environment. The simulation results in [41] show that the SPAD (SPCM-AQRH-15-FC) has the potential to support a 500 m transmission in the pure seawater.

Data rate	Year	Coding scheme	SPADs used	Paper
100Mbps	2013	OOK	Homemade	[25]
200Mbps	2015	OOK+DFE	Homemade	[44]
200Kbps	2015	4-PAM	Homemade	[45]
60Mbps	2016	4-PAM+CSK	Homemade	[46]
20Mbps	2017	OOK	SPCM-AQRH-15-FC	[47]

Table 2.2: Recent demonstration based on the SPAD-based receiver.

Besides the theoretical study, experimental demonstrations of using SPADs for VLC have already been reported in [25, 44–47]. Table 2.2 summarises the recent experimental demonstrations. All these experiments were performed in the indoor environment within a directed LOS link. So far, the maximum data rate that has been achieved using a SPAD-based receiver is 200 Mbps.

Chapter 3

A comparison of APD and small SPAD-based receivers

3.1 Introduction

SPADs are anticipated to be more sensitive than APDs. However, the sensitivities of the current SPADs are limited by dead time, small active area, low fill-factor, background counts, and the low PDE. In this chapter, the sensitivity of an existing small SPAD array and a typical APD are compared. This chapter begins with a characterisation of the transmitter that is used in all the experiments in this project, followed by a brief description of the small SPAD array which is tested in this chapter. A general model is then introduced to fit the measured output response of the active quenched small SPAD array. Afterwards, two analytical models (Poisson model and Gaussian model) which are widely used to estimate the SPAD-based receiver's BER performance are compared and validated through an OOK link test. The measured sensitivities of the small SPAD array at a data rate of 100 Mbps both in the dark and in the ambient light condition are reported. At the end of this chapter, the measured sensitivities of that small SPAD array are compared to a typical APD.

3.2 Transmitter characterisation

A commercially available Resonant-Cavity LED (RCLED), RC650-TO46FW, was selected as the transmitting source in this research in order to achieve sufficient modulation bandwidth. The modulation bandwidth of the RCLED depends on the bias voltage [48]. Figure 3.1 shows the measured modulation bandwidth of the selected RCLED at different bias voltages. This result indicates that the modulation bandwidth of this selected RCLED varies from 40MHz to 137MHz. Figure 3.2 shows the measured operating range of the selected RCLED. The measured result suggests that the applying voltage of the RCLED at bit 0 is required to be set below 0.8V so that the RCLED is totally switched off at the bit 0 and hence no background noise is generated by the transmitter itself. To prevent signal clipping, the maximum voltage that can be applied to create the highest signal level is 1.8V since the RCLED will be saturated when the applying voltage is higher than 1.8V. As a result, the maximum bias voltage for the RCLED to generate OOK signal is 1.3V which achieves a modulation bandwidth of 100 MHz.

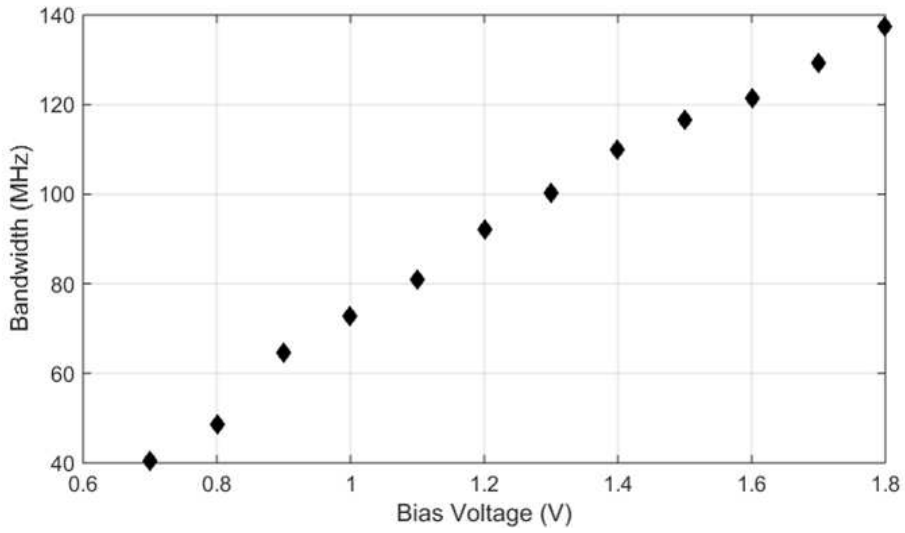


Figure 3.1: Modulation bandwidth of the tested RCLED (RC650-TO46FW) at different bias voltages.

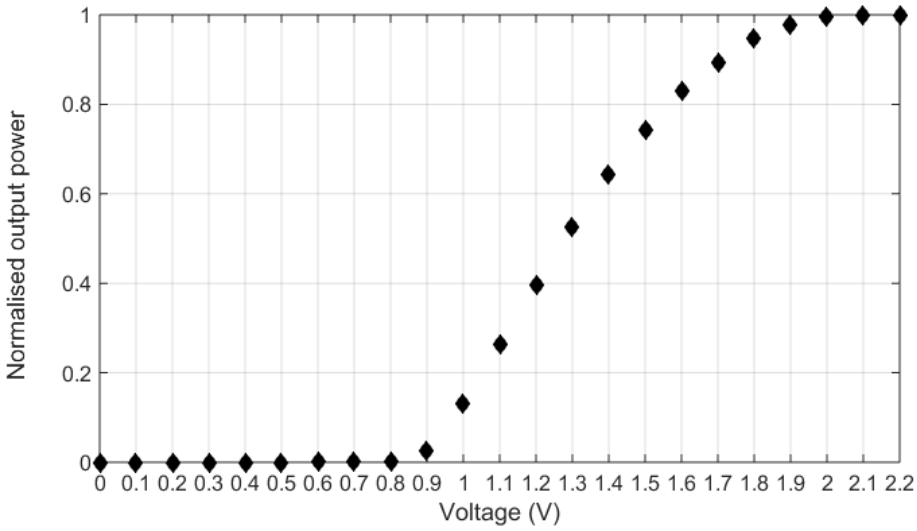


Figure 3.2: Measured operating range of the tested RCLED (RC650-TO46FW).

The response of LED is generally modelled by a first order low pass filter [15], which is expressed as

$$H_{LED}(s)|_{s=j\omega} = \frac{\omega_c}{\omega_c + s} = \frac{1}{1 + j(\frac{\omega}{\omega_c})} \tag{3.1}$$

where ω_c is the cut off frequency in rad/s. The time domain response of the LED is given by equation (3.2) which is the inverse Laplace transform of equation (3.1)

$$h_{LED}(t) = \frac{1}{T_c} e^{-\frac{t}{T_c}} \tag{3.2}$$

where T_C is

$$T_c = \frac{1}{\omega_c} = \frac{1}{2\pi\Delta f} \tag{3.3}$$

Term Δf refers to the modulation bandwidth of the LED. The accuracy of using equation (3.2) to model the tested RCLED has been investigated, and the fitting result is shown in figure 3.3. The dashed line in the figure represents the measured frequency response of the RCLED, and the solid line is generated by (3.2). It shows that equation (3.2) fits the measured RCLED frequency response reasonable well.

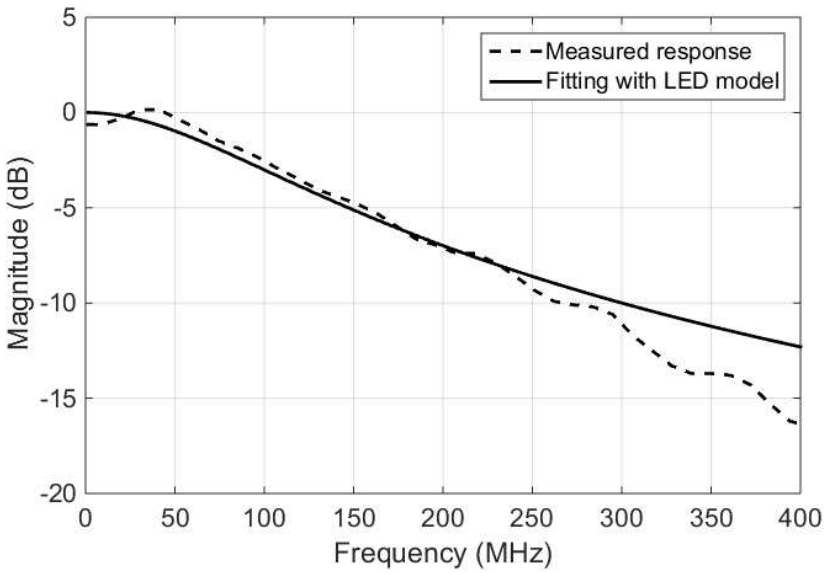


Figure 3.3: Measured frequency response of the tested RCLED (RC650-TO46FW) at the bias voltage of 1.3V fitted with the general LED model.

Using equation (3.2), the impact of ISI introduced by the tested RCLED only at different data rates has been investigated. The impact of the ISI can be quantified by the eye opening EO which is calculated by equation (3.4) [49].

$$EO = \min(A_1) - \max(A_0) \tag{3.4}$$

where A_1 is the amplitude of the signal represents bit 1 at the best sampling time and A_0 is the amplitude of signal represents bit 0 at the best sampling time. The signal $y(t)$ generated by RCLED is expressed as

$$y(t) = h_{LED}(t) * x(t) \tag{3.5}$$

where $*$ is the convolution operator, $x(t)$ is the transmitted OOK symbol (-1 and +1), and $h_{LED}(t)$ is the channel response of the RCLED expressed by equation (3.2). Based on equation (3.4) and (3.5), the calculated OOK eye openings at different data rates when the RCLED bandwidth is 100 MHz are shown in figure 3.4. This result

suggests that no ISI is generated by the RCLED when the data rate is below 100 Mbps at the RCLED bandwidth of 100 MHz.

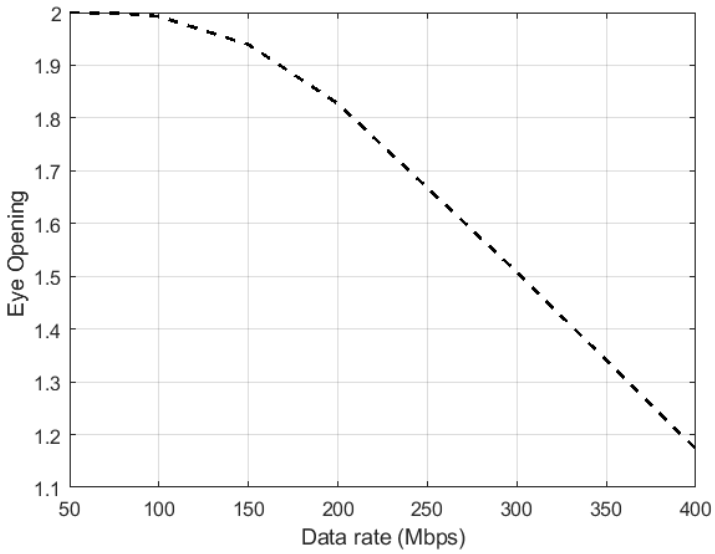


Figure 3.4: Eye opening at different data rates when the RCLED bandwidth is 100 MHz.

3.3 The tested SPAD array

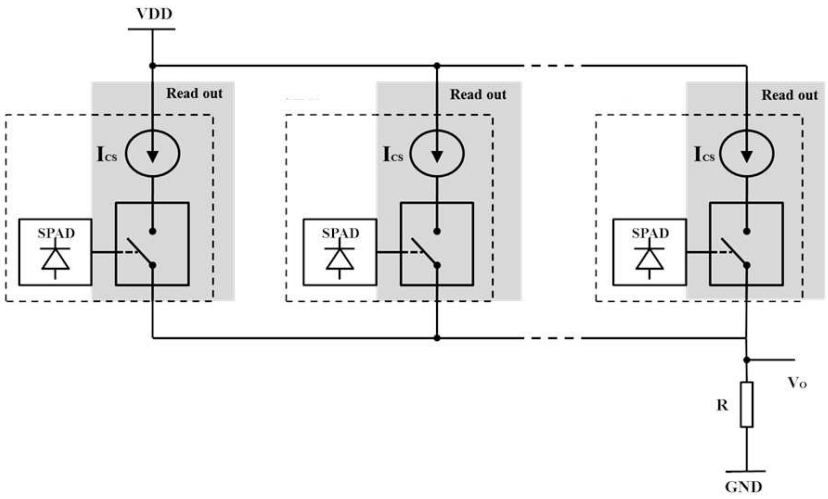


Figure 3.5: Simplified schematic for the tested SPAD array.

An array of 60 SPADs is used in the experiments described in this chapter. Ta-

ble 3.1 [23] lists the key parameters of this SPAD array. The simplified schematic of this SPAD array is shown in figure 3.5. The total output current of this SPAD array is an aggregation of the output currents associated with different SPAD cells [23]. Each SPAD cell contains an individual SPAD, a current source and a switch circuit. The switch is enabled by the SPADs output signal [23]. When an avalanche event is detected, the switch conducts during the SPADs dead time which enables the current I_{CS} to be added to the common output node [23]. The overall output current is then converted to a voltage by passing through an off-chip 50 Ω load resistor. At a particular sampling point, the total output voltage equals to the number of detected events multiplying with the voltage value which corresponds to one SPAD fire. This SPAD array uses the active quenching scheme and its dead time can be varied using an input voltage supplied by the user.

Process	180nm
Number of SPADs	60
Breakdown Voltage	10.4V
Diameter of Active Area	10μm
Fill Factor	3.20%
Minimum dead time	5ns
Average Dark Count Rate	90kHz
PhotonDetection Probability 650nm with an excess voltage of 1.6V	6.90%

Table 3.1: Summary of key parameters of the tested SPAD array.

3.4 Nonlinear model of the active quenched SPAD

For the active quenched SPAD, the incident photon within the dead time is simply missed [50]. The relationship between the dead time of a single SPAD and the av-

erage time between detected photons affects the performance of SPAD arrays. For a single SPAD, the number of detected photons within $1s$ observation time, N, can be expressed as

$$N = \frac{\eta A_{SPAD} \left(L_{dark} + L\right)}{E_p} \tag{3.6}$$

where E_p is the single photon energy, η is the photon detection probability (PDP) of the SPAD, A_{SPAD} is the active area of the SPAD, L is the incident light intensity in $\mathrm{W/m^2}$, and L_{dark} is the equivalent intensity that represents the effect of unavoidable dark counts. Therefore, the average time between detected photons can be expressed as

$$t_{interdetected} = \frac{1}{N} = \frac{E_p}{\eta A_{SPAD} \left(L_{dark} + L\right)} \tag{3.7}$$

When the incident light intensity L is low enough, $t_{interdetected}$ will be much longer than the dead time. As a result, the average number of detected events, $counts$, by the SPAD within an observation time T will be

$$counts = (L + L_{dark}) \times T \times \frac{\eta A_{SPAD}}{E_p} \tag{3.8}$$

For an array of N_{SPADs} SPADs, the average number of detected events, $counts_{array}$, in observation time T will then be

$$counts_{array} = N_{SPADs} \times (L + L_{dark}) \times T \times \frac{\eta A_{SPAD}}{E_p} \tag{3.9}$$

For convenience, equation (3.9) can be written as

$$counts_{array} = N_{SPADs} \times (L + L_{dark}) \times T \times \alpha \tag{3.10}$$

where α is defined

$$\alpha = \frac{\eta A_{SPAD}}{E_p} \tag{3.11}$$

Equation (3.10) shows that the number of detected events is proportional to the incident light intensity. This equation is expected to be valid if the incident light level is low enough so that the time between detected photon per SPAD is orders of magnitude longer than the dead time of the SPADs. If this condition is not satisfied, the incident photons will hit the inactive SPADs and the number of detected events will be reduced because of the dead time [51]. When the incident light level is high enough, the SPAD array will be saturated. In this case, a photon is capable to be detected when the dead time from the previous detected photon ends. Therefore, for an array of N_{SPADs} SPADs with a dead time of τ, the maximum number of detected events $counts_{max}$ within observation time T will be

$$counts_{\max} = N_{SPADs} \times \frac{T}{\tau} \tag{3.12}$$

An expression for representing the average number of detected events, *counts*, that combines the expected linear response at low light intensities with saturation at high light intensities is

$$counts = \frac{N_{SPADs} \times \alpha \ \times \ T \ \times (L + L_{dark})}{1 + \alpha \ \times \ \tau \ \times (L + L_{dark})} \tag{3.13}$$

The accuracy of equation (3.13) has been verified by the tested small SPAD array. Within a predetermined time, the average number of counts at different incident light intensities and dead times were obtained by both changing the incident light incident emitted by the RCLED and the dead time of tested SPAD array. The discrete spots in figure 3.6 are the measured average number of counts at different light intensities and dead times. The solid curve in figure 3.6 shows estimated result based on equation (3.13). It can be seen that all the measured data falls on the estimated

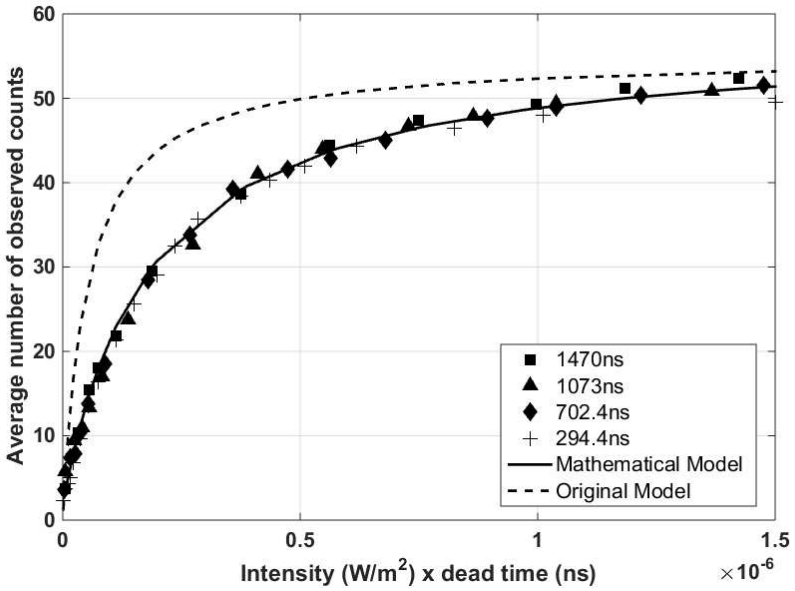


Figure 3.6: The measured average number of counts as a function of the product of the intensity of the light falling on the SPAD array and the SPAD dead time for four different dead times. This data is compared to the solid line which represents the results expected using equation (3.13) and a dashed line which represents the results obtained using a previously proposed method of determining the impact of dead time of the performance of an array of SPADs, equation (8) in [22]

curve when the x-axis is a product of dead time τ and incident light intensity L. This happens because the SPAD output response relies on the ratio of the SPAD dead time to the inter-photon time. At a fixed dead time, reducing the inter-photon time will increase the probability of photons impinging the inactive SPADs and hence increase the probability of photons to be missed. Correspondingly, at a fixed inter-photon time, reducing the dead time will increase the probability of photons impinging the active SPADs and hence reducing the probability of a photon to be missed. Equation (3.7) suggests that the average inter-photon time is proportional to the reciprocal of the light intensity L. The ratio of dead time to inter-photon time is therefore proportional to the dead time τ multiply by the light intensity L.

Moreover, the dashed curve in figure 3.6 is calculated by the dead time model proposed in [22] which is expressed as

$$counts_{array} = counts \times \frac{N_{SPADs}}{N_{SPADs} - counts} \tag{3.14}$$

Comparing the two curves, it is clearly that equation (3.13) is more accurate than equation (3.14) to estimate the output response of the SPAD array at different operation conditions.

3.5 SPAD OOK measurement result

This SPAD array was then used as the receiver in a VLC link. The experimental set-up for test the link performance is shown in the figure 3.7. In this experiment, an Agilent 81150A arbitrary waveform generator (AWG) was used to drive the RCLED to transmit an OOK modulated pseudorandom binary sequence (PRBS) sequence. The experiment was performed in an environment without room lighting. To further attenuate the ambient light generated by the laboratory equipments, a 650 nm band-pass optical filter with a 40nm bandwidth was placed over the SPAD array. Then a high resolution oscilloscope HDO6014-MS captures the output signal from the SPAD array. After synchronisation, the captured signal was decoded to the binary bits according to the searched decision threshold. The BER was then calculated by comparing the decoded bits with the transmitted bits.

3.5.1 Eye diagram

Figure 3.8 shows the raw eye diagram captured by the oscilloscope at a BER of 7.9×10^{-4} when the data rate is 100 Mbps. This BER is better than 10^{-3} which is the BER limit that Forward Error Correction (FEC) required [20]. For convenience, this BER (7.9×10^{-4}) was chosen as the reference BER in this chapter. In this experiment, the incident light intensity over the SPAD array is 1.1 W/m^2, which corresponds to an optical power of -53 dBm over the active area of the tested SPAD

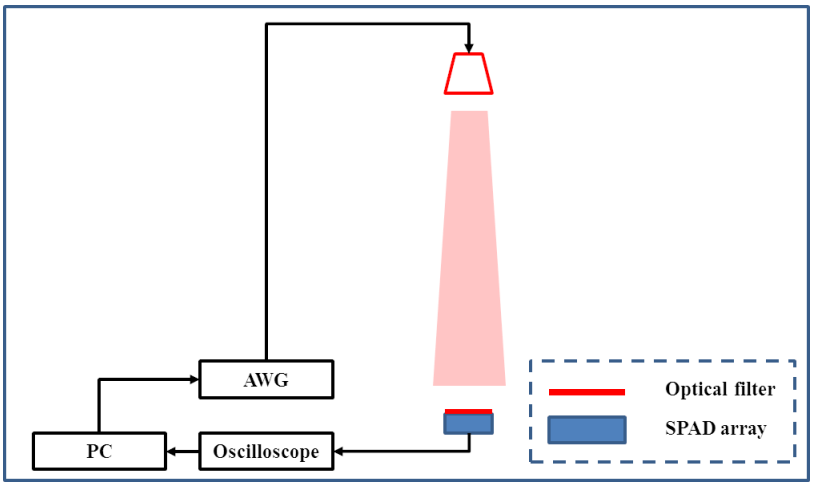


Figure 3.7: Experimental set-up for the OOK link test.

array. It can be seen that this incident light level created a reasonably clear eye-opening. More importantly, the noise at symbol level 1 is significantly higher than the noise at symbol level 0. This suggests that, for this SPAD-based receiver, the photon shot noise is a significant, if not the dominant, source of noise. Another notable feature of this eye diagram is its symmetry. This symmetry arises because the temporal response of the output is determined by the pair of transistors used to control the output current. These two transistors set a threshold voltage and they have identical responses when the SPAD bias voltage increases or decreases through this threshold. It is therefore these transistors that generate the symmetry in the eye diagram.

3.5.2 Effect of dead time

For this particular SPAD array, the output current associated with each SPAD cell are steered to the common output during the SPADs dead time. This means that the pulse time of this SPAD array equals the dead time. At a given incident light intensity, the amplitude of the output signal at the sampling point is determined by the number of fired SPADs aggregated together. If the dead time, and hence the output pulse

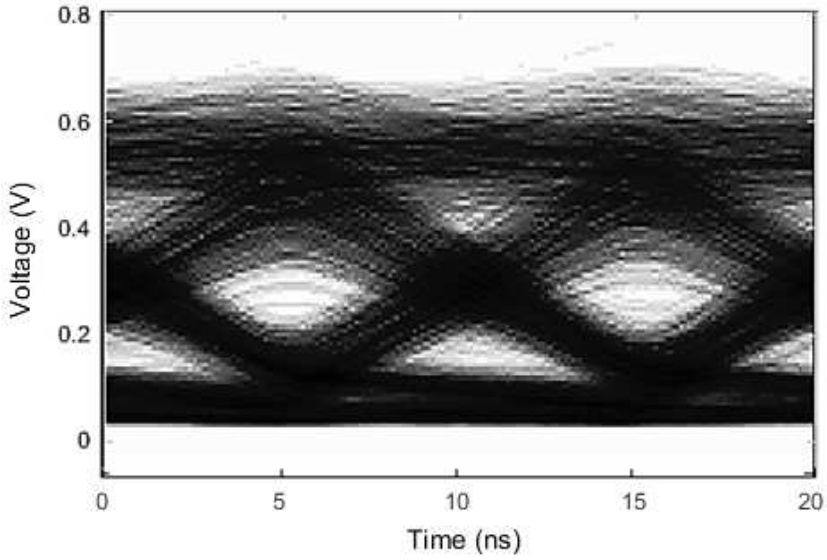


Figure 3.8: A raw eye diagram at a data rate of 100Mbps when the BER is 7.9×10^{-4}.

time, is much shorter than the bit time, the output current generated by the detected photons within each bit period will not necessarily be aggregated together at the best sampling point. However, if the dead time, and hence output pulse time, is too long compared to the bit time, this will cause ISI. Therefore, the optimum dead time and hence the pulse time for data communication will be approximately equal to the bit time. Figure 3.9 illustrates the measured BER using this tested SPAD array at three data rates against different dead times. As expected, the minimum BER is achieved when the dead time of this type of SPAD array is slightly shorter than the bit time.

3.5.3 Effect of ISI

The histogram of detected photons within each bit period is shown in figure 3.10. There are three peaks in this figure. The lower peak is the true distribution of bit 0. It is generated when a bit 0 is transmitted after one or more bit 0. The width of this peak is determined by the 72 mV_{pp} electronic noise within the system. The second peak, with a mean of approximately 3, is caused by the ISI. It is generated when a bit 0 is transmitted follows a bit 1. The final peak, with a mean of approximately 18,

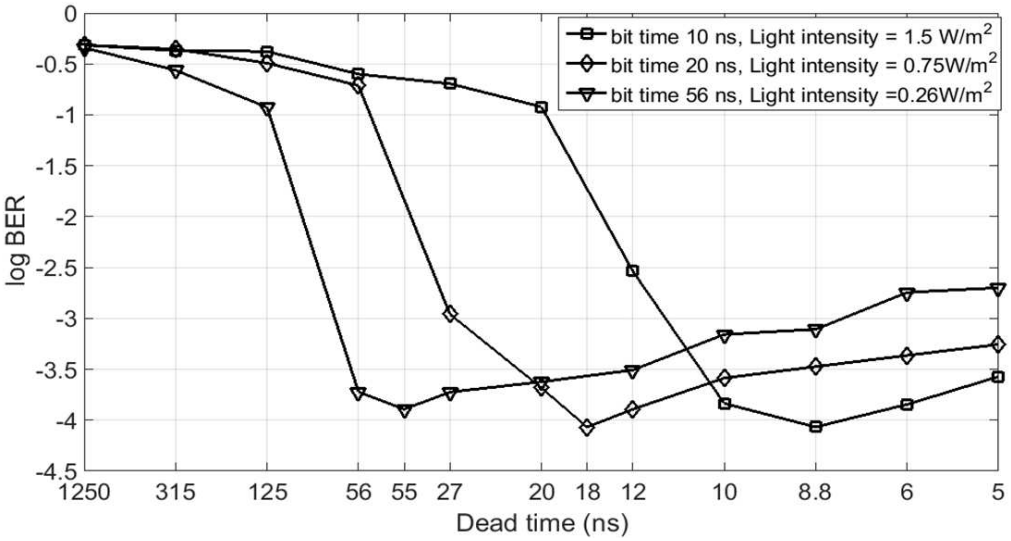


Figure 3.9: The measured BER at different dead times for a data rate of 100 Mbps, 50 Mbps and 17.9 Mbps. In each case the lowest BER is achieved for a dead time which is slightly shorter than the bit time.

corresponds to bit 1 is being transmitted. Since the shot noise is signal dependent noise, the variance of this peak is much broader. These results demonstrate that approximately 15 detected photons per bit are required by this SPAD array to achieve a BER of 7.9×10^{-4}. This sensitivity can be further improved by using Decision feedback equalisation (DFE) to reduce the impact of ISI [21]. After applying DFE, the sensitivity of this receiver has been improved by 3 dB. For an ideal photodetector, using equation (2.8), it can be calculated that an average of 6.5 detected photons per bit is required to achieve the BER of 7.9×10^{-4} in the dark. In fact, this SPAD array only requires an average of 10.2 detected photons per bit to achieve this BER. When detected photons per bit are considered, the performance of the SPAD array is close to that of an ideal receiver that is limited by Poisson noise.

3.5.4 Effect of ambient light

When the VLC system is deployed within the indoor environment, due to the presence of the room lighting, the impact of the ambient light cannot be avoided. In that case,

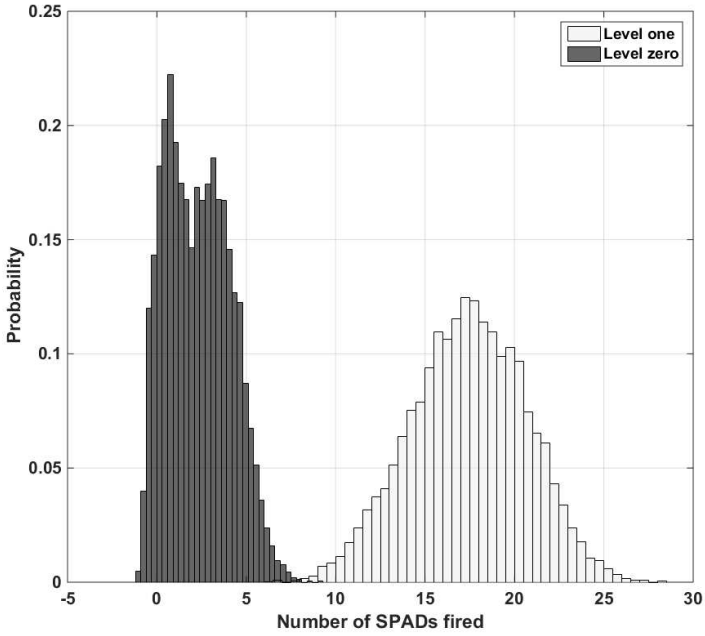


Figure 3.10: The measured histograms of the number of SPADs that have fired within a dead time of the end of each bit period when the bit time is 10 ns, the dead time is 8.8 ns and the measured BER is 7.9×10^{-4}.

the Poisson noise is expected to become the dominant noise source not only at bit 1 but also at bit 0. The BER of a system limited by Poisson noise can be calculated by equation (2.8). When the mean value in Poisson distribution is large enough, Poisson distribution can be approximated by Gaussian distribution [52]. Therefore, [25] presents another method to estimate the BER of a SPAD-based receiver according to the Gaussian distribution, which is given by

$$BER = \frac{1}{2} \times \left[\frac{1}{2} erfc\left(\frac{(N_1 - N_{th})}{\sigma_1 \sqrt{2}} \right) + \frac{1}{2} erfc\left(\frac{(N_{th} - N_0)}{\sigma_0 \sqrt{2}} \right) \right] \tag{3.15}$$

where N_1 is the average number of detected photons encoded in bit 1, N_0 is the average number of noise counts encoded in bit 0, N_{th} refers to the decision threshold, σ_1^2 is the noise when bit 1 is transmitted, and σ_0^2 refers to the noise when bit 0 is transmitted. The optimum decision threshold is given by [25]

$$N_{th} = \frac{\sigma_0 N_1 + \sigma_1 N_0}{\sigma_0 + \sigma_1} \tag{3.16}$$

Based on equation (3.16), equation (3.15) is expressed as

$$BER = \frac{1}{2} erfc\left(\frac{Q}{\sqrt{2}}\right) \tag{3.17}$$

where Q parameter is calculated as

$$Q = \frac{N_1 - N_{th}}{\sigma_1} = \frac{N_{th} - N_0}{\sigma_0} = \frac{N_1 - N_0}{\sigma_0 + \sigma_1} \tag{3.18}$$

For SPADs, the Poisson noise is expected to become the dominant noise source at bit 1 and bit 0. Therefore, $\sigma_1 = \sqrt{N_1}$, $\sigma_0 = \sqrt{N_0}$ and hence Q parameter is expressed as

$$Q = \frac{N_1 - N_0}{\sqrt{N_1} + \sqrt{N_0}} \tag{3.19}$$

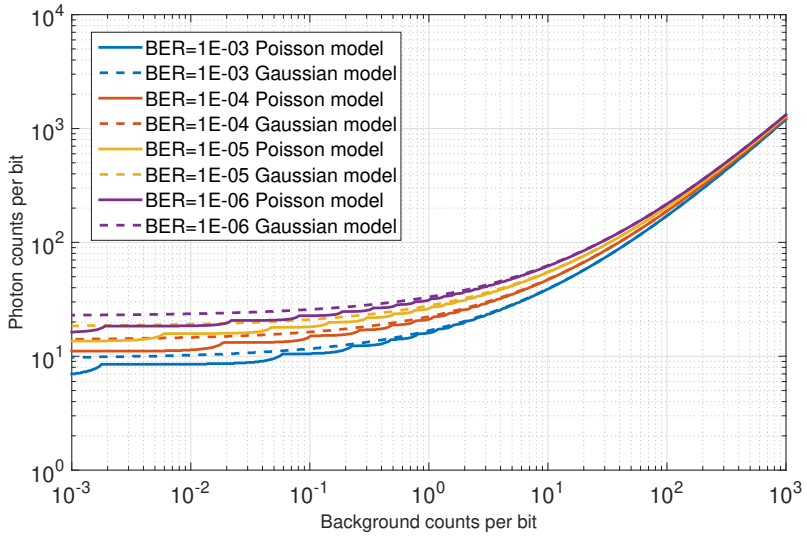


Figure 3.11: Photon counts per bit required to maintain different target BERs at different background counts, the dashed line is calculated based on Gaussian model equation (3.15) and the solid line is calculated based on Poisson model equation (2.8).

Figure 3.11 shows the photons per bit required to achieve different BERs calcu-

lated based on the Poisson model and the Gaussian model. It can be seen that the Gaussian model is getting indistinguishable from the Poisson model with the background photon counts per bit getting increased. In order to quantify the difference between the Gaussian model and the Poisson model, based on the data in figure 3.11, the error fraction is calculated using the equation below.

$$Error\ fraction = \frac{|Data_{Gaussian} - Data_{Poisson}|}{Data_{Poisson}} \tag{3.20}$$

where $Data_{Gaussian}$ refers to the data calculated using the Gaussian model in figure 3.11 and $Data_{Poisson}$ refers to the data calculated using the Poisson model in figure 3.11. The calculation results are shown in figure 3.12. It can be seen that, at the target BER of 10^{-3}, the difference between using the Gaussian model and the Poisson model is less than 2% when the background counts per symbol are higher than 2 counts per bit. Therefore, when the background counts per bit are higher than 2 counts per bit, the Gaussian model is an accurate approximation to the Poisson model and the Q parameter (equation (3.17) and (3.18)) can be used to evaluate the SPAD-based receiver's BER performance.

To evaluate the practically achievable performance of the SPAD-based receiver within the ambient light, the OOK link in figure 3.7 was placed within a practical indoor lighting environment. The ambient light intensity within this indoor environment was changed by dimming the rooms fluorescent lighting, in a range of 120 lux to 980 lux. To reduce the impact of ambient light and hence achieve the best practically achievable performance, an aperture was placed over the SPADs to restrict the FOV of the receiver to approximately 24 degrees which still maintains practical mobility of this VLC system.

The spots in figure 3.13 illustrate the signal penalty required by this particular SPAD array to maintain the BER of 7.9×10^{-4} at different background light intensities after equalisation (EQ). The solid curve in figure 3.13 is the estimated signal penalty to

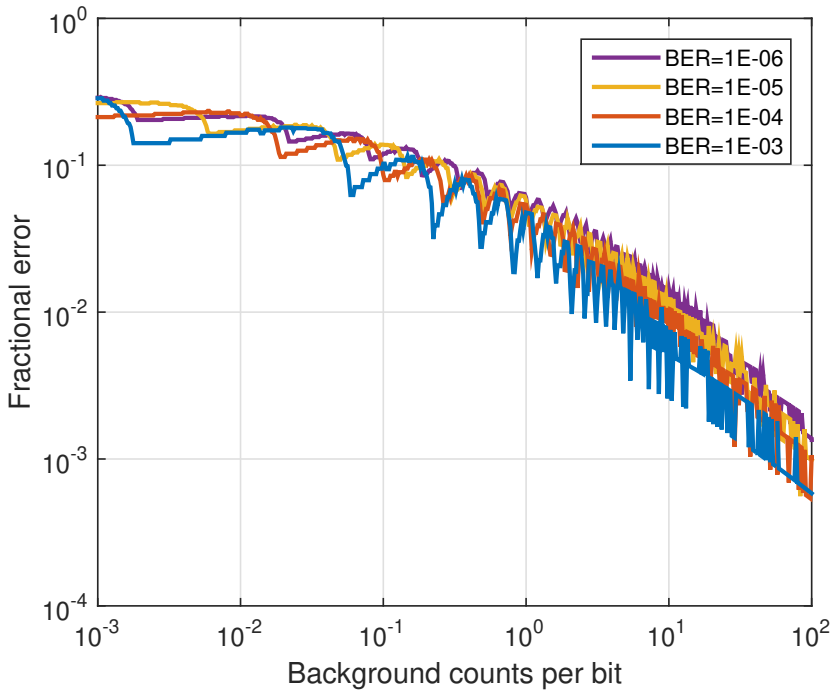


Figure 3.12: Fractional error of the Gaussian model.

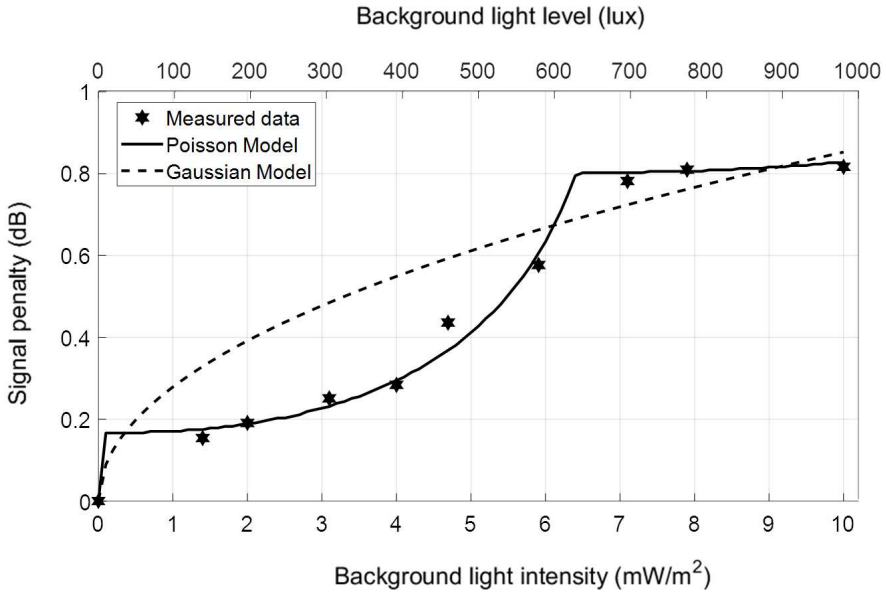


Figure 3.13: The signal penalty required for the SPAD to achieve a BER of 7.9×10^{-4} at different background light levels, shown in both $\mathrm{mW/m^2}$ (bottom x-axis) and lux (top x-axis), for 100 Mbps when equalization has been used to reduce ISI.

maintain the target BER calculated by equation (2.8). Due to the decision threshold in equation (2.8) being integer, there is an abrupt change within the estimated curve

when the background intensity is around 6.5 mW/m^2. When the background intensity increases from 1 mW/m^2 to 6.5 mW/m^2, the probability of a bit 0 being decoded as a bit 1 is increased. To achieve the target BER, the additional signal intensity is required to reduce the probability of a bit 1 being decoded as a bit 0. However, when all the errors come from a bit 0 being decoded as a bit 1, the decision threshold is required to be increased. Once this happens, almost all the errors come from a bit 1 being decoded as a bit 0. When the background light intensity is further increased, the signal intensity is required to be improved again to keep the BER. Eventually, the decision threshold is required to be increased again. As a result, the abrupt change at 6.5 mW/m^2 will happen again at higher background light intensities. The dashed curve is based on equation (3.15).

Compared to the Poisson model (equation (2.8)), the Gaussian model (equation (3.15)) is not accurate since the detected background counts per bit at this small SPAD array in the experiment are below 0.1 counts per bit. The excellent agreement between the measured data and the estimated results using equation (2.8) confirms that, in ambient light, the dominant noise source in the SPAD array is Poisson noise. Furthermore, these results show that, with a restricted FOV, a SPAD-based receiver only requires modest increases in transmitted power when it is operated in the practical ambient light conditions.

3.6 APD OOK measurement result

To allow a comparison between the typical APD and the tested small SPAD array, the sensitivity of a receiver containing a 3 mm^2 commercial APD (AD1900-9-TO5i) and TIA (MAX3665) has been measured at a data rate of 100 Mbps using the same experimental set-up shown in figure 3.7. The measurement results in figure 3.14 suggest that, at the optimum bias voltage 150 V, this commercial APD-based receiver

requires a signal light intensity of 3.44 $\mathrm{mW/m^2}$ (-50 dBm optical power at the receiver, 337 photons per bit) to achieve a BER of 7.9×10^{-4} in a dark condition.

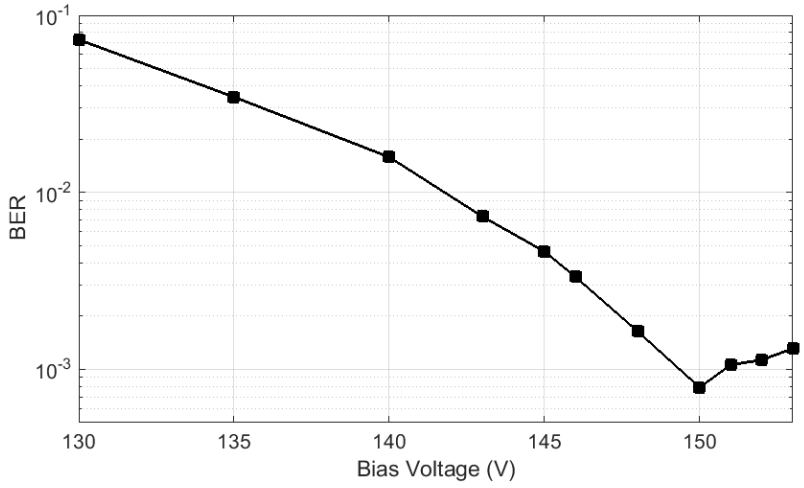


Figure 3.14: The measured BER of an APD-based VLC receiver at different bias voltages in the dark with a signal light intensity of 3.44 $\mathrm{mW/m^2}$.

When the APD-based receiver is in the presence of ambient light, in order to maintain the BER, additional signal power will be needed. The BER performance of the APD-based receiver can be calculated by equation (3.17) [15], where the parameter Q in equation (3.17) is

$$\mathrm{Q} = \frac{I_1 - I_0}{\sigma_1 + \sigma_0} \tag{3.21}$$

where I_1 is the photocurrent when bit one is being transmitted, I_0 is the photocurrent when a zero bit is being transmitted, σ_1^2 is the total noise in bit one and σ_0^2 is the total noise in bit zero. For an APD these four terms can be calculated using the equations below [15]

$$I_1 = m.R.\left(P_s + P_b\right) \tag{3.22}$$

$$I_0 = m.R.P_b \tag{3.23}$$

$$\sigma_1 = \sqrt{2e.\left(R.\left(P_b + P_s\right) + I_d\right).bw.m^{x+2} + i_{th}^2} \tag{3.24}$$

$$\sigma_0 = \sqrt{2e.\left(R.P_b + I_d\right).bw.m^{x+2} + i_{th}^2} \tag{3.25}$$

where m is the APD gain, R is the responsivity of the APD, P_s is the optical power of the signal, P_b is the optical power of the ambient light, I_d is the dark current, x is the excess noise index, bw is the noise equivalent bandwidth and i_{th}^2 is the thermal noise of the detector, which was calculated using experimental results in the dark and equation (3.26). Equations (3.24) and (3.25) both show that the noise in the system increases when background light reaches the APD. For example the total noise at bit 0 increased from $5.89 \times 10^{-16} W$ to $2.59 \times 10^{-14} W$ when the background light intensity increased from 0 to 8 mW/m^2. This significant increase in the noise level means that the signal power has to increase to maintain the same SNR. However, equation (3.24) shows that this also increasing the noise power when a bit 1 is being transmitted. The signal power level, P_s, required to obtain a particular Q value, and hence BER, in the presence of ambient light can be calculated by combining equations (3.22) to (3.25) to give

$$Q = \frac{m.R.P_s}{\sqrt{2e.\left(R.\left(P_b + P_s\right) + I_d\right).bw.m^{x+2} + i_{th}^2} + \sqrt{2e.\left(R.P_b + I_d\right).bw.m^{x+2} + i_{th}^2}} \tag{3.26}$$

Using this equation and the parameters in table 3.2 it can be calculated that when the background light intensity is 8 mW/m^2 the required value of Q is maintained if the transmitted signal intensity increases by 5 dB to 10.6 mW/m^2, because at this transmitted power the total noise when a bit 1 is transmitted increased from $1.1 \times 10^{-14} W$ to $5.9 \times 10^{-14} W$. The denominator of equation (3.26) is therefore increased from 1.30×10^{-7} to 4.04×10^{-7}, which is a 5 dB increment. Because both the numerator and the denominator increase 5 dB, the value of the Q parameter is maintained.

The effect of ambient light on the link using the APD-based receiver was measured using the same experimental procedure used to measure the impact of ambient light

Characteristics	Value
Active area	3 mm^2
Dark current	15nA @ M=100
Responsivity	35 @ M=100 ,λ= 650nm
APD gain	115 @ 150V
Excess noise index	0.36
Target BER	7.9×10^{-4}
Data rate	100Mbps

Table 3.2: Summary of key parameters of the tested APD.

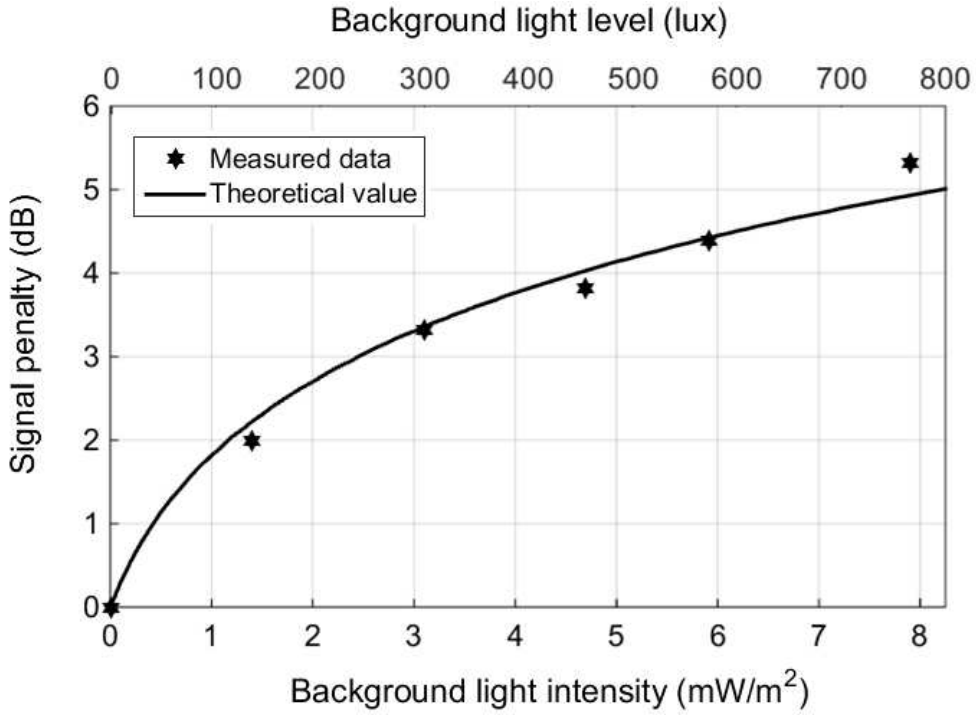


Figure 3.15: The required signal penalty for the tested APD to achieve a BER of 7.9×10^{-4} at various background light intensities. In this figure the data (stars) is compared to the predictions of equation 3.26.

on the SPAD array. The measured signal penalties required at different ambient levels are shown figure 3.15. The solid curve in this figure illustrates the theoretical signal penalty needed to maintain the target BER of 7.9×10^{-4}, which was calculated using equation (3.26) and table 3.2. The agreement between the measured data and the

results estimated by equation (3.26) demonstrates that the signal penalty required to maintain a target BER within the ambient light condition can be predicted by equation (3.26).

Comparing the signal intensities required by the tested APD and the SPAD array to achieve the same target BER, it could be found that, the tested APD-based receiver is approximately 22 dB more sensitive than the particular SPAD array used in these experiments. This is almost entirely due to the smaller area and the low fill-factor of the SPAD array, compared with that of the APD. In fact, the active area of the APD is approximately 640 times larger than the active area of the SPAD array, but the SPAD array only requires 161 times the light intensity of the APD. This shows that this early example of a SPAD array, not optimized for VLC, is approximately 4 times better than the typical APD. This result suggests that the sensitivity of the SPAD-based receiver could be more sensitive than the APD-based receiver when a larger SPAD array is used.

3.7 Summary

This chapter compares the sensitivity of a small SPAD array with a typical APD. A new expression for estimating the output response of an array of active quenched SPADs has been derived and shown to agree with results obtained with a small active quenched SPAD array. Results from this small SPAD array show that when this SPAD array is used in a VLC receiver, after EQ, the receiver only requires 1.57 times more detected photons per bit than an ideal receiver limited by Poisson noise. Consequently, this receiver requires approximately 33 times fewer detected photon per bit than a typical APD. Such an improvement is extremely valuable. However, in free-space communications, increased detection area provides equivalent gains to that in improved sensitivity. Since the tested APD is approximately 640 times larger than

the small SPAD array, the sensitivity of the small SPAD array is worse than the tested typical APD. However, the small SPAD array only requires 160 more photons than the tested APD, which suggests that larger SPAD arrays can match the performance of the typical APD. Furthermore, two widely used numerical models, the Poisson model and the Gaussian model, for estimating the BER of SPAD array are compared in this chapter. Results suggest that the Poisson model, equation (2.8), is more accurate. Gaussian model, equation (3.15) is a good approximation to the Poisson model when the background counts per bit are larger than 2 counts per bit. This result suggests that the Q parameter can be used to accurately evaluate the BER performance the SPAD-based receiver if the background counts per bit are larger than 2 counts per bit.

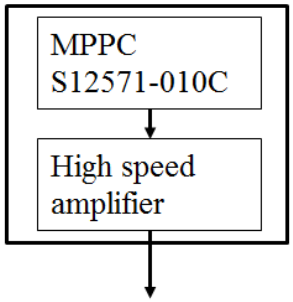
Chapter 4

Performance of larger SPAD array

4.1 Introduction

It is expected that receivers based on larger SPAD arrays could be more sensitive than the receivers based on APDs. In this chapter, the performance of receivers containing a larger SPAD array is investigated using a commercially available SPAD array module, Multi-Pixel Photon counter (MPPC) module C11209-110. This module includes a SPAD array MPPC S12571-010C and a high-speed amplifier which is shown in figure 4.1. The MPPC S12571-010C uses a passive quenching scheme and the output signals from all the SPADs within the MPPC are added together via a common output [53]. The output pulse time of S12571-010C is approximately 30 ns read from the datasheet. To have a better time resolution, this 30 ns pulse time is then reduced to around 10 ns by the high-speed amplifier which has a pass-band from 10 kHz to 40 MHz [54]. This chapter begins with a detailed description of how to process the output signal from this MPPC module. Then, the OOK link performance based on different signal processing methods are compared. Using the optimum output signal processing method, the sensitivities of this MPPC based receiver are measured both in the dark and the typical indoor ambient light condition. These measured sensitivities

are then compared with the tested APD-based receiver. At the end of this chapter, a criterion that determines a SPAD array is more sensitive than an APD in the typical indoor environment is presented.



Active Area	1mm^2
Number of SPADs	10000
Fill Factor	33%
Dark Count Rate	100 Kcps
PDE	8% @650nm
Amplifier Cut-Off Frequency	10kHz to 40 MHz

Figure 4.1: The block diagram and key parameters of MPPC module C11209-110.

4.2 Photon counting methods

The output signals from this MPPC module at different light levels are shown in figure 4.2. At very low light levels, the output signal from the MPPC module consists of discrete pulses. Since each pulse corresponds to a detected photon, the total number of detected photons can be counted by counting the discrete pulses. However, at higher light levels, the output pulses overlap which is known as the pulse pile-up effect [55]. Once this occurs, the manufacturer suggests that the output signal from the module should be treated as an analogue signal [55].

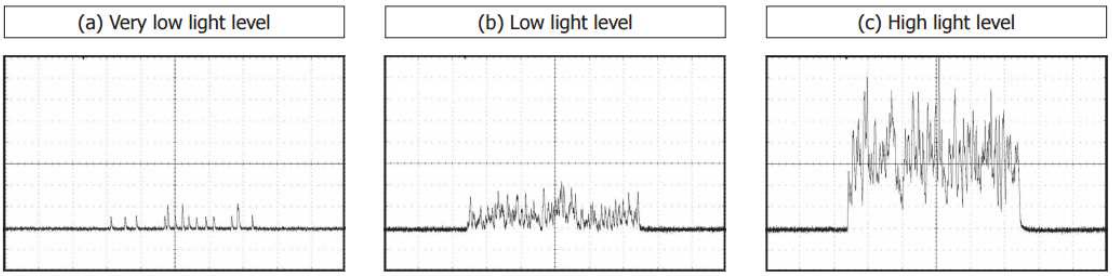


Figure 4.2: Output signal of the MPPC module from low light levels to high light levels.

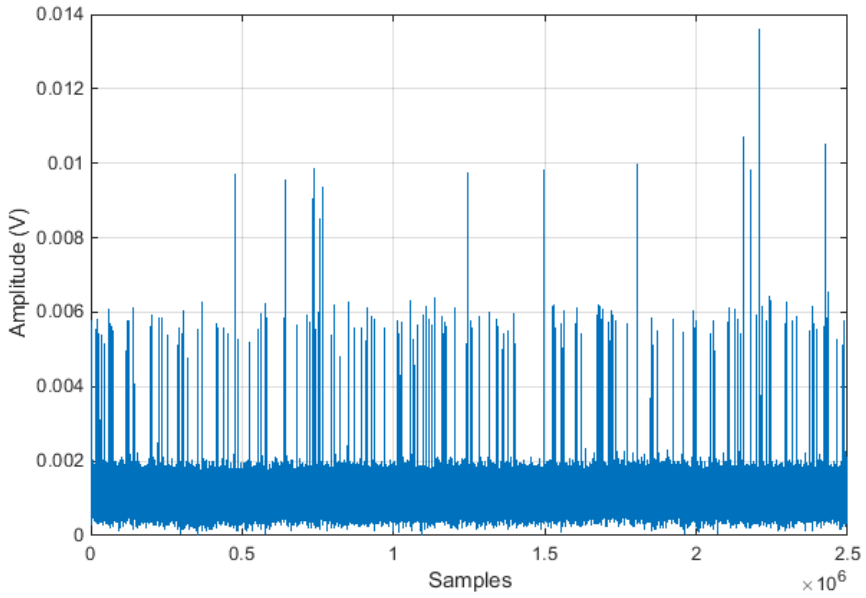


Figure 4.3: Output signal from the MPPC module measured in the dark within 1 ms. There are 200 pulses within this period counted by hand.

Photons can only be counted in photon counting mode [55]. However, there is no build-in photon counter within this MPPC module. Figure 4.3 shows the measured output signal from this MPPC module within 1 ms observation time in the dark, which has 200 pulses counted by hand. It indicates that the dark count rate of this MPPC is 200 kcps which is consistent with the data sheet. The performance of 3 photon counting methods, the peak counting method, the summation method, and the edge counting method are compared in the following sections.

4.2.1 Peak counting method

The peak counting method uses the peak information to count pulses. It first finds all the pulse peaks P from the received waveform within the observation duration. Then each peak value P_i is divided by a value P_s, which corresponds to the peak height from a single isolated photon, and then rounded to the nearest integer. The total number of counts N within the observation duration equals the sum of these

calculated integers which is expressed as

$$\mathrm{N} = \sum_{i=1}^{M} \mathrm{round}\left(\frac{P_i}{P_s}\right) \ , \ i = 1 : M, \ P_i \in P \tag{4.1}$$

where M is the total number of peaks within the measured output signal from the MPPC module.

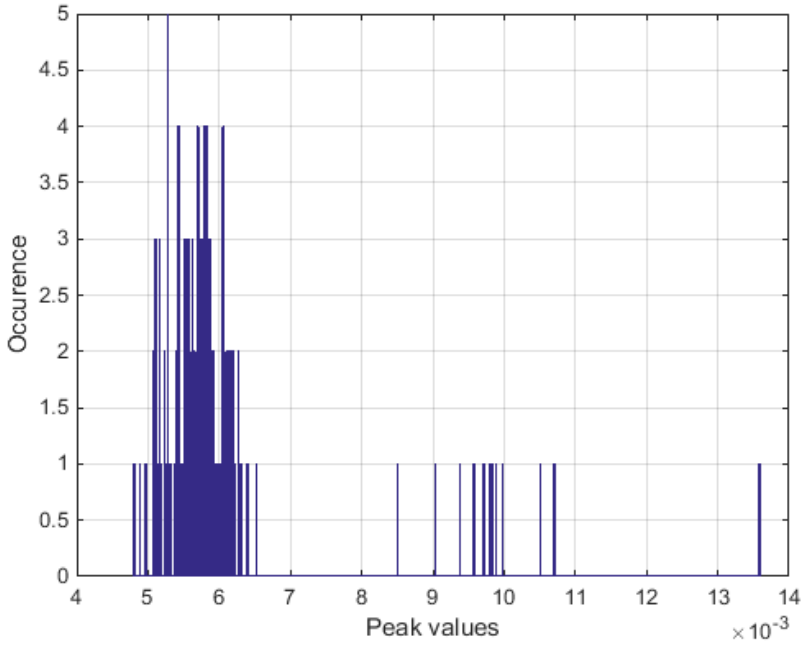


Figure 4.4: Distribution of peak values within the captured signal shown in figure 4.3.

The peak value distribution of the captured signal in figure 4.3 is shown in figure 4.4. Because the data was measured in the dark, most of the pulses correspond to one SPAD fired. Therefore, in figure 4.4, the highest distribution, the peak values vary from 0.00479 V to 0.00652 V, correspond to one SPAD fired. The second distribution, the peak values vary from 0.00851 V to 0.0107 V, correspond to two SPADs simultaneously fired. The third distribution, the peak value equals 0.0136 V corresponds to three SPADs simultaneously fired. Based upon the peak values distribution, P_s was subsequently set to 0.0048 V to convert the peak heights into a corresponding number of photons. The value 0.0048 V ensures the peak height

values at the tail of each distribution are classified correctly. When one SPAD fires, the maximum peak height of one SPAD fired pulse is 0.00652 V and the minimum peak height of one SPAD fired pulse is 0.00479 V. After these two values divided by 0.0048 V and rounded to the integer, integers 1 are given, which means all the pulses corresponding to one SPAD fired are correctly identified. When two SPADs fire, the maximum peak height is 0.0107 V and the minimum peak height is 0.00851 V. After these two values divided by 0.0048 V and rounded to the integer, integers 2 are given, which means all the pulses corresponding to two SPADs fired are correctly identified. Using the value 0.00851 V, 200 pulses are counted by the peak counting method which is consistent with the result counted by hand.

4.2.2 Summation method

Although the peak counting method is simple, there is a possibility that a peak from a photon might be obscured by the tail of a large peak caused by several photons being detected simultaneously. Compared to the peak counting method, the summation method uses information from multiple samples of a pulse rather than only one sample. The summation method first finds all the pulses related to the fired SPADs according to the peak information. For each searched pulse, within 10ns pulse time, all the samples S_j are summed together. The summed values $\sum S_j$ are then divided by a specific value S_s and rounded to the nearest integers. The total number of counts N within the observation duration equals the sum of those integers which can be expressed as

$$\mathrm{N} = \sum_{i=1}^{M} round\left(\frac{\sum_{j=1}^{j=K} S_j}{S_s}\right), \quad j = 1:K,\ i = 1:M \tag{4.2}$$

where K is the number of samples within a single isolated pulse, M is the total number of pulses within the output signal from the MPPC module, and S_s corresponds to

the value of summed samples over 10 ns pulse time which is generated by a single isolated photon.

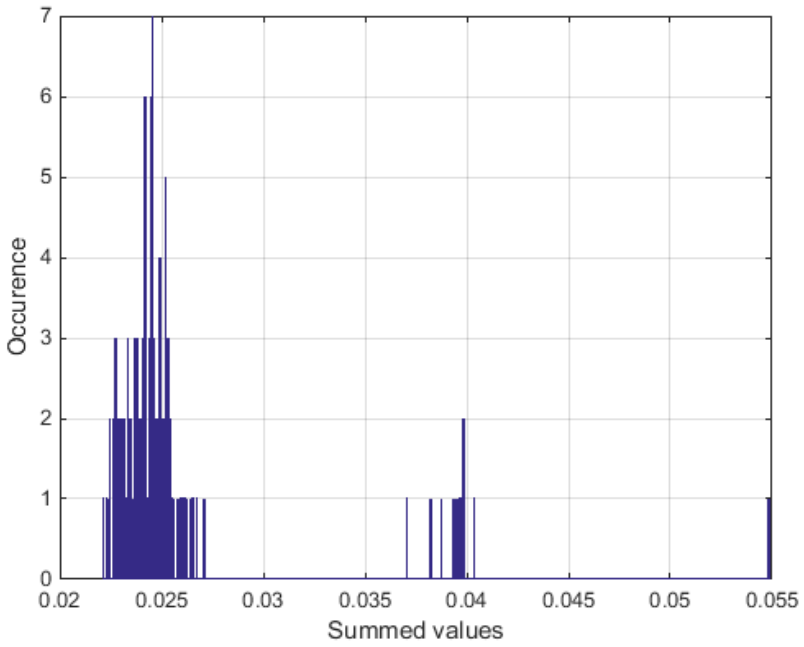


Figure 4.5: Distribution of a sum of single pulse amplitude over single pulse time (10 ns) generated from the data in figure 4.3.

The distribution of the summed pulses over the 10 ns pulse time is shown in figure 4.5. It is generated using the same captured signal shown in figure 4.3. In figure 4.5, the highest distribution, the summed values vary from 0.0221 V to 0.0271 V and correspond to one SPAD fired. The second highest distribution, the summed values vary from 0.0371 V to 0.0404 V and correspond to two SPADs simultaneously fired. The third distribution, the summed value is 0.0548 V and corresponds to three SPADs simultaneously fired. Based upon the summed values distribution, a value 0.02 V ensures that the summed values at the tail of each distribution are correctly identified. Therefore, S_s was subsequently set to 0.02 V to convert summed values into the corresponding number of photons. Using the value 0.02 V, 200 pulses are counted by the summation counting method which is consistent with the result counted by hand.

4.2.3 Edge counting method

The edge counting method counts the pulses by counting the rising edges in the output signal from the MPPC module within the observation time. The edging counting method first calculates the difference between the two adjacent samples in the output signal of MPPC within the observation duration using the equation below.

$$D\left[i\right] = S\left[i+1\right] - S\left[i\right] \quad , \; i = 1 : L \tag{4.3}$$

where $S[i]$ refers to samples in the measured output signal of MPPC module, $D[i]$ refers to the difference between the two adjacent samples and L refers to the total number of samples within 1 ms at the sampling rate of 2.5 GS/s, which is 2.5×10^6 samples. The sharp rising edges within $S[i]$ generate large peaks within $D[i]$ which are shown in figure 4.6. Therefore, the peak counting method is then applied to $D[i]$ to count rising edges by counting peaks which can be expressed as

$$\mathrm{N} = \sum_{i=1}^{M} \mathrm{round}\left(\frac{P_{D_i}}{P_{D_S}}\right) \; , \; i = 1 : M, \; P_{D_i i} \in P_D \tag{4.4}$$

where P_D refers to the peaks within $D[i]$, M is the total number of peaks within $D[i]$ and P_{D_S} corresponds a single isolated photon.

The distribution of peak heights within $D[i]$ is shown in figure 4.7. Because of the rising time of a single pulse is not a constant, at a fixed sampling rate, the sampling point at the rising edge varies, and consequently, the difference between the adjacent samples within the rising edge varies. As a result, in figure 4.7, the boundary between the distributions correspond to one SPAD fired and two SPADs fired is not as clear as figure 4.4 and 4.5 which indicates that using edge counting

method the error probability of photon detection could be higher than using the other two methods. Within the histogram, the boundary of one SPAD fired and two SPAD fired are founded by searching the original received signal $S[i]$.

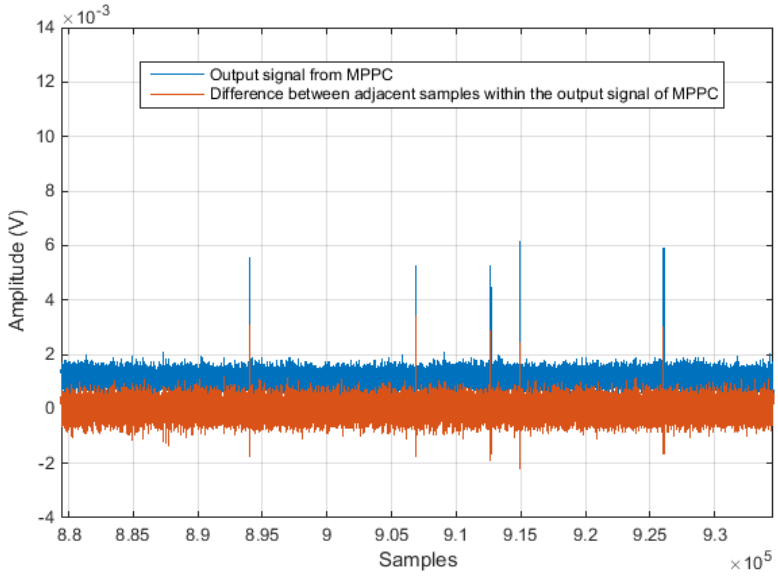


Figure 4.6: The blue curve is the output signal from the MPPC module measured in the dark and the red curve refers to the difference between the adjacent samples within the received signal.

The searched lower boundary of two SPADs fired is shown in figure 4.8(a), which is 0.00422 V. The searched upper boundary of one SPAD fired is shown in figure 4.8(b), which is 0.0041 V. P_{D_S} was subsequently set to 0.0028 V to convert P_{D_i} into a corresponding number of photons. The value 0.0028 V ensures that the values P_{D_i} at the tail of each distribution shown in figure 4.7 are classified correctly. 200 pulses are counted based on the edge counting method, which means that the edge counting method works properly in the dark using the searched value P_{D_S} 0.0028 V.

4.2.4 Evaluation of the photon counting methods

Within the photon-counting process, the pulse time and the inter-photon time are the two key times. For a fixed pulse time, reducing the inter-photon time will increase the

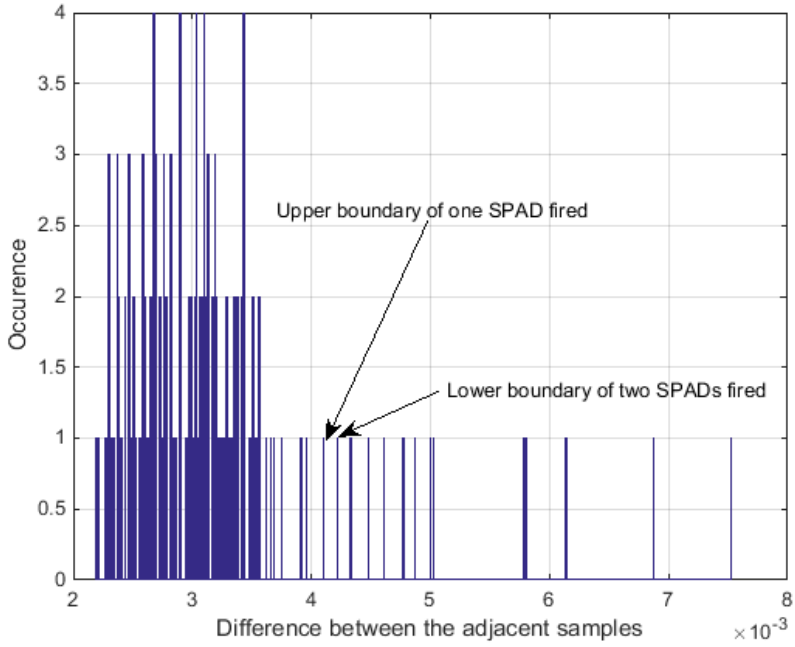


Figure 4.7: Distribution of the peak heights in $D[i]$ which is calculated using equation (4.3) based on the captured signal shown in figure 4.3.

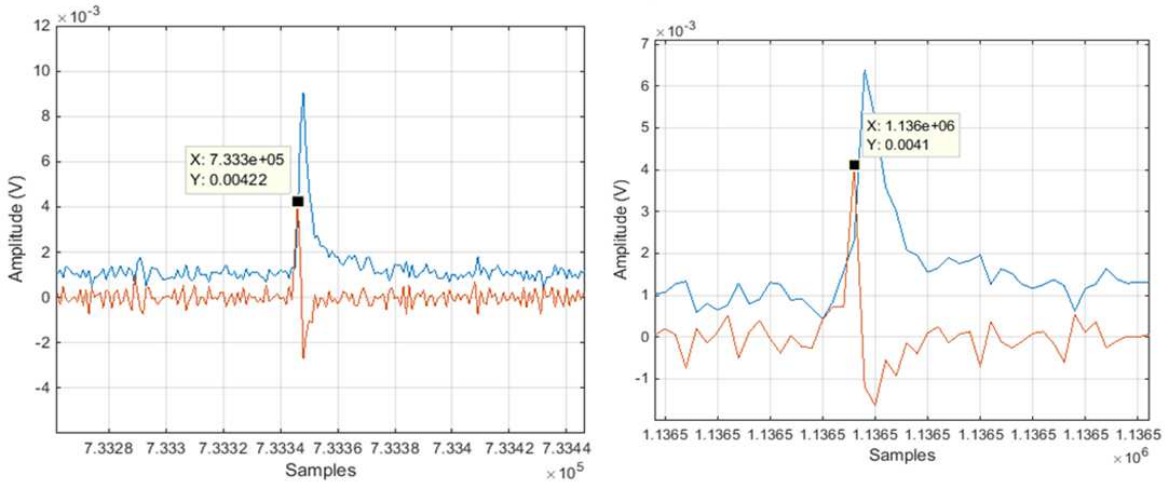


Figure 4.8: a) Lower boundary of two SPADs fired b) Upper boundary of one SPAD fired where the blue curves are the original signal $S[i]$ and the red curve are the $D[i]$.

probability of photons hitting the active SPADs and hence increase the probability of pulses overlapping. Figure 4.9 shows the measurement results of using the three photon counting methods at different light levels at 650 nm within 1 ms observation time. In the measurement, the optimum values P_s, S_s, P_{D_S}, searched in the dark

were used since these values identify the discrete pulses correctly. The expected value which corresponds to the dashed line is calculated by

$$Counts = \frac{PDE \times L \times A \times T}{E_p} \tag{4.5}$$

where T is the observation time, L is the light intensity in W/m^2, E_p is the single photon energy and A refers to the total area of the SPAD array. As expected, the photon counting performance of edge counting method is the worst. The summation method is slightly more accurate than the peak method. Moreover, figure 4.9 also suggests that photon counting modes start to lose the counting accuracy when the incident light intensity is higher than 0.4 $\mathrm{mW/m^2}$ which corresponds to the inter photon time approximately four times smaller than the pulse time.

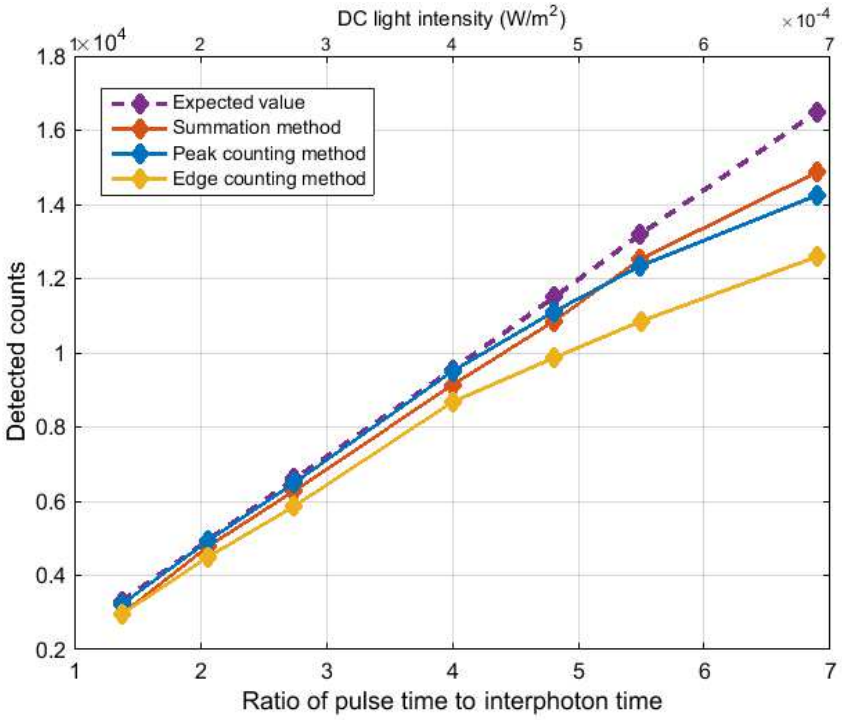


Figure 4.9: Performance evaluation of three photon counting methods at different light levels

4.3 Comparison between Photon counting mode and Analogue mode

Analogue mode is an alternative method suggested by the manufacturer to process the output signal of the MPPC module. The analogue mode directly measures the amplitude of the output signal from the MPPC. Compared to the photon counting mode, the analogue mode does not count pulses from the output signal. To compare the performance difference between using the photon counting mode and the analogue mode, the SNR achieved using the two modes are calculated at the same signal light level and background light level. The optical SNR achieved using the photon counting mode can be expressed as [31]

$$SNR_{optical} = \frac{\mu}{\sigma} = \frac{N_S}{\sqrt{N_S + N_b}} = \frac{N_{s_sec}T}{\sqrt{N_{s_sec}T + N_{b_sec}T}} = \frac{N_{s_sec}\sqrt{T}}{\sqrt{N_{s_sec} + N_{b_sec}}} \tag{4.6}$$

where μ is the average of the signal and σ is the total standard deviation of the signal, N_{s_sec} is the number of signal photons per second, N_{b_sec} is the number of background photons per second and T refers to the observation time. For the analogue mode, the SNR of the MPPC module can be calculated by treating the MPPC module as a shot noise limited APD. According to [56, 57],

$$\mu = e.M.N_{s_sec} \tag{4.7}$$

$$\sigma = \sqrt{2.e.bw.M.NF.\left(e.M.(N_{s_sec} + N_{b_sec})\right)} \tag{4.8}$$

$$T = \frac{1}{2.bw} \tag{4.9}$$

Based on equations (4.7) to (4.9), the optical SNR achieved by analogue mode is expressed as

$$SNR_{optical} = \frac{\mu}{\sigma} = \frac{N_{s_sec}\sqrt{T}}{\sqrt{NF\left(N_{s_sec} + N_{b_sec}\right)}} \tag{4.10}$$

where M is the gain of the MPPC, bw is the noise equivalent bandwidth and NF is the excess noise factor of the MPPC which is slightly larger than 1 [58]. Comparing equation (4.6) with equation (4.10), it can be found that, the SNR of analogue mode is slightly worse than photon counting mode.

To verify this prediction, the sensitivity difference between using the analogue mode and photon counting mode to achieve the same target BER of 7.9×10^{-4} based on OOK at different data rates were tested in the dark. For each sensitivity test, the same procedures were used. At the transmitter, the PRBS signal is generated and modulated to a digital OOK signal using MATLAB running on a PC. The output data from the PC is sent to an Agilent 81150A arbitrary waveform generator (AWG) to convert the modulated digital signal to the analogue signal to drive the RCLED (RC650). At the receiver, a 650-nm band-pass optical filter was placed over the MPPC. A high-resolution oscilloscope, LeCroy HDO6014-MS, captured the output signal of the SPAD array. The received data is offline processed using a PC.

For the analogue mode, the output signal is first synchronised with the transmitted signal and then low pass filtered, using a 4th order butterworth filter with a cut-off frequency equal to the data rate and decoded to binary bits using the searched optimum threshold. By comparing with the original transmitted bits, the BER of the analogue mode is calculated. If the measured BER equals the target BER of 7.9×10^{-4}, the optical power was measured using a power meter. Otherwise, the optical power was decreased if the measured BER is less than the target BER or increased if the measured BER is higher than the target BER.

For the photon counting mode, after synchronisation with the transmitted signal, the summation method is used to count pulses within each bit. The photon counts within each bit are converted to the binary bit using the optimum threshold. Com-

paring the decoded bits with the original transmitted bits, the BER achieved using photon counting mode is calculated. If the measured BER equals to the target BER of 7.9×10^{-4}, measure the optical power using a power meter. Otherwise, the optical power was decreased if the measured BER is less than the target BER or increased if the measured BER is higher than the target BER.

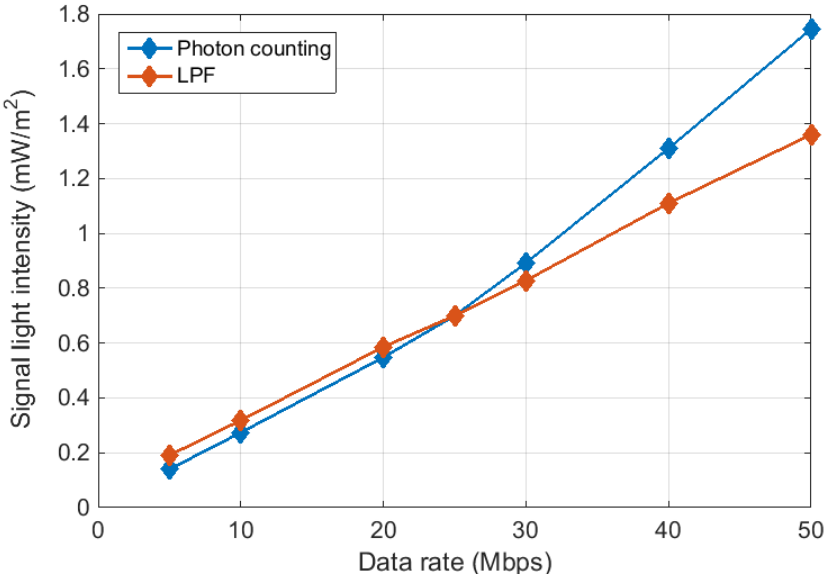


Figure 4.10: Comparison between the photon counting mode and analogue mode at different data rates measured in the dark.

Experimental results are shown in figure 4.10. It can be seen that the photon counting mode is slightly better when the data rate blow 25 Mbps, which is consistent with the previous exception. However, when the data rate is higher than 25 Mbps, the analogue mode is better. This is because the photon counting accuracy of the summation method degrades due to the pulse pile-up effect is getting significant at high light levels. Since the analogue mode does not suffer from the pile-up effect at high light levels, photon counting mode loses its advantages. Therefore, after 25 Mbps, the analogue mode is the optimum signal detection method to process the output signal of the MPPC module.

4.4 OOK link results using an MPPC

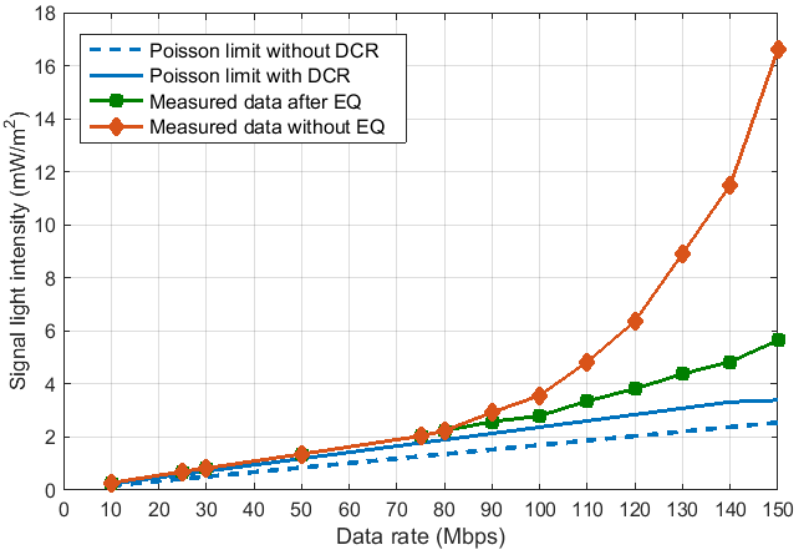


Figure 4.11: The transmitter signal intensity required to achieve a BER of 7.9×10^{-4} at different data rates in the dark when the MPPC module is used as the receiver. In the figure, the red curve refers to the signal intensities measured without using EQ, the green curve refers to the signal intensities measured after using EQ, the solid blue curve refers to the calculated signal intensity based on Poisson distribution when dark counts are considered and the dashed blue curve refers to the calculated signal intensity based on Poisson distribution without considering dark counts.

Using the analogue mode, the sensitivities of this MPPC module at higher data rates were investigated. For each sensitivity test, the same measurement procedures for the analogue mode BER test mentioned in the section 4.3 were used. The measurement results at different data rates are shown in figure 4.11. It can be seen that EQ significantly improves the BER performance when the data rate is higher than 100 Mbps. This result suggests that ISI becomes significant when the symbol time becomes less than the pulse time of the MPPC module. The dashed blue curve in figure 4.11 represents the theoretical signal intensities S_I which are calculated based on equation 4.11.

$$S_I = \frac{\frac{N_S}{PDE} \times E_p}{A \times T} \tag{4.11}$$

where N_S is the detected photons per bit, T is the bit time, E_p is the single photon energy, and A is the total area of the MPPC. N_S is calculated by equation (2.8) when dark counts is not considered (N_0 equals 0), which refers to the Poisson limit N_{PL}. The solid blue line is calculated using the same equations as the dashed blue line but considering dark counts (N_0=dark counts per bit). The ratio between the dashed blue line and the solid blue line indicates the impact of dark counts at different data rates which can be calculated as

$$\frac{S_{I\ with\ DCR}}{S_{I\ without\ DCR}} = \frac{N_S}{N_{PL}} \tag{4.12}$$

In equation 4.12, N_{PL} is a constant and N_S changes with N_0. Since the dark counts per bit decrease with the increase of the data rate, the tendency of this ratio against data rate has an opposite tendency of N_S against N_0. Figure 4.12 shows the ratios at different data rates. As expected, the impact of dark counts decreases with the increase of the data rate and the curve in this figure has an inverse shape to that in figure 3.13.

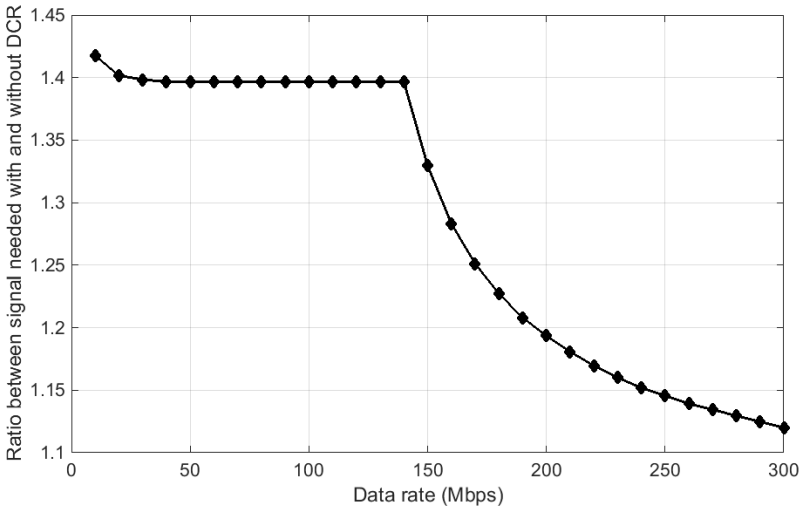


Figure 4.12: The impact of DCR accessed by the ratio between the signal counts required with and without dark counts at different data rates.

Comparing the green curve and the dashed blue curve in figure 4.11, it can be

found that this MPPC module requires 1.64 times more transmitted power than the ideal photodetector (no dark counts) at 100 Mbps in the dark condition. When dark counts are considered, the MPPC module requires 1.17 times more detected photons per bit than the value calculated based on equation (2.8). Despite this power penalty and a PDE of 8%, this SPAD-based receiver achieves a BER of 7.9×10^{-4} at 100Mbps with 80% of the power required by the typical APD-based receiver. As expected, a receiver using a larger SPAD array is more sensitive than a receiver using an APD in the dark condition.

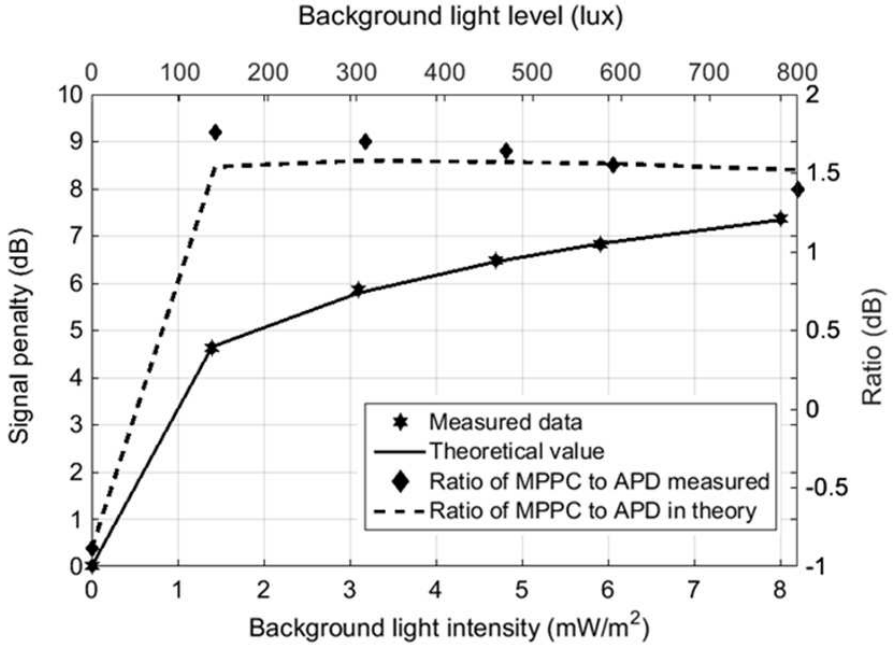


Figure 4.13: The required signal penalty for the MPPC to achieve a BER of 7.9×10^{-4} at various background light intensities. In this figure the data (stars) is compared to the predictions of equation (2.8).

When the MPPC module is operated within the ambient light condition, more signal power is required to compensate the increase of the background light noise. To investigate the power penalty required by this MPPC module to maintain the target BER of 7.9×10^{-4} at 100 Mbps against different background light levels, sensitivities measurements were done by following the same experimental procedures used in section 3.5.4. The measurement results are shown in figure 4.13. The solid

curve in the figure shows the theoretical signal penalty required to achieve the target BER, which is calculated based on the Poisson model, equation (2.8). It can be seen that equation (2.8) can be used to estimate the power penalty required by the MPPC module to maintain the target BER in the presence of ambient light. Comparing with the power penalty required by APD (figure 3.15), it can be seen that the MPPC module requires more power penalty than the APD to operate in ambient light. This is because the shot noise is the only dominating noise source for the SPAD-based receiver. Apart from the shot noise, the APD-based receiver also suffers from excess noise and thermal noise in the electronics associated with the APD. In that case, the SPAD-based receiver requires more additional transmitted power to be operated in ambient light. The measurement results in the dark show that, although the PDE is only 8%, this MPPC module is still more sensitive to the light than the APD. Consequently, the MPPC module suffers from more background light noise than the APD when both the MPPC module and the APD are presented in the ambient light. The ratio between the powers required by the MPPC module and the tested APD to achieve the same target BER at different ambient light conditions is also shown in figure 4.13. It shows that the tested APD is more sensitive than the tested MPPC module to achieve the same target BER within the ambient light condition.

Experimental results shown in figure 3.15 and figure 4.13 indicate that the power penalty required by APD and SPAD array against ambient light can be estimated by using equations (3.26) and (2.8). Therefore, when the required signal light intensities in the dark had been measured, these two equations were used to estimate the signal light intensities required by the MPPC module and the APD to achieve a target BER of 7.9×10^{-4} at 100 Mbps within the ambient light. The results in figure 4.14 show that a receiver containing an MPPC with a PDE of 8% and a power penalty of 1.17 is expected to require more transmitter power than the APD-based receiver at background light intensities of more than 30 $\mu W/m^2$. Consequently, at the typical

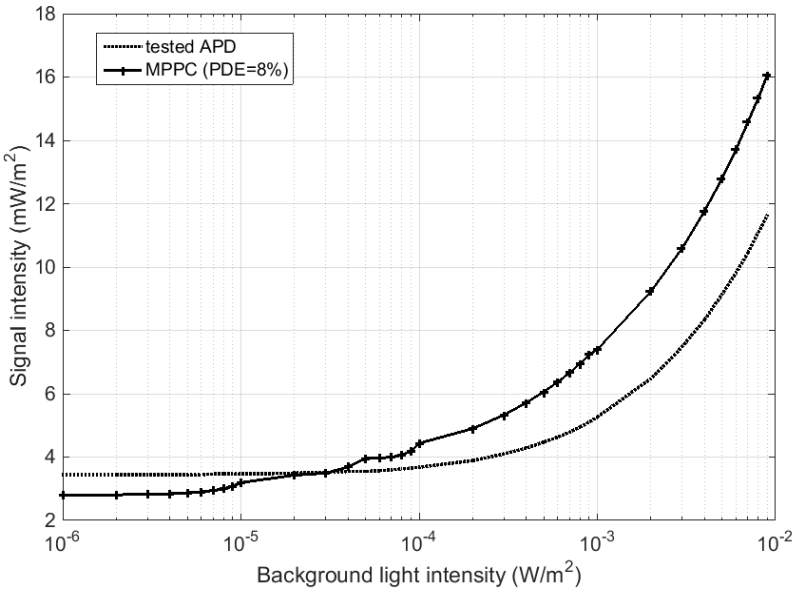


Figure 4.14: The estimated signal intensities required by the tested APD-based receiver and receivers including MPPC to achieve the target BER at different intensities of background light.

ambient light condition (500 lux [59]), the MPPC requires 1.45 times more transmitted signal intensity than the APD to achieve the target BER.

4.5 Sensitivity improvement by increasing PDE

In order to match the APD's performance, the PDE of the MPPC module should be increased. When the Gaussian model (equation (3.15)) is valid for both the APD and the SPAD array, the PDE required for the SPAD array to match the performance of an APD can be estimated by comparing the Q parameters of the two devices under the same conditions.

The noise power change of the tested APD at different background light intensities to achieve the target BER (7.9×10^{-4}) is shown in figure 4.15. The first solid line shows the total shot noise at level one generated by the dark current I_d, background light and signal light, which is calculated using

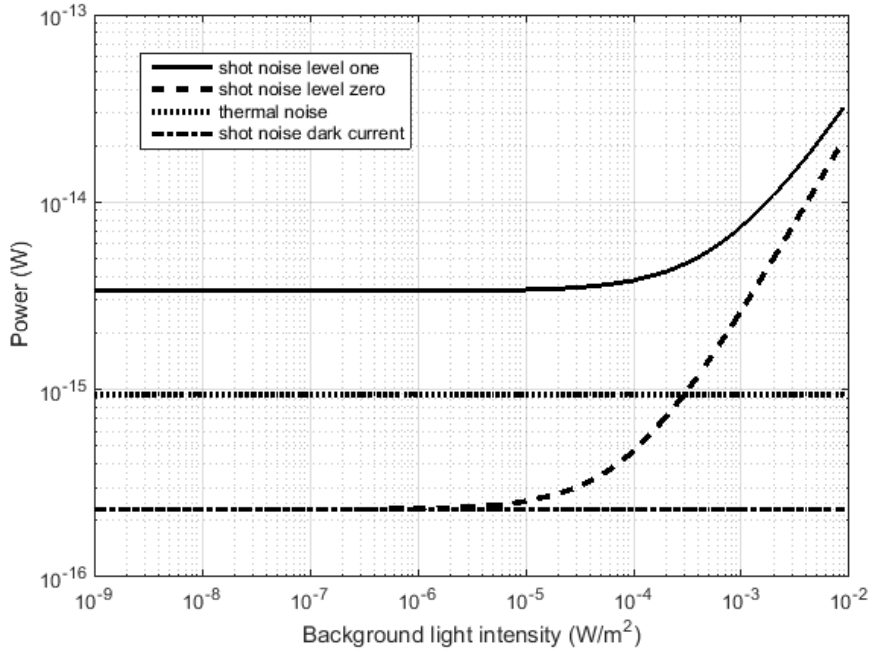


Figure 4.15: APD noise power analyses at different background light intensities.

$$2e.\left(R.\left(P_b + P_s\right) + I_d\right).bw.m^{x+2} \tag{4.13}$$

The dashed line shows the total shot noise from level zero generated by the dark current and the background light, which can be calculated using

$$2e.\left(R.P_b + I_d\right).bw.m^{x+2} \tag{4.14}$$

The dotted line shows the thermal noise, and the dash-dotted line shows the shot noise purely generated by the dark current. This figure shows that for this tested APD operated at 650 nm, shot noise power becomes the dominant noise source when the background light intensity is higher than 5 mW/m^2 which corresponds to the 500 lux indoor ambient light condition. Since the shot noise from the dark current is negligible compared to the other shot noise sources, when the shot noise becomes the dominant noise of the APD, the Q parameter for APD can be expressed as

$$Q_{APD} = \frac{Int_S \sqrt{\frac{QE.\lambda.A_{APD}}{1240.m^x}}}{\sqrt{2e.bw}(\sqrt{(Int_S + Int_b)} + \sqrt{Int_b})} \tag{4.15}$$

where A_{APD} is the active area of the APD, Int_S is the signal intensity, Int_b, is the background light intensity, bw is the noise equivalent bandwidth of the detector, QE is the quantum efficiency, λ is the operation wavelength and m^x is the excess noise factor.

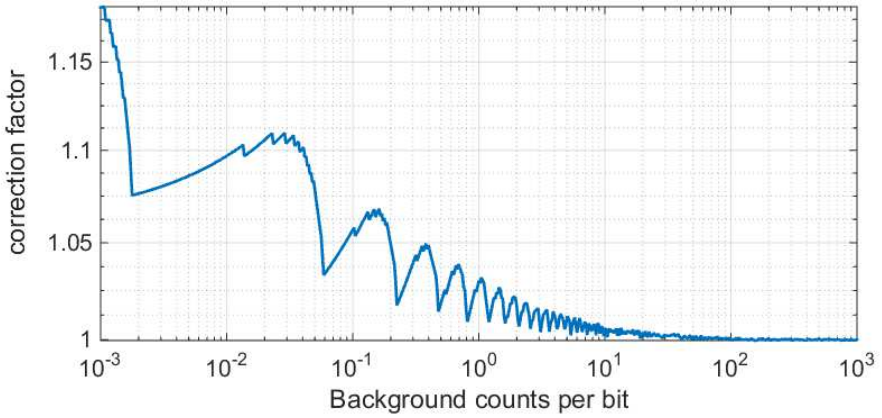


Figure 4.16: Correction factor required to compensate the Q parameter calculated by equation (3.19). This figure is obtained using data in figure 3.11 at the BER of 10^{-3}.

For the SPAD array, the results in figure 3.13 suggest that the Poisson model, equation (2.8), is more accurate than the Gaussian model, equation (3.15). However, the Poisson model can be accurately approximated by the Gaussian model when the background counts per bit are higher than 2 counts per bit. Therefore, when the detected background counts per bit are higher than 2 counts per bit, the Q parameter calculated by equation (3.19) can be directly used to estimate the BER performance of a SPAD-based receiver. When the detected background counts per bit are less than 2 counts per bit, the Q parameter (equation (3.19)) overestimates the BER value. Therefore, in order to use the Gaussian model(equation (3.15)) to estimate the BER achieved by a SPAD-based receiver accurately, a correction factor has to be

added to equation (3.19). The correction factor is calculated by

$$correction_factor = \frac{Q_{actual}}{Q_{est}} \tag{4.16}$$

where Q_{actual} is the true Q parameter calculated by the equation (3.17) using the actual BER and Q_{est} is calculated using (3.19). Figure 4.16 shows the correction factors at different background counts per bit. This figure shows that the correction factor is higher than 1. For the worst case (the system suffers from a large number of background counts), the correction factor is very close to 1. Then, the Q parameter of a SPAD-based receiver with a total area of A_{SPAD} can be calculated as

$$Q_{SPAD} = \frac{Int_S.\sqrt{\frac{PDE.\lambda.A_{SPAD}}{1240}}}{\sqrt{2bw}.(\sqrt{(Int_S + Int_b)} + \sqrt{Int_b})} \tag{4.17}$$

When the electrical bandwidth of both devices is sufficient to the support a data rate of $1/T$, no power penalty is required for compensating ISI. Then the Q parameter ratio between SPAD and APD is given by

$$\frac{Q_{SPAD}}{Q_{APD}} = \sqrt{\frac{m^x \times PDE \times A_{SPAD}}{QE \times A_{APD}}} \tag{4.18}$$

This ratio can be used to compare the sensitivity of a particular SPAD array and a particular APD in the typical indoor ambient light condition (500 lux) when there is no ISI. If this ratio is larger than 1, the SPAD array is more sensitive than APD. Otherwise, APD is better.

For the tested MPPC module, at the typical ambient light condition (500 lux), the background counts per bit are higher than 39 counts per bit. The total area of tested MPPC module and the active area of the tested APD are the same. Therefore, the sensitivity of the tested MPPC and APD can be compared by

$$\frac{Q_{SPAD}}{Q_{APD}} = \sqrt{\frac{m^x \times \ PDE\,(\lambda)}{QE\,(\lambda)}} \tag{4.19}$$

Due to the longer pulse time of the MPPC module and the additional system noise exists, the power penalty PP has to be considered, and hence equation (4.19) is given by

$$\frac{Q_{MPPC}}{Q_{APD}} = \sqrt{\frac{m^x \times \ PDE\,(\lambda)}{QE\,(\lambda) \times PP}} \tag{4.20}$$

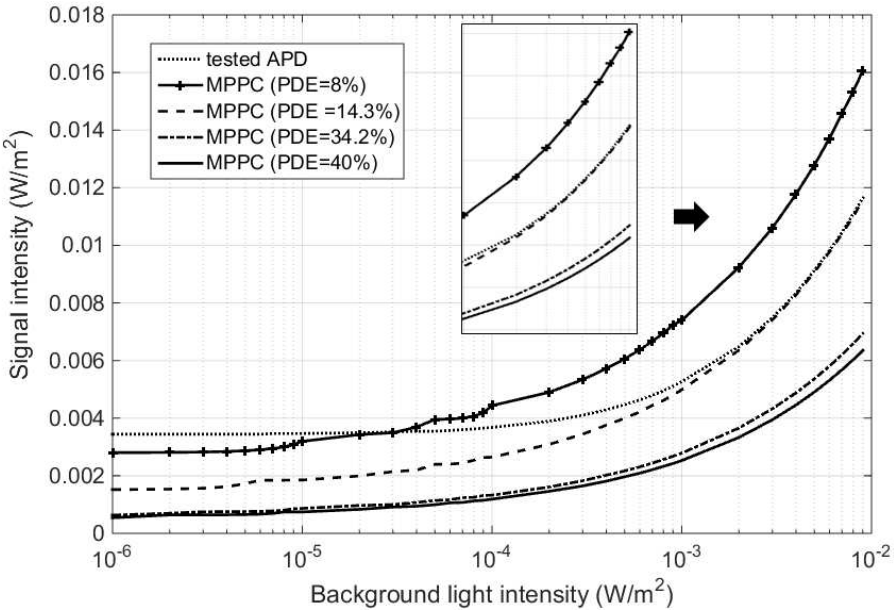


Figure 4.17: The estimated signal intensities required by the tested APD-based receiver and receivers including MPPCs with different PDEs to achieve the target BER at different background light intensities.

For the tested APD, $m^x = 5.3$ since x equals 0.36 and the measured optimum gain is 105. At 650 nm, the quantum efficiency (QE) of the APD is approximately 65% and the power penalty for the tested MPPC is 1.17. Equation (4.20) therefore suggests that an ideal SPAD array will need a PDE of 14.3% to match the Q parameter of this APD when shot noise from the detected light is the dominant noise source. The dashed curve in figure 4.17 shows the simulation result of the tested MPPC module

with a 14.3% PDE based on equation (2.8) with a power penalty of 1.17. This result confirms that equation (4.20) gives an accurate estimate of the MPPC PDE that matches the performance of the tested APD.

The recently released MPPC has already achieved a significant higher PDE than this tested MPPC [53]. The maximum PDE of the MPPC S12571-015C has already achieved 40% [53]. The performance of an MPPC with 40% PDE has been simulated based on equation (2.8) assuming no power penalty is required , and the results are shown in figure 4.17. The simulation results show that, within the normal ambient light condition, the APD is expected to require 1.8 to 2.1 times more signal intensity than the new released MPPC. However, this new device may need more power than the ideal receiver. Therefore, figure 4.17 also shows the simulation results of the MPPC with a PDE of 34.2% which corresponding to the PDE of 40% and power penalty 1.17. In this case, within the normal ambient light condition, the APD is expected to require 1.7 to 1.9 times more signal intensity than the new MPPC.

4.6 Summary

In this chapter, the performance of a larger SPAD array is tested using an MPPC module C11209-110 which consists of 10000 SPADs. There are two modes to process the output signal of the MPPC. At low light levels, the output signal of the MPPC consists of well-separated pulses and hence the number of detected photons can be counted by counting the pulses using photon counting mode. Three photon counting methods were compared. Results show that the summation method is better than the peak counting method and the edge counting method. At high light levels, the pulses from the MPPC overlaps. When the incident light intensity is higher than 0.4 mW/m^2, photon counting mode starts to lose the counting accuracy. According to the manufacturer, analogue mode is an alternative method to process the output

signal of MPPC at high light levels. The performance of photon counting mode and analogue mode are compared in an OOK link. Results show that analogue mode should be selected when the data rate is higher than 25 Mbps.

Using the analogue mode, the sensitivities of the MPPC at higher data rates were tested. Results suggest that the ISI is tolerable at the data rate of 100 Mbps using this MPPC module. Despite the ISI, dark counts also impact the MPPC based receiver's performance. Result shows that the impact of the dark counts decreases with the increase of the data rate. In the dark, this MPPC based receiver is more sensitive than the tested APD at 100 Mbps. Results show that this MPPC based receiver requires only 80% of the power needed for the tested APD-based receiver to achieve the target BER, which verifies that larger SPAD array can be more sensitive than the APD. However, this MPPC is more sensitive to ambient light than the APD. As a result, this MPPC requires more power to compensate the impact of the background light noise than the tested APD in the typical indoor ambient light environment.

To match the APD's performance in typical ambient light conditions, the sensitivity of the SPAD-based receiver can be further improved by improving the PDE. A criterion, equation (4.18), that determines when the sensitivity of a SPAD-based receiver is superior to an APD-based receiver in the typical indoor lighting condition is presented. Using this criterion, the minimum PDE required by the tested MPPC module to match the APD's sensitivity in the normal ambient light condition has been calculated. Results suggest that the tested MPPC module needs a 14.3% PDE to match the APD's performance in the normal indoor ambient light condition. A newly released MPPC has already achieved a PDE of 40%. Simulation results suggest that a receiver containing a SPAD array with a 40% PDE is expected to be significantly more sensitive than the APD-based receiver within typical indoor ambient light conditions.

Chapter 5

4-PAM VLC with a SPAD-based receiver

5.1 Introduction

Results in the previous chapter suggest that a SPAD-based receiver can be more sensitive than the APD-based receiver. Therefore, using a SPAD-based receiver can increase the achievable SNR of the VLC system and hence the data rate. In this chapter, results are presented which show how the increased SNR can be exploited to support 4-PAM. This chapter begins with a detailed description of the optimum strategy for setting the 4-PAM symbol levels and thresholds for the SPAD-based receiver. Based on the optimum strategy, a practical estimation method is then investigated to estimate the actual 4-PAM power levels required by the tested MPPC module C11209-110 to achieve the target BER of 10^{-3}. The accuracy of this estimation method is then evaluated in a 2 Mbps 4-PAM link. The 2 Mbps data rate is useful for low data rate applications [60–62]. For high data rate VLC, the MPPC has to be operated in the analogue mode. A 200 Mbps data rate 4-PAM test is presented in this chapter. Before performing the link test, the non-linear response of the tested

MPPC module is measured and fitted with the optimum dead time model. Results in previous chapters suggest that ISI occurs when the symbol time is 10 ns. A simple method for estimating the power penalty required for employing DFE to correct ISI in 4-PAM is presented. At the end of this chapter, with a practical method for determining 4-PAM levels at high data rate, a 200 Mbps data rate is demonstrated using the tested MPPC module both in the dark and in the normal indoor ambient light condition(500 lux). The accuracy of using the simple method to estimate the power penalty required for correcting ISI using DFE is evaluated.

5.2 Numerical model of 4-PAM

For 4-PAM, assuming errors only occur within the nearest symbols, the total SER (symbol error rate) can be calculated as

$$SER_{total} = \sum_{n=1}^{3} SER_n \tag{5.1}$$

where SER_n refers to the SER between the adjacent levels $level_{n-1}$ and $level_n$(n = 1,2,3). There are two coding schemes can be applied to encode 4-PAM symbol levels which are shown in table 5.1.

symbol level	$symbol_0$	$symbol_1$	$symbol_2$	$symbol_3$
Gray Code	00	01	11	10
Binary Code	00	01	10	11

Table 5.1: Gray Code vs Binary Code.

When Gray code is applied, one symbol error only generates one bit error. Since each 4-PAM symbol carries two binary bits, the BER of 4-PAM is half of the SER of 4-PAM, and hence the total BER of 4-PAM can be calculated as

$$BER_{total} = \frac{1}{2} SER_{total} = \frac{1}{2} \sum_{n=1}^{3} SER_n \tag{5.2}$$

When Binary code is applied, one symbol error between $level_1$ and $level_2$ generates two bit errors. In that case, the BER achieved using Binary Code is calculated as

$$BER_{total} = \frac{1}{2} SER_1 + SER_2 + \frac{1}{2} SER_3 \tag{5.3}$$

For an ideal photon counter based 4-PAM system, there is no thermal noise and ISI. In that case, the received 4-PAM symbols are only determined by the number of detected photons within each symbol period. Therefore, the symbol error rates SER_n can be calculated based on the Poisson distribution, which is expressed as

$$SER_n = \frac{1}{4} \sum_{k=th_n+1}^{\infty} \frac{{N_{n-1}}^k}{k!} e^{-N_{n-1}} + \frac{1}{4} \sum_{0}^{k=th_n} \frac{{N_n}^k}{k!} e^{-N_n} \tag{5.4}$$

where N_{n-1} and N_n are the number of photons per symbol within symbol levels $level_{n-1}$ and $level_n$, and th_n is the optimum decision threshold between $level_{n-1}$ and $level_n$.

5.2.1 Comparison between Gray Code and Binary Code

To quantify the difference between using the Gray Code and the Binary Code, the BERs obtained using the two coding methods based on the same symbol level arrangements which ensure the same SER are compared. Simulation results are shown in figure 5.1 when background count is 1. It can be found that the Gray coding requires 20.3 photons per bit to achieve the BER of 10^{-3}. For binary coding, it requires 21.3 photons per bit to achieve the same BER which is 1.05 times more than the Gray Coding. This result suggests that Gray Code is the optimum scheme for coding the 4-PAM signal.

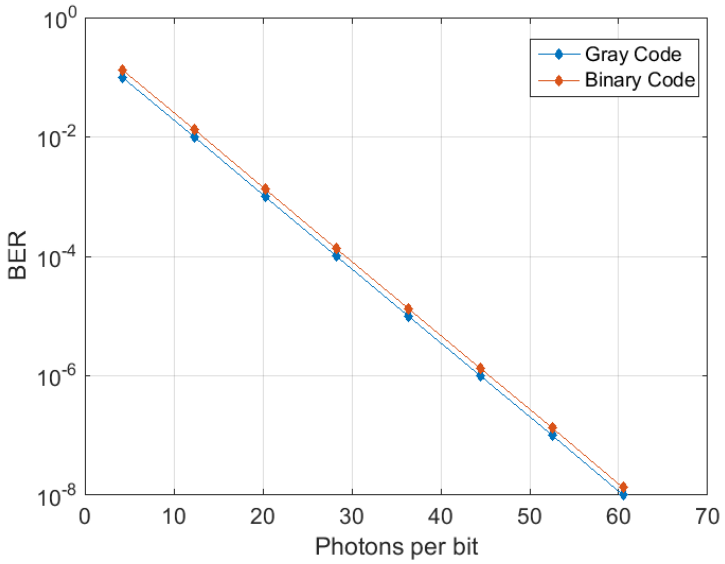


Figure 5.1: BER differences between using Gray Code and Binary Code at the same symbol levels arrangement when background count is 1.

5.2.2 Strategy to determine the optimum 4-PAM symbol levels

For a particular background count level and BER, there is an optimum choice of symbol levels for 4-PAM to achieve the highest sensitivity (the minimum number of photons per bit). The arrangement of 4-PAM symbol levels is determined by the SER distribution between the adjacent symbol levels. Equation (5.2) shows that there is a trade-off within SERs arrangements between adjacent levels. For example, when signal $level_1$ is reduced, SER_1 between $level_0$ and $level_1$ is increased and the SER_2 between $level_1$ and $level_2$ is reduced. If the decrease of SER_2 is less than the increase of SER_1, in order to maintain the total BER, more signal photons are required by $level_3$ to reduce SER_3. One strategy to find the optimum 4-PAM symbol levels is to do a comprehensive search. Based on equation (5.2) and (5.4), the sensitivities achieved at different combinations of error distribution were calculated first. The error distribution that achieves the highest sensitivity was then used to determine the optimum signal arrangement. The dashed line in figure 5.2 shows the optimum signal

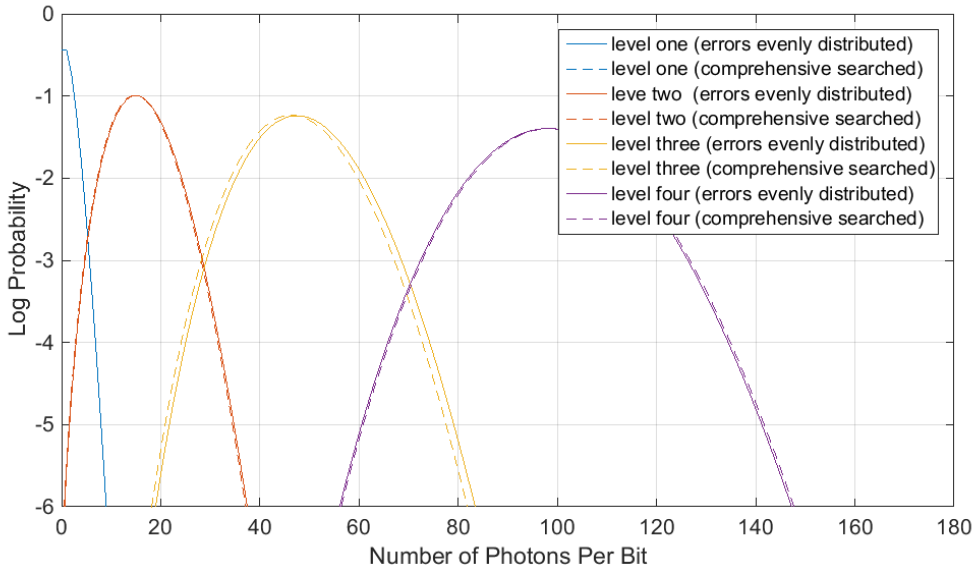


Figure 5.2: Signal levels arrangement to achieve a target BER of 10^{-3} when background count equals to 1.The dashed lines are the optimum signal levels based on comprehensive search. The solid lines refer to the signal levels which ensure errors are evenly distributed.

arrangement based on the comprehensive search strategy (4525 possible combinations of error distribution are tested) to achieve a target BER of 10^{-3} when the background count is 1. This optimum signal level arrangement is achieved when SER_1 is 7.2×10^{-4} , SER_2 is 8.2×10^{-4} and SER_3 is 4.6×10^{-4}, which only requires 20.3 photons per bit to achieve the target BER 10^{-3}.

Due to the long searching process, optimisation using a comprehensive search strategy can be inconvenient. A more convenient strategy that has been investigated is to set the 4-PAM symbol levels based on evenly distributed errors between neighbouring levels. The solid line in figure 5.2 shows the signal levels arrangement based on the errors evenly distributed strategy to achieve the same target BER of 10^{-3}. Compared to the comprehensive searched result, this strategy tolerates fewer errors at level 1, and 2 and hence more signal photons are required to represent level 1 and level 2. At the highest symbol level, this strategy tolerates more errors, and hence fewer signal photons are required at level 3. As the decrease of signal photons at level

3 is less than the increase of signal photons at level 1 and 2, 0.1 more photons per bit are required by this convenient strategy than the comprehensive searched strategy. Compared with the achievable measurement accuracy, this 0.5% difference is negligible.

One assumption has been made when determine the 4-PAM levels using equation (5.2) is that errors only occur between neighbouring symbols. However, in reality, there is a probability that errors could occur within the signal levels that are not close to each other. The total SER distributions between all symbol levels of 4-PAM in figure 5.2 are shown in table 5.2 when the searched optimum signal level arrangement is used. It can be seen that errors within the symbol levels that are not close to each other are negligible compared to the target BER, which suggests that assuming errors only occur within the adjacent levels is a sensible choice in practical 4-PAM system design.

Tx/Rx	Level 0	Level 1	Level 2	Level 3
Level 0	0	1.49×10^{-4}	1.15×10^{-35}	8.23×10^{-117}
Level 1	5.67×10^{-4}	0	2.88×10^{-4}	1.20×10^{-28}
Level 2	3.00×10^{-17}	5.30×10^{-4}	0	2.29×10^{-4}
Level 3	1.71×10^{-41}	1.47×10^{-20}	2.29×10^{-4}	0

Table 5.2: Total SER distribution between signal levels in figure 5.2.

Table 5.3 compares the sensitivity difference (averaged photons per bit) between using different signal levels arrangements at different background counts to achieve the same target BER of 10^{-3}. For 4-PAM, each symbol level carries two bits. Therefore, the averaged photons per bit are calculated by summing the 4 symbol levels together and then divided by 8. It can be seen that using the searched optimum symbol levels is slightly better than using the symbol levels determined by errors evenly distributed strategy. The gap is increasing as background counts increased. Since the difference

Background counts per bits	1	10	50	100
BER achieved	10^{-3}	10^{-3}	10^{-3}	10^{-3}
Photons per bits [45]	24.2	39.6	81.1	122.6
Photons per bits (errors are evenly distributed)	20.4	35	72.6	110.8
Photons per bits (comprehensive searched results)	20.3	34.6	72.2	110.3
Differences between errors evenly distributed and optimum searched results	0.1	0.4	0.4	0.5

Table 5.3: Comparison between different signal level arrangements.

is small compared to the average value, using the errors evenly distributed strategy for setting the 4-PAM symbols is a sensible choice. Compared to the results in [45], it can be seen that the new results are better. This is because results in [45] did not decode the 4-PAM symbol to the binary bits using Gray Code. Consequently, this result calculated the photons per bit required to get the SER equals to 10^{-3} rather than the BER.

5.2.3 Impact of background count on 4-PAM

Using errors evenly distributed strategy, the impact of background count on 4-PAM has been investigated. When the background count is 0, no photon is transmitted at symbol 0 if the transmitter is fully turned off at symbol 0. Consequently, no event is counted at symbol 0. In that case, the optimum decision threshold for separating the received symbols 0 and 1 is set to 0 since the effective decision threshold in the CDF (cumulative distribution function) of Poisson distribution is an integer. As a result, SER_1 equals to the probability of no photon is detected within the received symbol 1 when symbol 1 is transmitted. When the background count per symbol is less than

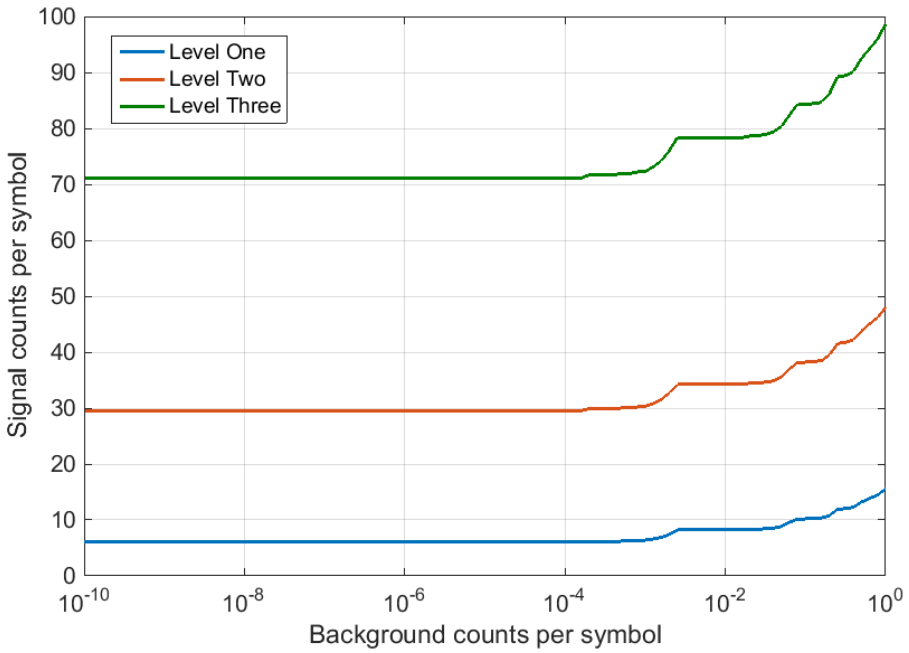


Figure 5.3: Signal levels change against background counts to achieve a BER of 10^{-3}.

1, increasing the background count rate increases the probability that one count is detected at symbol 0. When the optimum threshold equals to 0, this will increase the probability of the transmitted symbol 0 is detected as symbol 1. However, when the probability of symbol 0 is detected as symbol 1 is negligible compared to target SER_1, no power penalty will be required for symbol 1. Otherwise, to maintain the SER_1, more power is required for symbol 1. Accordingly, power levels for symbol 2 and 3 are required to be increased to maintain the same BER.

Figure 5.3 shows the 3 signal levels of 4-PAM required to maintain a target BER of 10^{-3} at different background counts calculated by equation (5.2) and equation (5.4). As expected, symbol 2 and 3 increase simultaneously with symbol 1 to compensate the background noise. The BER requirements for conventional applications, such as telephony speech, voice over IP and video conference tools, are in a range of 10^{-3} to 10^{-6} [63]. Therefore, the impacts of the background count at different target BERs (10^{-3} to 10^{-6}) are investigated, and the result is shown in figure 5.4. Similar to

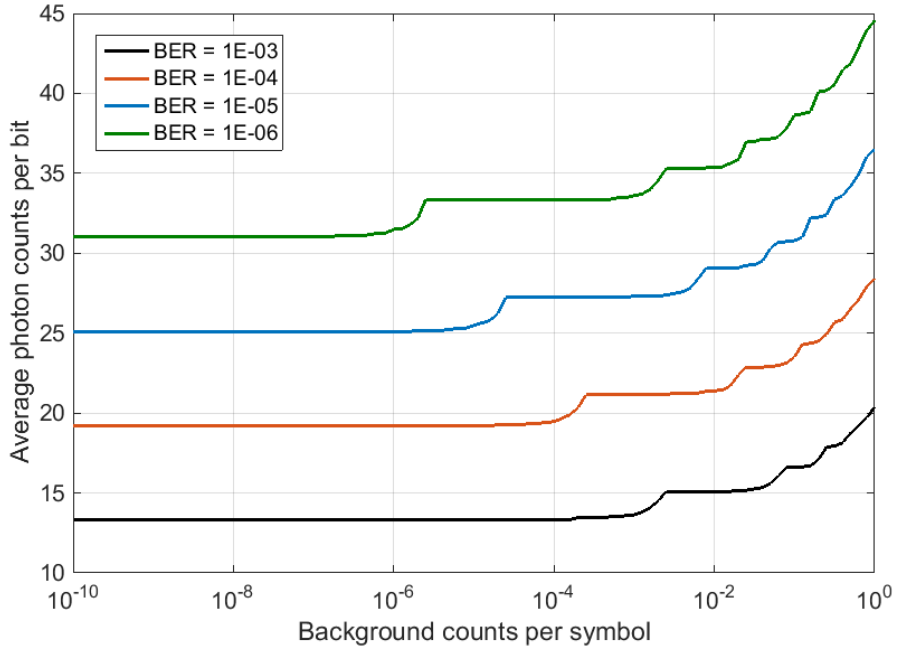


Figure 5.4: Averaged photon counts per bit required to maintain different target BERs at different background counts .

the result shown in figure 5.3, the impact of background noise is negligible when the background counts per symbol are less than $SER/13$. When the impact of background counts is negligible, the error probability generated by the background counts which make symbol 0 is detected as symbol 1 is negligible. In this case, the optimum threshold for calculating SER_1 is 0 and the SER_1 is determined by the probability that a symbol 1 is detected as symbol 0 which is generated by no photon is detected at symbol 1. When the background counts per symbol is less than one, the background per symbol can be regarded as the probability that one background counts occur within a symbol time. Therefore, result in figure 5.4 indicates that the impact of background count is negligible when the probability of one background count occurs within a symbol period is 13 times less than the error probability generated by no photons are detected at symbol 1 within a symbol period. Moreover, figure 5.4 also shows that the averaged photons per bit required to achieve a particular BER increases less quickly than the number of background counts.

5.2.4 Comparison between Poisson model and Gaussian model

After Gray Codes are used, the total BER for 4-PAM is expressed as

$$\begin{aligned} BER =& \frac{1}{2} \times [P\left(0\right) P(1|0) + P\left(1\right) P(0|1) + P\left(1\right) P(2|1) + P\left(2\right) P(1|2) \\ &+ P\left(2\right) P(3|2) + P\left(3\right) P(2|3)] \end{aligned} \tag{5.5}$$

where

$$P\left(0\right) = P\left(1\right) = P\left(2\right) = P\left(3\right) = \frac{1}{4} \tag{5.6}$$

The Poisson distribution can be approximated by the Gaussian distribution when a large number of photons are detected. Based on the Gaussian distribution, $P(L-1|L)$ and $P(L|L-1)$ in equation (5.5) can be expressed as

$$P(L-1|L) = \frac{1}{2} erfc\left(\frac{N_L - N_{thL}}{\sigma_L \sqrt{2}}\right) \tag{5.7}$$

$$P(L|L-1) = \frac{1}{2} erfc\left(\frac{N_{thL} - N_{L-1}}{\sigma_{L-1} \sqrt{2}}\right) \tag{5.8}$$

where L =1,2,3 corresponds to the three symbol levels of 4-PAM, N_L is the average number of detected photons encoded in level L, N_{thL} refers to the optimum decision threshold between symbol $level_L$ and $level_{L-1}$, and σ_L^2 refers to the noise power at $level_L$.

Figure 5.5 shows the simulation results based on the Poisson model, equation (5.2) and (5.4), and the Gaussian model, equation (5.5) to (5.8). It can be seen that the curve calculated by the Gaussian model is getting indistinguishable from the curve calculated by the Poisson model with the background counts per symbol is getting increased. To quantify the difference between using the Gaussian model and the Poisson model, based on the data in figure 5.5, the fractional error is calculated using the equation (3.20). The calculation results are shown in figure 5.6. It can be

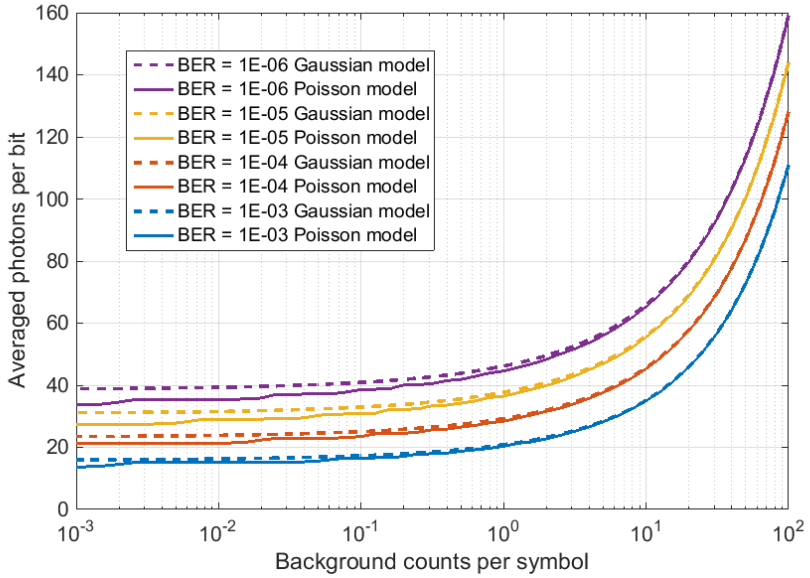


Figure 5.5: Photon counts per bit required to maintain different target BERs at different background counts, the dashed line is calculated based on Gaussian model equation (5.5) to (5.8), and the solid line is calculated based on Poisson model equation (5.2) and (5.4).

seen that, at the target BER of 10^{-3}, the difference between using Gaussian model and Poisson model is less than 1% when the background counts per symbol are higher than 2 counts per symbol. Therefore, using the Gaussian model is an accurate approximation to the Poisson model when the background counts per symbol are higher than 2 counts per symbol.

5.3 A practical method to estimate the optimum 4-PAM symbol levels

The accuracy of using the ideal Poisson model, equations (5.2) and (5.4), to determine the optimum 4-PAM symbol levels has been measured using the tested MPPC module in the photon counting mode in the dark. Results in figure 4.9 show that the photon counting mode (summation method) of the tested MPPC module counts photons

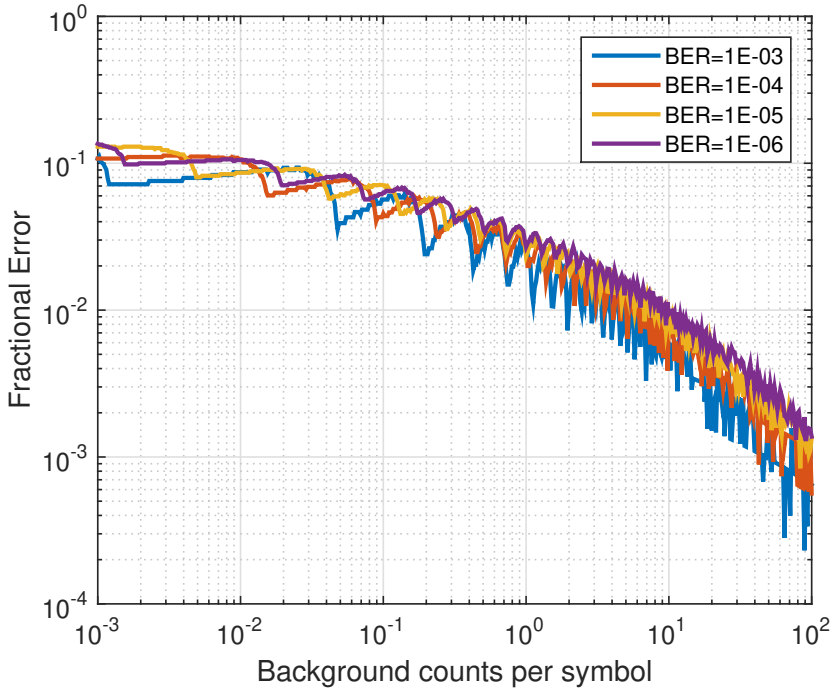


Figure 5.6: Fractional error of the Gaussian model equation (5.5) to (5.8).

accurately when the signal intensity is below 0.4 mW/m^2. Therefore, in order to ensure the photon counting accuracy at each 4-PAM symbol level, the signal intensity to generate the highest symbol level of 4-PAM (level 3) is required to be less than 0.4 mW/m^2. For a fixed 4-PAM symbol arrangement, the signal intensities required by the tested MPPC module to generate the highest symbol level (level 3) in the dark is related to the data rate. Based on the errors evenly distributed strategy and equation (5.2) and (5.4), the estimated signal intensities required by the tested MPPC module to generate the highest 4-PAM level(symbol 3) at different data rates are shown in figure 5.7. This result suggests that the 4-PAM measurement data rate is required to be set to 2 Mbps so that the light level required by symbol 3 is below 0.4 mW/m^2.

The actual signal intensities required by the tested MPPC module for generating the 4-PAM symbols to achieve the target BER of 10^{-3} at 2 Mbps were determined experimentally. The measurement results in figure 4.11 show that there is no ISI

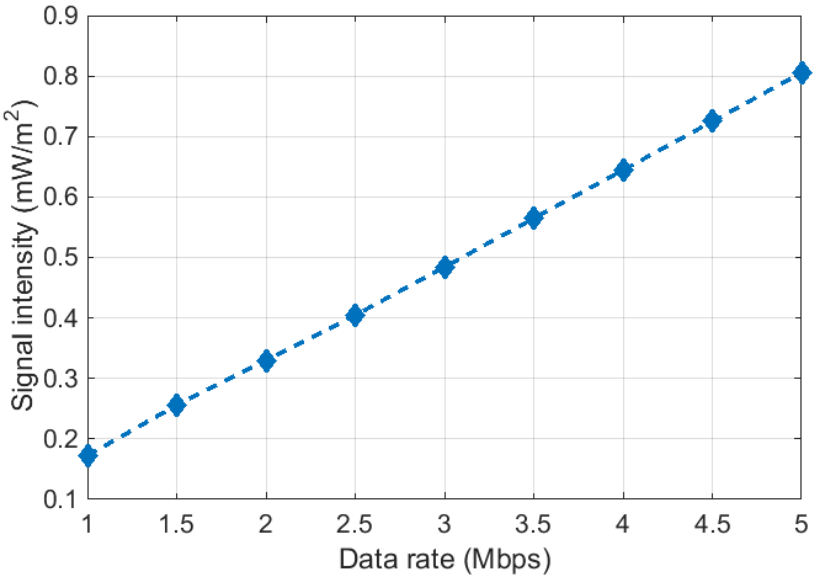


Figure 5.7: Signal intensities required by the tested MPPC module to generate level 3 at different data rates to achieve the target BER of 10^{-3} in the dark when errors are evenly distributed.

when the symbol time is set to 1 μs. Without ISI, each received 4-PAM symbol is independent of others and is only determined by the received optical power. Since errors only occur between adjacent levels, the experiment to determine the three signal symbol levels for 4-PAM can be separated into three individual OOK tests. For the first OOK test, the background light level was used as level 0, and the signal photons per bit required to generate level 1 for the target BER are searched. For the second OOK test, level 1 was used as the lowest level, and the signal photons per bit required for level 2 to achieve the target BER are searched. Finally, for the third OOK test, level 2 was used as the lowest level, and the signal photons per bit required to achieve the target BER for level 3 are searched. For each OOK test, the probability of transmitting symbol 0 and 1 are 1/2. While for 4-PAM, the probabilities of transmitting two adjacent symbols are 1/4. As a result, comparing equation (2.8) with equation (5.4), it can be seen that the BER for each OOK test is twice the adjacent symbol error rate of 4-PAM, $BER_{OOK} = 2SER_n$. When Gray coding is

applied, one symbol error only generates one bit error. Since each 4-PAM symbol carries two bits, the total SER of 4-PAM is twice the BER of 4-PAM,$SER_{total} = 2BER_{4PAM}$. When errors are evenly distributed, the SER_n is a third of the total target SER of 4-PAM, $SER_n = \frac{1}{3} \times SER_{total} = \frac{2}{3} \times BER_{4PAM}$. Therefore, the target BER for each OOK test, BER_{OOK}, is required to be set to 4/3 of the total target BER of 4-PAM. In the measurement, each OOK test follows the same procedures for the photon counting mode BER test mentioned in section 4.3.

4-PAM Symbol	Symbol 1	Symbol 2	Symbol 3
Signal intensity (W/m^2)	4.17×10^{-4}	1.63×10^{-4}	3.9×10^{-4}
Applied Voltage (V)	0.96	1.16	1.59

Table 5.4: The searched power levels for generating 4-PAM symbols and the corresponding applied voltages used in the completed 4-PAM test.

The searched power levels shown in the second row of table 5.4 were then used for a completed 4-PAM test. In the completed 4-PAM test, the optical power levels for generating the corresponding symbol levels are controlled by the two parameters, the applied voltages of the transmitter and the optics after the light source. For the 2 Mbps 4-PAM test, three ND filters were used to efficiently attenuate the emitted light from the RCLED in order to generate the required optical power levels. Using this given transmitter setup, the searched 4-PAM power levels were totally determined by the corresponding voltage levels. The measured voltage levels are shown in the third row of table 5.4. Based on the searched voltages, using the same transmitter setup, a completed 4-PAM test was performed.

The detailed experimental setup for the completed 4-PAM test is described as follows. At the transmitter, the PRBS signal was generated and modulated to a digital 4-PAM signal by using a MATLAB script running on a PC. The output data from the PC was sent to an Agilent 81150A arbitrary waveform generator (AWG)

to convert the modulated digital signal to the corresponding voltages to drive the transmitter RC650. Three ND filters were placed after the RC650 to attenuate the emitted light. To further attenuate the ambient light generated by the laboratory equipments, a 650 nm band-pass optical filter with a 40nm bandwidth was placed over the MPPC module. A high-resolution oscilloscope, LeCroy HDO6014-MS, captured the output signal of the MPPC module. The received data was processed offline. After synchronisation, the summation method was used to count the number of detected photons within each symbol period. These photon counts were then converted to the corresponding 4-PAM symbols using the optimum decision threshold. Then each decoded 4-PAM symbols were converted to the binary bits according to the Gray code. Comparing with the originally transmitted bits, the BER was calculated. Figure 5.8 shows the histogram of the three signal levels of 4-PAM. Results in table 5.5 show that, although photons are being counted, the measured symbol levels are not those calculated assuming Poisson statistics. In fact, the highest symbol level is 17% higher than the estimated level.

Level	1	2	3	Photons per bit
Measured photons per symbol obtained by evenly distributing errors between symbols	10.9	42.6	102	19.4
Predicted photons per symbol obtained (Ideal Poisson)	10.8	39.7	86.8	17.2
Ratio between measured value and predicted value	1	1.07	1.17	1.13

Table 5.5: A comparison between the predicted number of detected photons per symbol needed to achieve the target BER of 10^{-3} and experimental results with 0.2 counts per symbol due to dark counts.

Efficient 4-PAM power level estimation relies upon detailed knowledge of the noise associated with varying levels of optical power. The distributions of photon counts within 1 μs (the symbol duration of 2 Mbps 4-PAM) have therefore been measured

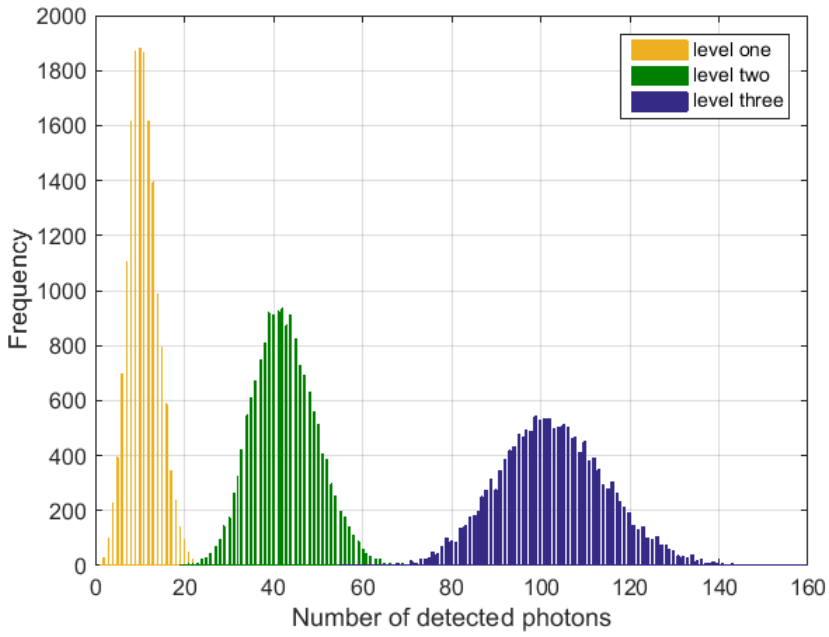


Figure 5.8: The histograms of measured counts per symbol for the 3 signal symbol levels of 4-PAM when a BER of 10^{-3} is achieved in the dark with the data being Gray coded.

at 10 different light levels from 0.05 mW/m^2 to 0.4 mW/m^2. Figure 5.9 shows the distribution of the detected photon counts at 0.4 mW/m^2. It was anticipated that this data would be consistent with either Poisson or Gaussian distribution. However, the typical data in figure 5.9 shows that these two distributions were not sufficiently accurate. A curve-fitting tool in MATLAB was therefore used to simultaneously fit each side of the error distributions from the 10 light levels separately based on the modified Gaussian distribution and this process resulted in the error functions

$$Pe(level-1|level,\ x) = \frac{1}{2}erfc\left(\frac{x-0.95\mu}{0.75\sigma\sqrt{2}}\right) \tag{5.9}$$

$$Pe\left(level+1|level,x\right) = \frac{1}{2}erfc\left(\frac{0.925\mu-x}{1.25\sigma\sqrt{2}}\right) \tag{5.10}$$

where x is the threshold, μ is mean of the photon counts distribution and σ is the

standard deviation of the photon counts distribution.

Based on equation (5.9) and equation (5.10), the optimum 4-PAM symbol levels for the tested MPPC module were estimated by evenly distributing errors between neighboring symbols. From the results in table 5.6, it can be seen that the measured symbol levels are within 2% of the levels estimated using the measured statistics. This result demonstrates that the 4-PAM symbol levels estimation method based on equation (5.9) and (5.10) is accurate.

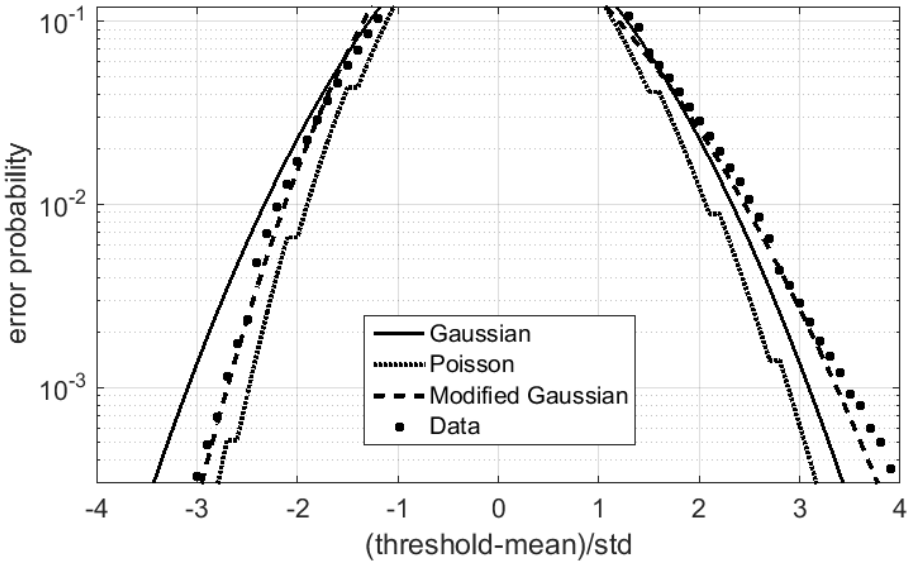


Figure 5.9: A comparison between the number of counts in 1 μs at 0.4 mW/m^2 and three possible mathematical models.

5.4 200 Mbps demonstration using 4-PAM

A system with a 2 Mbps data rate can be used to support low data rate VLC applications [60–62]. However, this low data rate is not particularly useful for meeting the high-speed demand. To further improve the data rate, the tested MPPC module is required to be operated in the analogue mode since the pile-up effect becomes significantly within each symbol period due to the reduction of the symbol time.

Level	1	2	3	Photons per bit
Estimated photons per symbol obtained assuming an even distribution of errors	11	41.9	99.6	19.06
Measured photons per symbol obtained by evenly distributing errors between symbols	10.9	42.6	102	19.44
Ratio between estimated and measured value	0.98	1.02	1.02	1.02

Table 5.6: A comparison between the estimated number of detected photons per symbol needed to achieve the target BER of 10^{-3} and experimental results.

The OOK measurement results in figure 4.11 suggests that, after using DFE, the ISI power penalty is tolerable when the symbol time is set to 10 ns. Therefore, the target 4-PAM data rate for this MPPC module is set to 200 Mbps.

5.4.1 Feasibility check

The first step to do the 200 Mbps 4-PAM test is to check whether the operating range of the MPPC module is sufficient to generate the required 4-PAM symbols at 200 Mbps. Due to the tested MPPC module being AC coupled, the operating range of the MPPC module in analogue mode was measured by calculating the difference between level 1 and level 0 at different optical power levels through the 100 Mbps OOK test which followed the procedure described in section 4.3. In order to avoid the interference from the previous bits, only the samples belonging to the last 0s in 00 transitions and 1s in 01 transitions were used. Based on these selected samples, the difference between level 1 and level 0 was calculated by subtracting the averaged samples of level 1 to the averaged samples of level 0. Figure 5.10 shows the measured differences between level 1 and level 0 against different incident optical powers. This result suggests that the tested MPPC module is almost saturated when the incident

optical power at the active area of MPPC reaches 0.4 μW.

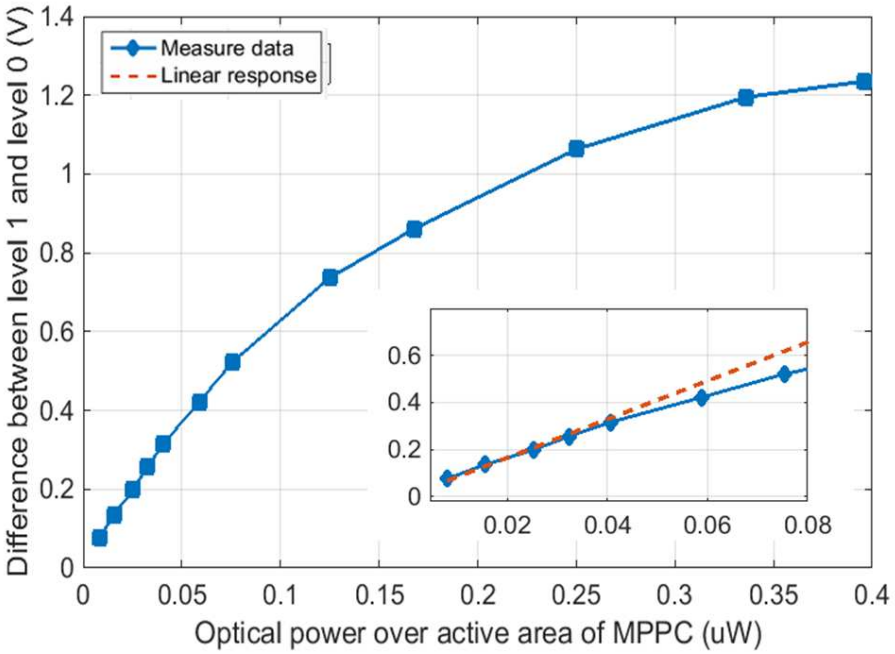


Figure 5.10: Operating range measurement result of the tested MPPC module.

The inset in figure 5.10 shows that the difference between level 1 and level 0 is directly proportional to incident optical power until the optical power reaches 32 nW, where the incident optical power causes the output response drop 2% from the ideal linear response. Within the linear region, the average number of detected photons per bit $\bar{N}$ is also directly proportional to the incident light power which can be calculated by

$$\bar{N} = \frac{PDE \times A \times I \times T}{E_{ph}} \tag{5.11}$$

where A is the total area of the SPAD array, I is the signal intensity, T is the bit time and E_{ph} refers to the single photon energy. Based on equation (5.11) and the measured result in the linear region of figure 5.10, it can be calculated that, in average, 1 detected photon contributes approximately 0.0010 V to the measured difference between level 1 and level 0. Using the ratio 1000 counts/V, the difference

between level 1 and level 0 can be converted to the detected photon counts.

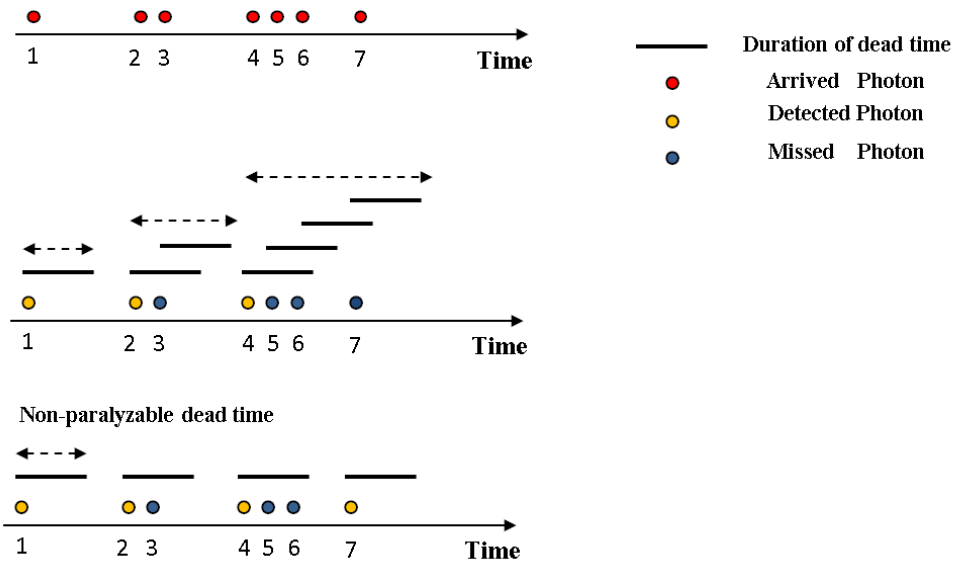


Figure 5.11: The effect of paralyzable dead time and non-paralyzable dead time. Photon arrived within the paralyzable dead time is not only missed but also restarts the dead time. Photons arrived within the non-paralyzable dead time are lost and there is on restarting of the dead time [50].

The nonlinear response of the SPAD array is caused by the effect of dead time [64]. The dead time of the passive quenching SPAD consists of two consecutive dead time periods, the non-paralyzable dead time and the paralyzable dead time [50, 65]. Figure 5.11 illustrates the effect of paralyzable dead time and non-paralyzable dead time. For the non-paralyzable dead time, photons arriving within this period are lost. Suppose the arrived photon rate is λ_{in} and the actual detected count is k within a time T. Since each detected count enables a dead time $\tau_{non-paralyzable}$, the total dead time within the observation time T is $k\tau_{non-paralyzable}$. During the total dead time, $\lambda_{in}k\tau_{non-paralyzable}$ counts are lost. Therefore, the total number of arrived events within time T can be expressed as

$$\lambda_{in}T = k + \lambda_{in}k\tau_{\text{non-paralyzable}} \tag{5.12}$$

Define the detected count rate as

$$\lambda_{out} = \frac{k}{T} \tag{5.13}$$

The detected count rate λ_{out} can be expressed as

$$\lambda_{out} = \frac{\lambda_{in}}{1 + \lambda_{in}\tau_{\text{non-paralyzable}}} \tag{5.14}$$

For a SPAD array consisting of N SPADs, within the observation time T, the total number of detected photon counts N_{out_total} can be expressed as

$$N_{out_total} = NT\lambda_{out} = \frac{NT\lambda_{in}}{1 + \lambda_{in}\tau_{\text{non-paralyzable}}} \tag{5.15}$$

Assume,

$$\alpha = \frac{A_{SPAD}\eta}{E_p} \tag{5.16}$$

$$\lambda_{in} = \frac{LA_{SPAD}\eta}{E_p} = \alpha L \tag{5.17}$$

$$N_{out_total} = \frac{NTL\alpha}{1 + \alpha L\tau_{\text{non-paralyzable}}} \tag{5.18}$$

It can be seen that equation (5.18) is the same as equation (3.13) when λ_{in} in equation (5.18) takes into account the existence of dark counts.

For the paralyzable dead time, a photon within this period will not only be missing but also extend the dead time. The key observation with a paralyzable system is that, only those counts which arrive at time intervals larger than the dead time $\tau_{paralyzable}$ can be counted [66]. The distribution of time intervals with an incident rate follows the exponential distribution. Therefore, the probability of the time intervals between

two detected events larger than $\tau_{paralyzable}$ can be expressed as

$$P\left(t > \tau_{paralyzable}\right) = 1 - \left(1 - e^{\left(-\lambda_{in}\tau_{paralyzable}\right)}\right) = e^{-\lambda_{in}\tau_{paralyzable}} \tag{5.19}$$

Based on equation (5.19), for an array of N SPADs, within the observation time T, the total number of detected photon counts N_{out_total} can be expressed as

$$N_{out_total} = NT\lambda_{in}e^{-\lambda_{in}\tau_{paralyzable}} \tag{5.20}$$

When λ_{in} is low enough, the paralyzable dead time is rarely to be extended and hence $P(t > \tau_{paralyzable})$ is close 1. Based on equation (5.20), it could be calculated that, $N_{out_total} = NT\lambda_{in}$, which is the same as the result calculated by equation (5.15) at low λ_{in}. This means that the paralyzable dead time can be regarded as non-paralyzable dead time at low λ_{in}. When λ_{in} is high enough, the time interval between two adjacent counts will be significantly reduced and hence $P(t > \tau_{paralyzable})$ becomes very small. In this scenario, the two models behave different. For non-paralysable dead time system, according to equation (5.15) λ_{out_total} saturates at $\frac{N\times T}{\tau_{non-paralyzable}}$. For paralysable dead time system, N_{out_total} significantly drops due to $P(t > \tau)$ becomes very small.

For the passive quenching SPAD, non-paralyzable dead time and paralyzable dead time are acted in series [65]. Combine equation (5.15) and (5.20), a hybrid dead time model for passive quenching SPAD was proposed by [67] which is given below

$$\lambda_{out} = \frac{\lambda_{in}e^{-\lambda_{in}\tau_{\text{paralyzable}}}}{1 + \lambda_{in}\tau_{\text{non-paralyzable}}} \tag{5.21}$$

For a SPAD array consisting of N SPADs, within the observation time T, the total detected counts can be expressed as

$$N_{out_total} = \frac{NT\lambda_{in}e^{-\lambda_{in}\tau_{\text{paralyzable}}}}{1+\lambda_{in}\tau_{\text{non-paralyzable}}} \tag{5.22}$$

The total dead time τ_{total} is a sum of the paralyzable and non-paralyzable dead time. If convenient, a parameter β can be added to equation (5.22), which is expressed as

$$N_{out_total} = \frac{NT\lambda_{in}e^{-\lambda_{in}\beta\tau_{\text{total}}}}{1+\lambda_{in}\left(1-\beta\right)\tau_{\text{total}}} \tag{5.23}$$

For MPPC, the manufacturer Hamamatsu also proposed a model, which is expressed as [55]

$$N_{out_total} = N_{total}\left\{1-\exp\left(\frac{-N_{photon}PDE}{N_{total}}\right)\right\} \tag{5.24}$$

where N_{total} is the total number of SPADs within the SPAD array and N_{photon} is the number of incident photons.

Results in figure 5.12 show the accuracies of using the different dead time models to fit the tested MPPC module's nonlinear response. The manufacturer only provides the information of the pulse time rather than the dead time of MPPC module C11209-110. Empirically, the dead time of a SPAD array is approximately equal to the pulse time of the SPAD array when there is no pulse shaping applied. From the data sheet [53], it can be seen that the pulse time and hence the dead time of the S12571-010C is $\sim$ 30 ns. In the MPPC module C11209-110, a band-pass high-speed amplifier effectively reduces the pulse time of S12571-010C from $\sim$ 30 ns to $\sim$ 10 ns. Since the pulse shaping technique may also reduce the dead time of the SPAD array, it was first assumed that the dead time of the MPPC module equals the pulse time of the MPPC module(10 ns). In figure 5.12, the red curve is calculated using the equation (5.24), the Hamamatsu model. The yellow curve is calculated based on equation (5.15), the non-paralyzable dead time model. The green curve is based on

equation (5.20), the paralyzable dead time model. The blue curve is calculated using the equation (5.23), the hybrid dead time model. The result shows that the hybrid model with the searched optimum $\beta = 0.7$ gives the closest approximation to the measured data, but it is still not accurate enough to predict the nonlinear behaviour of this MPPC module. This result indicates that the dead time of this MPPC module does not equal the pulse time of the MPPC module.

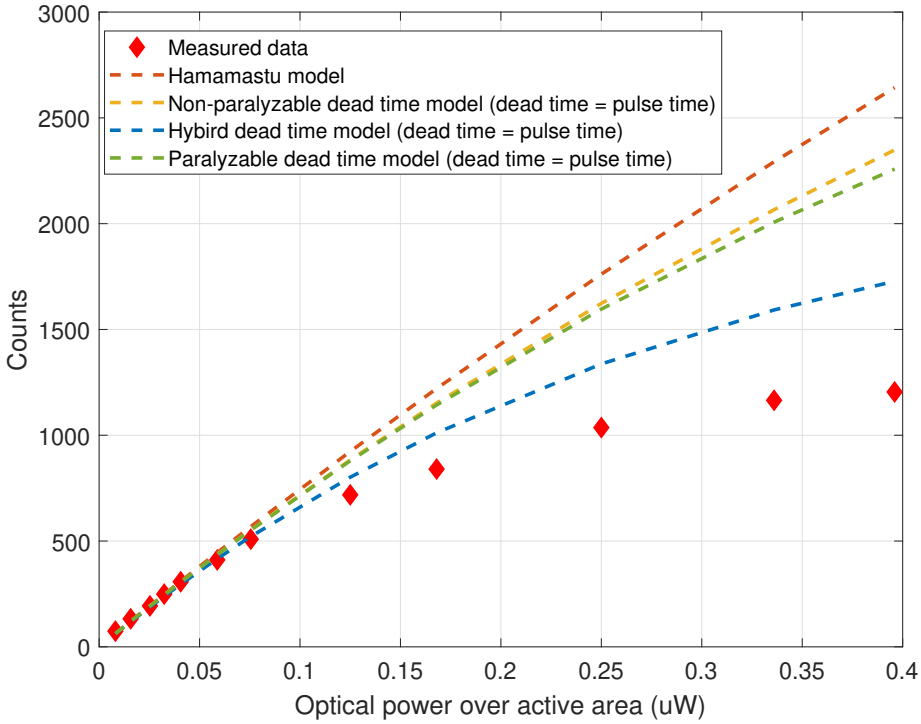


Figure 5.12: The nonlinear response of the tested MPPC module with models fit assuming dead time equals to the pulse time of the C11209-110 module (10 ns). The red spots are calculated using the ratio 1000 counts/V and data in figure 5.10

To get a better fitting result, a dead time correction factor ρ has been used in the calculations. The curves in figure 5.13 show the optimum fitting results when the dead time equals the 10 ns pulse time multiplying with different optimum correction factors ρ. It can be seen that the Hamamatsu model fits the measured data when ρ equals 7 which suggests that the dead time of the MPPC module is 70 ns. For the non-paralyzable dead time model, it fits the measured data when ρ equals 4 which

indicates the dead time of the MPPC module is 45 ns. For the hybrid dead time model, it fits the measured data when ρ equals 3.2, β =0.7 which indicates that the total dead time of the MPPC module is 32 ns and the non-paralyzable dead time equals 10 ns. For the paralyzable dead time model, it fits the measured data when ρ equals 3.05 which indicates that the dead time of the MPPC module is 30.5 ns. With the pulse shaping technique, the dead time has to be less than or equal to the dead time of S12571-010C. Comparing the fitted dead times with the dead time of the S12571-010C ($\sim$ 30 ns), this result suggests that both the hybrid dead time model and the paralyzable dead time model are sensible to be used to estimate the measured output response of S12571-010C. This fitting result is comparable to the results in [65]. Moreover, the best fitted dead times are quite close to the dead time of inner the MPPC S12571-010C, which suggests that the pulse shaping technique does not affect the dead time of the SPAD array.

When the SPAD array enters the saturation region, the impact of paralyzable dead time is getting significant and hence the effective dead time is getting increased. As a result, there is a smaller number of photons that can be detected, after the SPAD array enters the saturation region. When the incident light intensity is higher than the saturation condition, the difference between the paralyzable dead time model and hybrid dead time model becomes distinguishable which is shown in figure 5.14. The measurement result in [51, 65] suggests that the paralyzable dead time model becomes not reliable after the SPADs enter the saturation region. Therefore, the hybrid dead time model should be used to estimate a given SPAD array's operating range. However, the VLC application only interests the region before saturation. For simplicity, the hybrid dead time model can be replaced with the paralyzable dead time model in the VLC application.

For the estimation method based on equation (5.9) and equation (5.10) to be valid requires that there is no ISI within the system since these two equations do

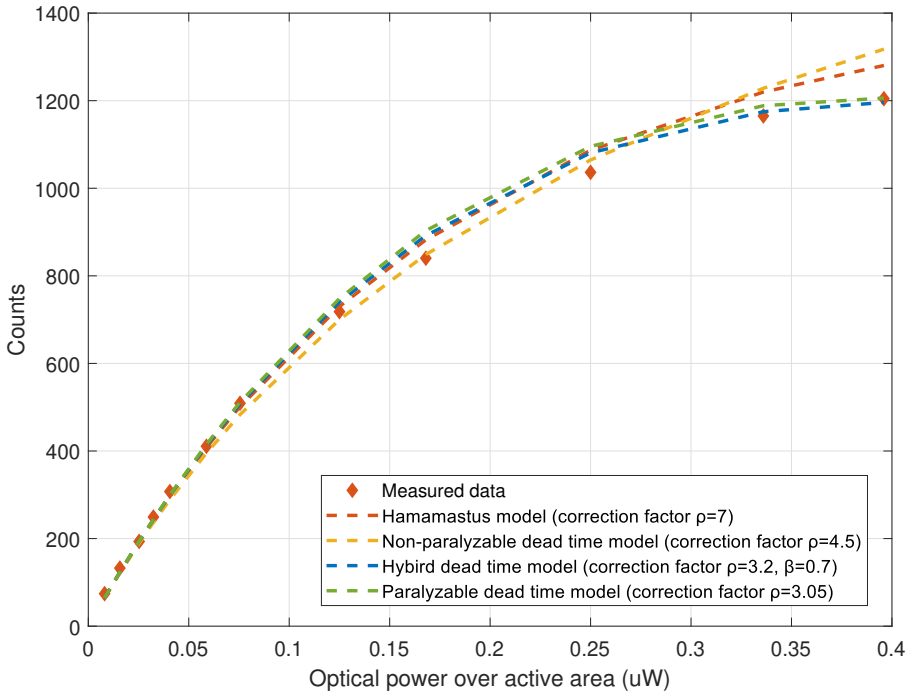


Figure 5.13: The measured nonlinear response of the tested MPPC module with different model fit.

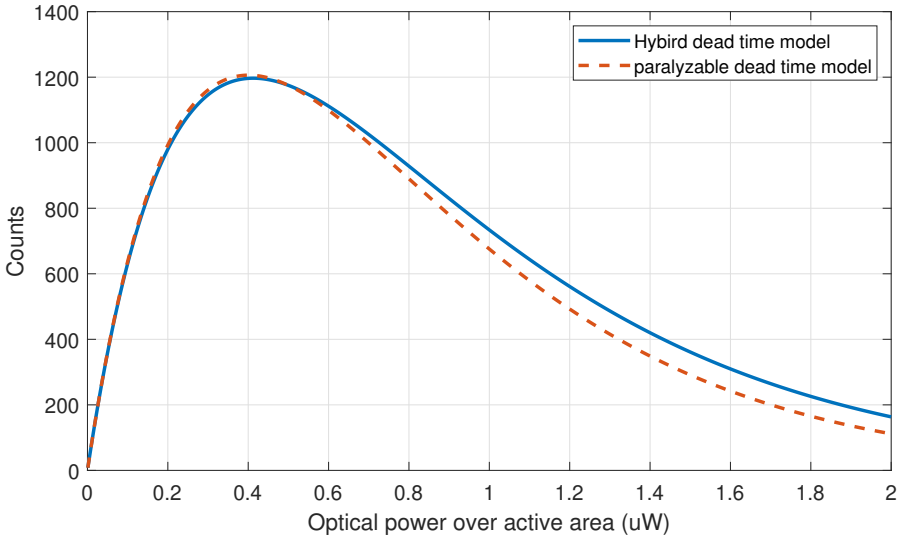


Figure 5.14: Comparision between the hybrid dead time model and the paralyzable dead time model.

not take into account the impact of ISI. Unfortunately, there is ISI in the 200 Mbps 4-PAM test. Figure 5.15 shows the measured distributions of received symbol 1 from

a completed 4-PAM test at 200 Mbps before DFE. There are 4 peaks in the figure. The lowest peak refers to the true PDF of received symbol 1, and the rest of the three peaks are caused by the ISI from the transitions of level 1 to level 1, level 2 to level 1 and level 3 to level 1. This result shows that the ISI at a given 4-PAM symbol level does not only come from its adjacent levels but also the level that it is not close to. As a result, the 4-PAM levels cannot be searched by three individual OOK tests.

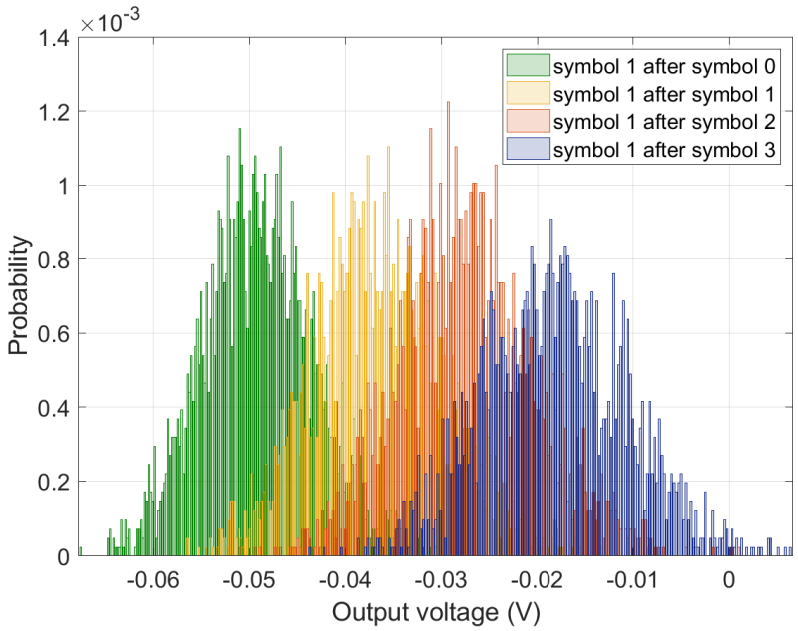


Figure 5.15: The distributions of received 4-PAM symbol 1 after different received 4-PAM symbols measured at a 200 Mbps 4-PAM link in the dark before equalisation.

The ISI power penalty required to compensate ISI within the system using DFE was approximately simulated based on the block diagram shown in figure 5.16. In the simulation, the received signal $y(t)$ is expressed as

$$y\left(t\right) = h\left(t\right) * x\left(t\right) + n\left(t\right) \tag{5.25}$$

where $*$ is the convolution operator, $x(t)$ is the transmitted 4-PAM symbol, $h(t)$ is the overall channel response and $n(t)$ is the noise within the system. In this simulation, the electrical SNR, $SNR_{electrical}$, required at different channel bandwidth to achieve

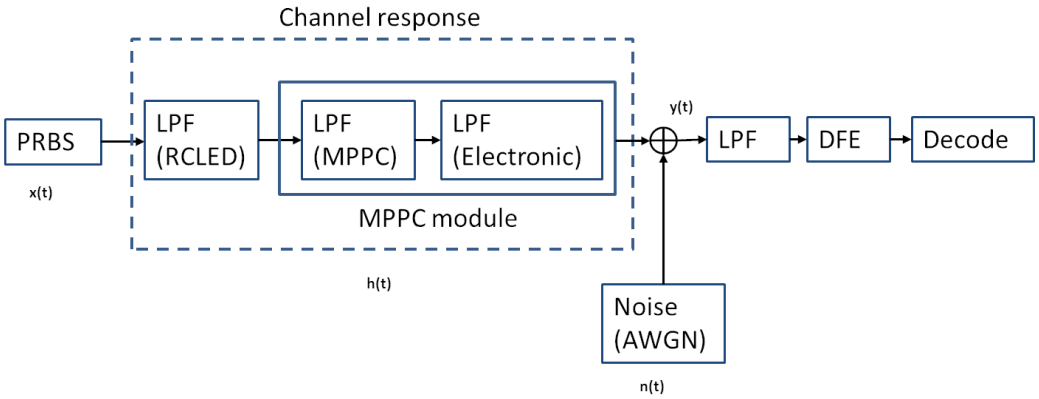


Figure 5.16: Block diagram of the tested MPPC module based 4-PAM system used for Monte Carlo simulation.

a BER of 10^{-3} are searched. For simplicity, in the simulation, the signal levels were fixed and hence the signal power was fixed. It was presumed that $n(t)$ was AWGN noise. When the ISI within the system gets significant, the eye diagram gets closed, and hence less noise power within the system can be tolerated to obtain the target BER. This is equivalent to an increment in the required $SNR_{electrical}$ (electrical SNR penalty). In this approximate estimation, it was presumed that the electrical SNR penalty equals the signal power penalty. The reason is given below. The relationship between the $SNR_{electrical}$, and the optical SNR, $SNR_{optical}$, is given by [68]

$$SNR_{optical} = \sqrt{SNR_{electrical}} \tag{5.26}$$

Therefore, the optical SNR penalty is a square root of the electrical SNR penalty. At the 10 ns symbol time, there are 0.002 background counts per symbol detected by the MPPC module under the dark condition. Even when there is no ISI, the minimum number of signal photons per symbol required to get the target BER 10^{-3} by the MPPC module is 116 which is 5.8×10^4 times higher than the background photons. Since the background counts can be ignored, based on equation (4.6), the optical SNR can be calculated as

$$SNR_{optical} = \sqrt{N_s} \tag{5.27}$$

Consequently, in the dark, the power penalty equal the electrical SNR penalty is a sensible choice. When the MPPC module is operated in the 500 lux ambient light condition, at the same symbol rate, there are 39 background counts per symbol detected. It is calculated that, assuming no ISI, a minimum of 353 signal counts per symbol are required to get the target BER, which is 9 times higher than the detected background counts. The optical SNR calculated without considering the background counts is 5% higher than the optical SNR calculated with the background counts. Consequently, it has to be admitted that letting the power penalty equal the electrical SNR penalty will introduce a tolerable error.

In the simulation, the overall channel response $h(t)$ is calculated as

$$h\left(t\right) = \ h_{Tx}\left(t\right) * h_{SPADs}\left(t\right) * h_{electronic}\left(t\right) \tag{5.28}$$

where $h_{Tx}(t)$ refers to the channel response of the RCLED, $h_{SPADs}(t)$ refers to the channel response of the S12571-010C within the tested MPPC module and $h_{electronic}(t)$ refers to the channel response of the high-speed amplifier within the tested MPPC module. In this approximate estimation, all these three responses are modelled by the first order low pass filter $h_{LPF}(t)$ which has an exponential response as follows

$$h_{LPF}\left(t\right) = \frac{1}{T_C} e^{-\frac{t}{T_C}} \tag{5.29}$$

where T_C is calculated by

$$T_C = \frac{1}{2 \times \pi \times \Delta f_D} \tag{5.30}$$

Term Δf_D refers to the bandwidth of the related device. According to the [53], the falling time of the S12571-010C is approximately 30 ns which indicates that the

bandwidth of the S12571-010C is 13 MHz. For the high-speed amplifier, it has a low cut off frequency of 10 kHz and high cut off frequency of 40 MHz. Since the 10 kHz lower stop band is less than 0.03% of the passband, it was presumed that this high-speed amplifier is a low pass filter with a cut off frequency of 40 MHz.

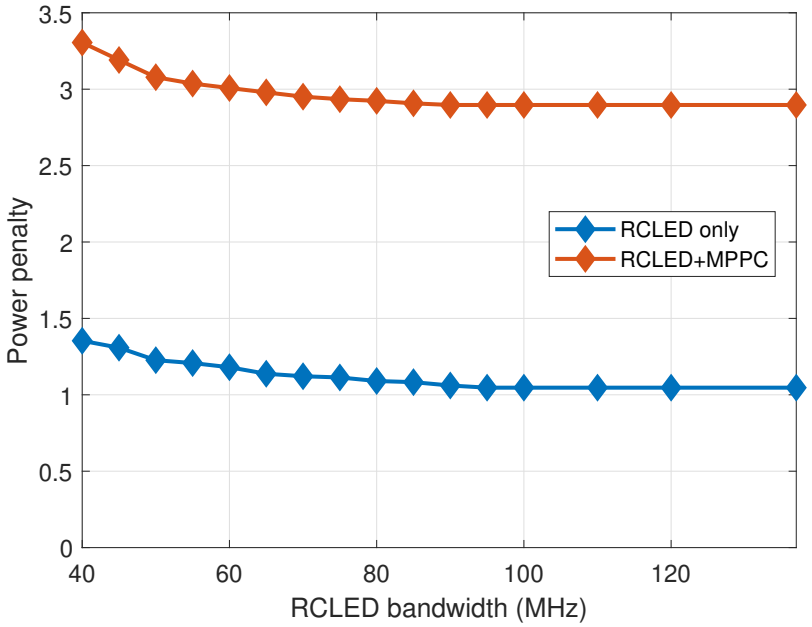


Figure 5.17: The ISI Power Penalty required at different RCLED bandwidth using 4-PAM at a data rate of 200 Mbps.

The modulation bandwidth of the RCLED is determined by the effective DC bias voltage [69]. In 4-PAM, the effective DC bias voltage changes with different symbol transitions. As a result, the modulation bandwidth of the RCLED changes at different symbol transitions. The measured bandwidth of the tested RCLED is in range of 40 MHz to 137 MHz. Therefore, in the worst scenario, the bandwidths of the RCLED within all the 4-PAM transitions are 40 MHz. At the best scenario, the bandwidths of the RCLED within all the 4-PAM transitions are 137 MHz. Figure 5.17 shows the ISI Power Penalty required to compensate ISI achieve a target BER of 10^{-3} at different RCLED bandwidths using 4-PAM with a data rate of 200 Mbps when DFE has been applied. The blue curve shows the estimated ISI penalty only considering

the RCLED's response and the red curves shows the estimated ISI power penalty not only considering the RCLED but also the tested MPPC module. The gap between the two curves indicates that the ISI within this system is dominated by the MPPC module. Moreover, the approximate estimation results shown in blue curve suggests that that the required ISI power penalty for this system to maintain the target BER at 200 Mbps is in a range of 2.8 to 3.3.

At the 10 ns symbol time, there are 39 background counts per symbol detected by the tested MPPC module at the 500 lux ambient light condition. According to the model, equations (5.9) to (5.10), and error evenly distributed strategy, combining the worst power penalty 3.3, approximately 765 SPADs are required to generate the highest 4-PAM level at the 500 lux ambient light environment. Compared to the measured operating range ($\sim$ 1200), this MPPC module is capable of implementing 4-PAM at 200 Mbps in the normal ambient light condition.

5.4.2 Method to search 4-PAM symbol level

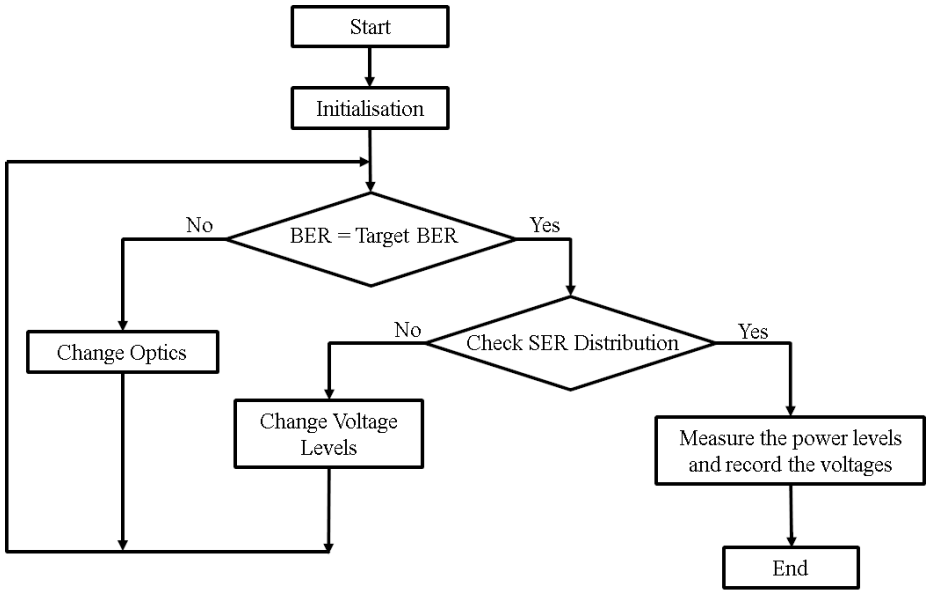


Figure 5.18: Method to search the 4-PAM symbol level.

The appropriate power levels to generate 4-PAM symbols are required to be

searched in a completed 4-PAM test. As discussed in section 5.3, the power levels for creating the corresponding 4-PAM symbol levels are determined by the applied voltages of the RCLED and optics after the RCLED. Compared to the 2 Mbps 4-PAM test, more optical power is required by the 200 Mbps test. Therefore, the three ND filters used before were replaced with a collimating lens. The transmitted power can be changed by changing the beam pattern size by adjusting the distance between the lens and the RCLED. The method for searching the optimum 4-PAM power levels by changing the optics and applied voltages is shown in figure 5.15. In the first step, to fully turn off the RCLED for sending symbol 0, the applied voltage for symbol 0 is fixed to 0.75V. To fully use the operating range and the bandwidth of the tested RCLED, the applied voltage for symbol 3 is fixed to 1.8V. After that, the other two applied voltages for symbol 1 and symbol 2 between symbol 0 and symbol 3 and the distance between lens and RCLED are set according to the estimated power level using the model, equation (5.9) to (5.10). The second step is to check whether the measured BER equals the target BER. If the measured BER does not equal the target BER, the beam pattern size is changed by adjusting the distance between the lens and the RCLED and the second step repeated to recheck the BER. If the measured BER equals the target BER, then the SERs distribution is checked. If the SERs are evenly distributed, then the optical powers for each symbol level are measured and the applied voltage levels recorded. If not, the applied voltages for symbol 1 and symbol 2 are changed and the second step repeated.

5.4.3 Experimental results

Using the searched power levels and voltages, 200 Mbps data rate with a BER of 10^{-3} has been achieved with a sensitivity of approximately 43 photons per bit in the dark and 177 photons per bit in the 500 lux ambient light. Figure 5.19 shows the 200 Mbps eye diagram measured in the dark before equalisation. As expected, the eye is

almost closed which indicates that the ISI within this tested system is significant.

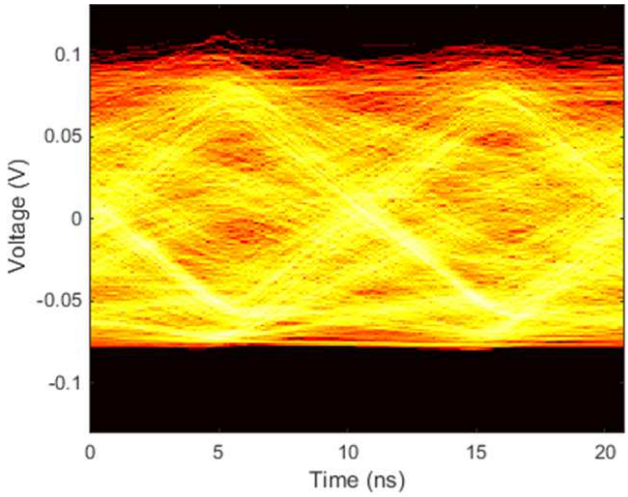


Figure 5.19: Eye diagram of 200 Mbps 4-PAM link operated in the dark with a BER of 10^{-3} before equalisation.

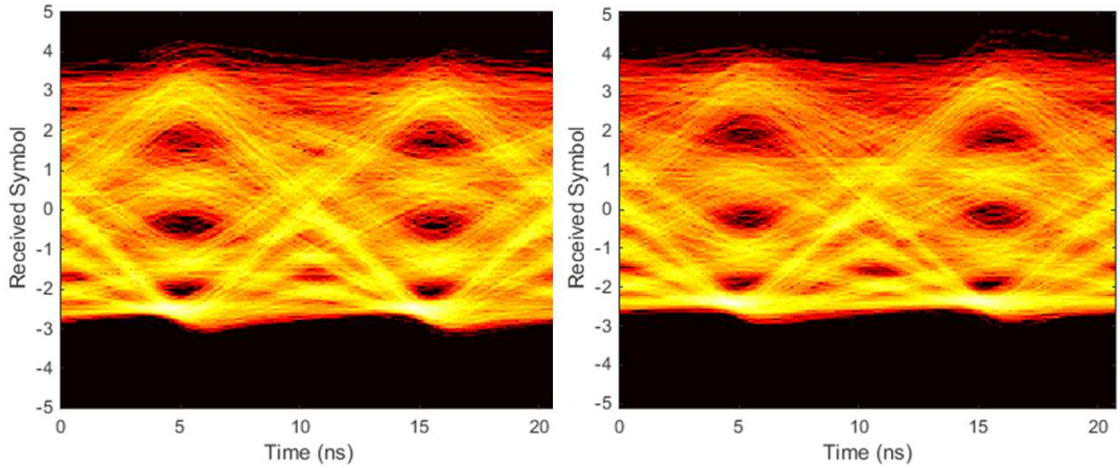


Figure 5.20: Eye diagram of 200 Mbps 4-PAM link operated in the dark and in the 500 lux ambient light with a BER of 10^{-3} after equalisation.

To achieve the target BER, the impact of the ISI was mitigated using a DFE equaliser at a cost of the sensitivity. The eye diagrams of the equalised 4-PAM symbol measured in the dark and 500 lux are shown in figure 5.20. These two measurements achieve the same target BER using the same SERs distribution criteria. Therefore, as expected, the two equalised eye diagrams are very similar. The searched power

	Estimated value (W/m^2)	Mesured value (W/m^2)	Ratio
Level 1	0.0008	0.0027	3.34
Level 2	0.0037	0.0124	3.35
Level 3	0.0089	0.028	3.15
Total	0.0134	0.0431	3.22

Table 5.7: Comparisons between measured 4-PAM symbol levels with estimated values in the dark.

	Estimated value (W/m^2)	Mesured value (W/m^2)	Ratio
Level 1	0.0108	0.037	3.43
Level 2	0.0188	0.062	3.30
Level 3	0.0292	0.08	3.09
Total	0.059	0.189	3.20

Table 5.8: Comparisons between measured 4-PAM symbol levels with estimated values at 500 lux.

levels for generating 4-PAM symbols listed in the table 5.7 and 5.8. It can be seen that the average power penalty needed to overcome ISI in the dark was 3.34 and the equivalent result with 500 lux of ambient light was 3.2. Both of these values are within the estimated power penalties in figure 5.17. To the authors best knowledge, so far, this is the fastest SPAD-receiver-based 4-PAM VLC system demonstrated in the dark and in the 500 lux environmental light. These experimental results demonstrate the potential for implementing high-speed VLC system using a SPAD-based receiver combined with 4-PAM.

5.5 Summary

In this chapter, the efficient way of using the SPAD-based receiver to support 4-PAM is investigated. Using the Poisson model(equation (5.2) and (5.4)), the optimum strategy to set the 4-PAM symbol levels has been investigated. Simulation results suggest that setting the 4-PAM symbol levels based on errors evenly distributed between the pairs of symbol levels is the optimum strategy in practical 4-PAM design. Using this optimum strategy, the impact of background noise and the difference between using Gaussian model and Poisson model to estimate 4-PAM symbol levels have been analysed. Results suggest that the Gaussian model is a good approximation to the Poisson model for 4-PAM when the background counts per symbol is higher than 2 counts per symbol.

The accuracy of the Poisson model (equation (5.2) and equation (5.4)) has then been experimentally assessed at a data rate of 2Mbps. Measurement result shows that the required power levels is 17% higher than the estimated power levels based on this numerical model. To further improve the estimation accuracy, a more accurate model based on equation (5.9) and (5.10) has been investigated. Using these two equations, the estimated power levels are within 2% different from the measured power levels.

The 2 Mbps data rate is suitable for the low speed VLC application but not practically useful for meeting the demand of high speed VLC. The OOK measurement result in figure 4.11 suggests that, after using DFE, the ISI power penalty is tolerable when the symbol time is 10 ns. Therefore, a 200 Mbps 4-PAM link has been tested. The operating range of the tested MPPC module is measured first. Four empirical dead time models have been tested to fit the nonlinear response of the tested MPPC module. Among the four models, the hybrid dead time model and the paralyzable dead time model give the best fitting result at the non-saturate region of the tested MPPC module. Since only the non-saturated region is interested in VLC application, this result suggests that the paralyzable dead time model can be used to replace the

hybrid dead time model for estimating the operating range of the passive quenched SPAD array. The power penalty required to compensate the ISI within 4-PAM symbol using DFE has been estimated by assuming the frequency response of the SPAD array is a first order roll-off low-pass filter. Using the estimated power penalty and the estimated number of photons required to generate the highest 4-PAM level, it is anticipated that the operating range of the tested MPPC module can support the 200 Mbps 4-PAM.

Based on a practical method to search the 4-PAM symbol levels, a completed 4-PAM test has been performed. Despite the significant ISI within the system, based on the searched 4-PAM symbol levels, 200 Mbps data rate has been achieved with a sensitivity of approximately 43 photons per bit in the dark and 177 photons per bit in the normal indoor ambient light condition. Moreover, results suggest that the power penalty required by DFE to compensate ISI can be estimated using a simple method that assumes that the response of the SPAD array can be approximated by a first order roll-off low-pass filter.

Chapter 6

Future Prospects of SPAD-based VLC receiver

6.1 Introduction

The previous chapter demonstrates that a 200 Mbps data rate can be achieved with a convenient SPAD array which has a lower PDE than more recent SPADs. The main results are therefore the understanding of the use of SPADs in the VLC receiver. As a result of the continuing improvements in manufacturing processes, SPADs are now available which have a higher PDE. The APD-based receiver can offer Gbps data rates [10, 11]. To match the APD's performance, in this chapter, the feasibility of using a receiver based on newly released SPAD arrays shown in table 1 in Appendix B to support a data rate of 1 Gbps or even higher, within typical indoor ambient light condition is estimated.

6.2 Estimated background counts from ambient light

To estimate the sensitivity of the newly released SPADs under the 500 lux ambient light environment, it is essential to estimate the background counts generated by the ambient light source. Figure 6.1 shows the density of background photons per second within a 1 mm^2 detector measured from a range of lighting sources [70] at 500 lux condition. This result shows that the receiver will suffer from the minimum number of background photons when the system's wavelength is around 400 nm and the maximum number of background photons when the system's wavelength is around 620 nm. To reduce the impact from the ambient light source, the SPAD-based VLC system is recommended to be operated at around 400 nm. The previous experiment described in section 3.5 measures that the background counts per second were reduced by approximately 6 times when the FOV of the receiver was restricted to 24 degrees. Combining a conventional bandpass filter 400FS40-50, which has a 40 nm bandwidth at the 400 nm central wavelength and a 45% transmission, with the 24-degree FOV, the total ambient light power can be reduced by a factor of 13. After integrating the averaged density from 380 nm to 420 nm and dividing the total power reduction factor 13, the background photons per second reaching a 1 mm^2 detector can be reduced to 1.5×10^9 counts per second.

For a particular SPAD array, the detected background counts per symbol N_b can be calculated using the equation below

$$N_b = \frac{PDE}{FF} \times T \times A \times 1.5 \times 10^9 \tag{6.1}$$

where T is the symbol time T, FF is the fill factor of the SPAD array and A is the active area of the SPAD array in mm^2. Using symbol time, FF, PDE, active area given in table 1 in the Appendix B, the number of detected background photons per

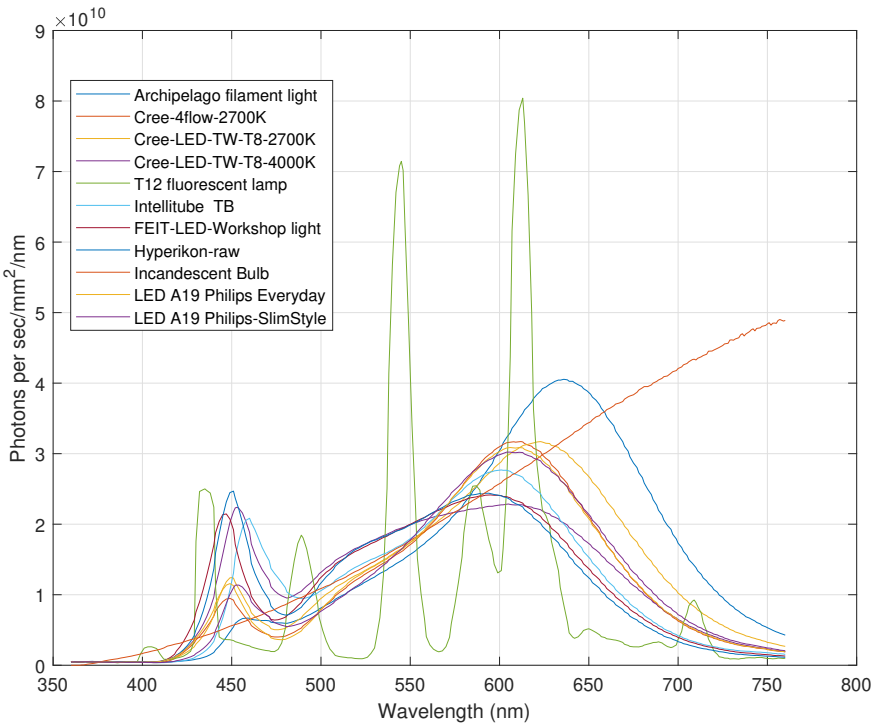


Figure 6.1: The density of background photons per second measured by a 1 mm^2 detector from different lighting sources at 500 lux condition.

symbol for a particular SPAD array at 400 nm wavelength in the 500 lux ambient light condition can be calculated. In addition, the background counts are also generated by the dark counts within the SPADs. From table 1 in Appendix B, it can be found that, in the worst case, the dark counts per second within 1 mm^2 are 7×10^5 counts per second. Therefore, in the worst case, the dark counts per symbol can be calculated as

$$\mathrm{N_{DCR}} = T \times A \times 7 \times 10^5 \tag{6.2}$$

Even with the lowest PDP ($\frac{PDE}{FF}$) in table 1 in Appendix B which is 38%, the number of dark counts is more than 790 times less than the number of background counts generated by ambient light. Therefore, the impact of dark count is negligible compared to the background counts generated by the ambient light even when the background

counts generated by the ambient light are restricted by the optical filter and FOV.

6.3 Impact of dead time and pulse time

To support the Gbps data rate, the symbol time has to be less than or equal to 1 ns when OOK is used. According to the parameters listed in table 1 in Appendix B, the 1 ns symbol time is much less than the dead time and the pulse time. The dead time determines the number of available SPADs within an array and hence the effective PDE of the SPAD array. The effective PDE within a bit period, PDE_{eff}, can be calculated by

$$PDE_{eff} = \frac{N_{out_total}}{N_{incident}} \tag{6.3}$$

where N_{out_total} is the number of photons detected by the SPAD array within a bit period and $N_{incident}$ refers to the number of incident photons within a bit period over the total area of SPAD array. From figure 5.14, it can be seen that the SPAD array cannot detect more photons with the increased optical power when it enters the saturation region, which means that the BER cannot be further improved by increasing the signal power at this point. As a result, for VLC application, only the region before saturation is interesting. Moreover, the result in figure 5.14 also shows that the paralyzable dead time model and the hybrid dead time model are almost the same in the non-saturation region. Therefore, for simplicity, the paralyzable dead time model is used to calculate the effective PDE. According to equation (5.20) and equation (5.11), equation (6.3) can be expressed as

$$PDE_{eff} = PDE_{max}e^{-x} \tag{6.4}$$

where PDE_{max} is the original PDE of the SPAD array given by the manufacture's data sheet, and x refers to the ratio of the dead time to the inter photon time which is expressed as

$$x = \frac{t_{dead}}{t_{interphoton}} = \frac{t_{dead} N_s}{N_{SPADs} T} \tag{6.5}$$

where T is the symbol duration, t_{dead} is the dead time of the SPAD array, N_s is the average number of SPADs fired within a symbol duration in bit one, and N_{SPADs} is the total number of SPADs within a SPAD array. The detailed deviation of equation (6.3) to (6.5) is given by Appendix C. The factor e^{-x} in equation (6.4) determines the PDE reduction. For a given N_s and symbol time T, equation (6.4) and equation (6.5) suggest that the impact of dead time on the PDE reduction, and hence the receiver sensitivity reduction, is determined by the ratio of SPAD array's dead time to the number of SPADs within an array. At a given N_s and symbol time T, the SPAD array with the smaller dead time and a larger number of SPADs will suffer from less PDE reduction.

Another important characteristic of the SPAD arrays is the pulse time which is related to the bandwidth of the SPAD array. For a SPAD array with a pulse time t_{pulse}, the bandwidth of the SPAD array can be calculated as

$$\Delta f_{SPADs} = \frac{1}{2\pi \times \left(\frac{t_{pulse}}{-\ln(1-p)} \right)} \tag{6.6}$$

where p is the falling percentage that is used to define the pulse time by the manufacturer. Different manufacturers select different p values. In this chapter, p is set to 99%. Correspondingly, the pulse time is defined as the duration when the pulse is falling 99%. When the symbol rate is larger than the bandwidth of the SPAD array, additional power is required to compensate for ISI.

Estimates of the increase in power that will be required by the SPAD array with

insufficient bandwidth to support higher symbol rate using OOK and 4-PAM have been obtained using the same time domain Monte Carlo simulation mentioned in section 5.4.1 based on equation (5.29) assuming other components within the system have sufficient bandwidth. In figure 6.2, the spots are the results obtained based on Monte Carlo simulation. The two curves are the fitted curve, and the fitting function is given below.

$$PP = \begin{cases} 1 & r_{sb} \leq 1 \\ a.e^{br_{sb}} + c.e^{dr_{sb}} + k & 1 < r_{sb} < 2 \\ p1.r_{sb} + p2 & r_{sb} \geq 2 \end{cases} \tag{6.7}$$

where r_{sb} refers to the ratio of the symbol rate to the bandwidth. The fitted parameters are given in table 6.1.

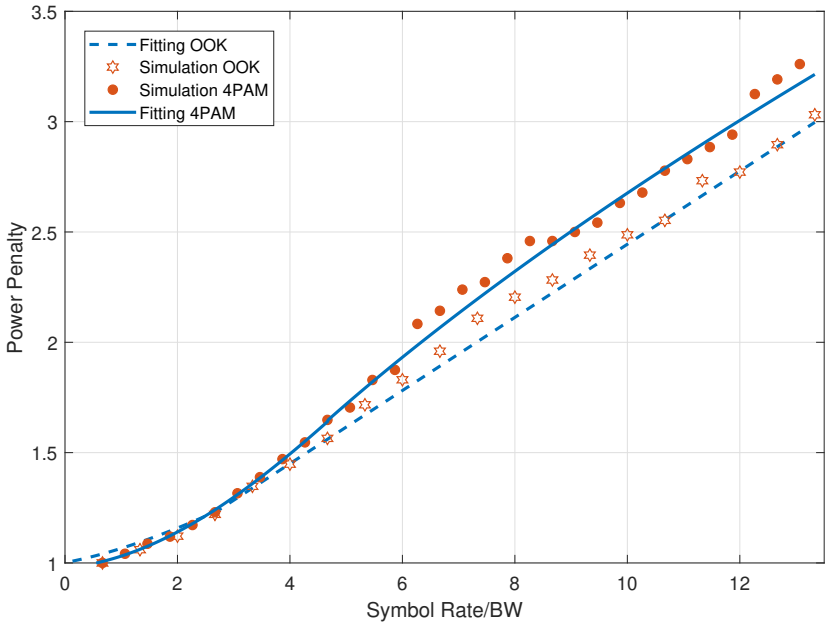


Figure 6.2: The estimated extra power needed to employ DFE when the symbol rate is higher than bandwidth of the SPAD array.

Fitted parameters	4-PAM	OOK
a	0.088	0.07691
b	-1.383	-0.6276
c	0.9122	0.944
d	0.1086	0.1012
k	-0.01	-0.02
p1	0.1902	0.1658
p2	0.7765	0.827

Table 6.1: Fitting parameters used in figure 6.2.

6.4 A general method to estimate the sensitivity of a given SPAD array

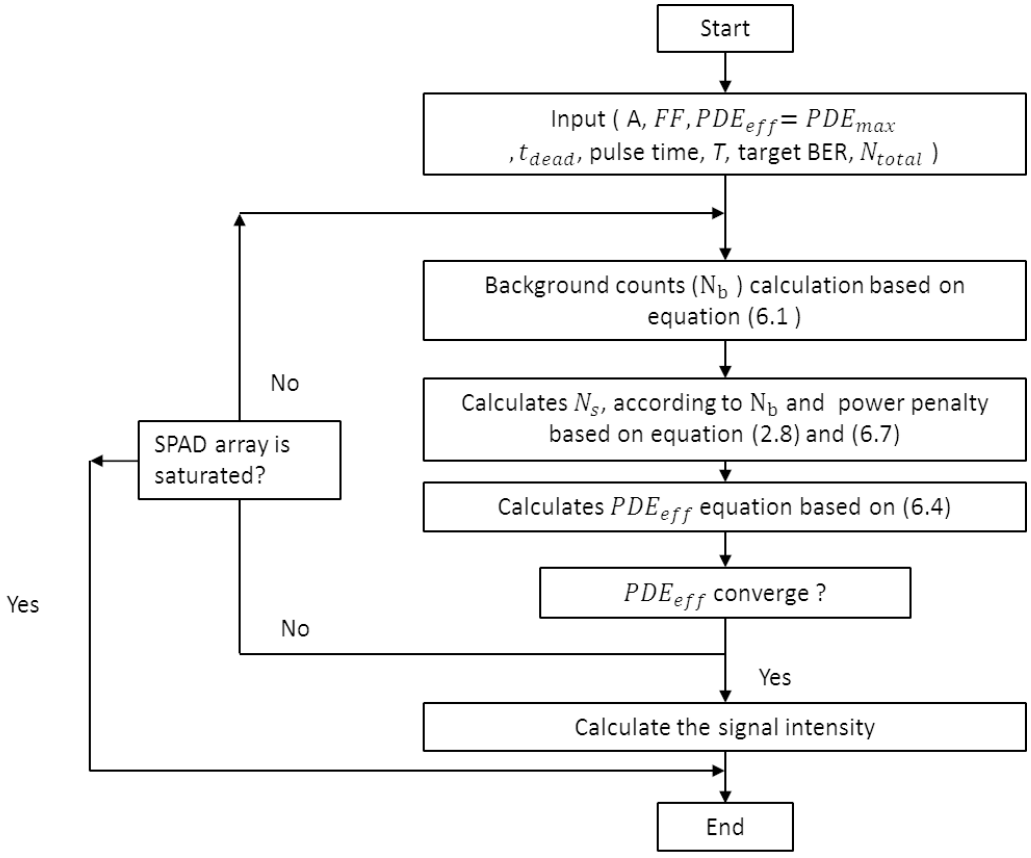


Figure 6.3: A general method to estimate the sensitivity of a given SPAD array.

The method to estimate the signal intensity required by a given SPAD array to achieve the target BER at a given data rate using OOK modulation is shown in

figure 6.3. This method starts with inputting the symbol time T, the target BER, the specification of a given SPADs including its total area, FF, PDE, pulse time, dead time and the total number of SPADs in an array. Then based on equation (6.1) the number of detected background counts per bit are calculated. Using equation (2.8) and detected background counts per bit, the average number of detected signal counts per bit N_{s0} in bit one can be calculated. When the background count per bit is higher than 2, the Gaussian model equation (3.15) can be applied to accelerate the searching process for N_s. Because, based on the Gaussian model, the signal counts can be directly calculated using equation (3.15).

Based on equation (6.7), the power penalty PP required to compensate ISI is calculated. The number of signal photons per bit N_s that are required can then be calculated using

$$N_s = PPN_{s0} \tag{6.8}$$

Afterwards, the effective PDE is calculated according to equation (6.4) and the calculated signal counts per bit N_s. When the effective PDE is changed, the detected background count per bit has to be changed, and hence the signal counts per bit N_s. Therefore, an iteration process is required to calculate the actual effective PDE. From equation (6.1) and (6.4), it can be seen that decreasing the PDE_{eff} will reduce the background counts per bit and hence reduce the N_s. The reduced N_s will increase the PDE_{eff}. Since the signal counts is increased less quickly than the background counts, if the SPAD array is not saturated, the effective PDE can converge to a stable value. When PDE_{eff} becomes stable (PDE_{eff} changed by less than 1% during the iteration), the updated effective PDE, signal counts, symbol time and detector area, are then used to calculate the required signal intensity to achieve a target BER at a given data rate and return the calculated signal intensity. If the SPAD array enters the saturation region (N_s exceed the maximum number of photons can be detected), the target BER can not be achieved by the SPAD array since the SPAD array cannot

detect more photons with higher optical power. In this case, the calculation has to be terminated and return null.

6.5 Estimation results for OOK

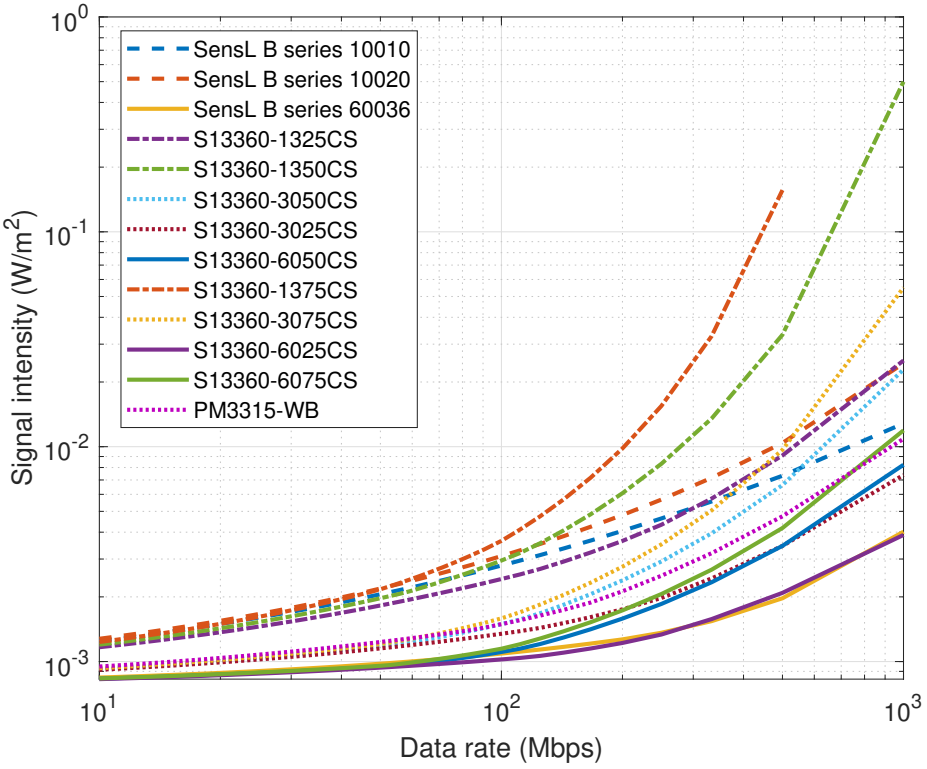


Figure 6.4: Signal intensities required by the SPAD arrays in table 1 in Appendix B to achieve a BER of 10^{-3} in the 500 lux ambient light condition at different data rates.

The estimated signal intensities required by the SPAD arrays listed in the table 1 in Appendix B to achieve a BER of 10^{-3} under the 500 lux ambient light condition at different data rates using OOK are shown in figure 6.4. The solid lines represent the SPAD arrays with 36 mm^2 active area, the dotted lines represent the SPAD arrays with 9 mm^2 active area, and the dash-dotted lines and dashed lines represent the SPAD arrays with approximately 1 mm^2 active area. It can be seen that SPAD

arrays with the 36 mm^2 active area have the highest sensitivity. This result indicates that the active area primarily determines the sensitivity of the SPAD array.

For a given active area, based on equation (2.12) and (6.4), the sensitivity of a SPAD array can be expressed as

$$N_{in} = \frac{N_S}{PDP_{eff}} = \frac{N_S}{PDP_{\max}.e^{-x}} = \frac{PP.N_{s0}}{PDP_{\max}.e^{-\frac{t_{dead}.PP.N_{s0}}{N_{SPADs}.T}}} \tag{6.9}$$

where N_{in} refers to the number of photons per bit required incident the active area of a given SPAD array, PDP_{max} is calculated using PDE and FF provided by the manufacturer's data sheet, PDP_{eff} refers to the effective PDP, and x is the ratio between the dead time and the inter photon time calculated by equation (6.5). Equation (6.9) suggests that the sensitivity of a given SPAD array with the largest active area is determined by the effective PDP and the ISI power penalty. For a given N_S, a higher effective PDP results in a higher sensitivity. When ISI is present, the ISI power penalty reduces the sensitivity since the ISI power penalty not only increases the number of detected photons required but also reduces the effective PDP. The ISI power penalty PP is determined by the pulse time of the SPAD array.

At high data rates, ISI is present, and hence the sensitivity is determined by both the effective PDP and the pulse time. Figure 6.5 shows the sensitivity of SPAD arrays with the 36 mm^2 active area, listed in table 6.2, at different data rates. Since the ISI power penalty depends on the data rate, the effective PDP changes with the data rate. Figure 6.6 shows the effective PDP at different data rates. Results in figure 6.5 and figure 6.6 suggests that the effective PDP becomes less important than the pulse time when the data rate is higher than 200 Mbps. Although SensL B 60036 has a relatively low effective PDP, due to the shortest pulse time, SensL B 60036 is still a good choice at the data rate higher than 200 Mbps.

At the low data rates, when there is no ISI, the SPAD array's sensitivity is only determined by the effective PDP. The effective PDP is determined by the original PDP

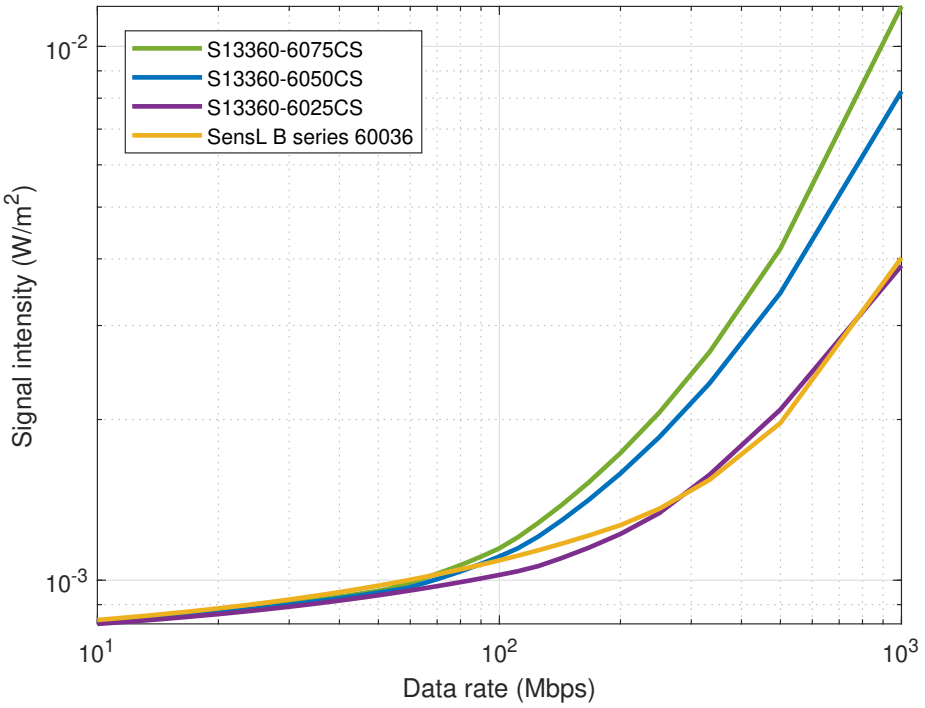


Figure 6.5: Signal intensities required by the SPAD arrays with the 36 mm^2 active area in table 1 in Appendix B to achieve a BER of 10^{-3} in the 500 lux ambient light condition at different data rates.

Serial Number	Dead time (ns)	Number of SPADs	$\frac{t_{dead}}{N_{SPADs}}$	PDE (%)	FF (%)	PDP (%)	Pulse time (ns)
SensL B series 60036	411	18980	0.02165	41	64	64	3.20
S13360 -6075CS	69	6400	0.01078	50	82	61	13.80
S13360 -6050CS	61	14400	0.00426	40	74	54	12.27
S13360 -6025CS	30	57600	0.00052	25	47	53	6.00

Table 6.2: SPAD arrays with 36 mm^2 active area extracted from table 1 in Appendix B

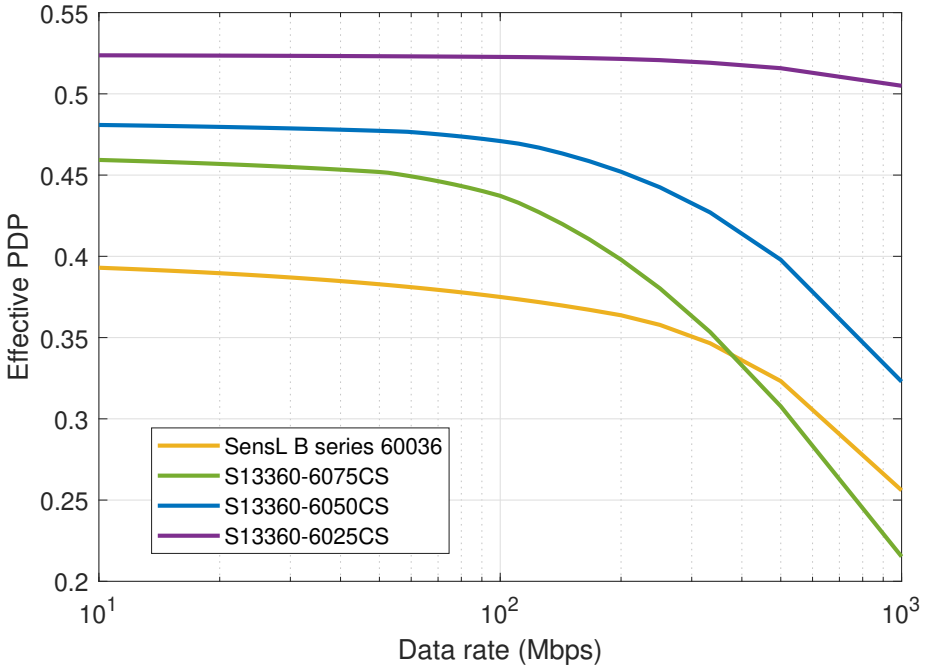


Figure 6.6: Effective PDP of the SPAD arrays with 36 mm^2 active area at different data rates.

and the PDP reduction due to the impact of dead time. As discussed in section 5.4.1, at a high incident photon rate over the total SPAD array, the SPAD array suffers from the impact of dead time. A SPAD array with larger number of SPADs and shorter dead time has more available SPADs to detect the incident photons and hence will be less impacted by the dead time. Therefore, the ratio between the dead time and the number of SPADs, $\frac{t_{dead}}{N_{SPADs}}$, is a critical factor that determines the effective PDP. The smaller this ratio, the less PDP reduction will be. The calculated $\frac{t_{dead}}{N_{SPADs}}$ for those 4 SPAD arrays are listed in table 6.2. Figure 6.7 shows the sensitivities required by the SPAD arrays with an active area of 36 mm^2 below 50 Mbps. The lowest bandwidth of those 4 SPAD arrays is 52 MHz. Therefore, no ISI is present when the data rate is below 50 Mbps. Results in figure 6.7 show that, although SensL B 60036 has the highest original PDP, it is not the optimum choice for low data rate VLC receiver due to its longest dead time significantly increases $\frac{t_{dead}}{N_{SPADs}}$ and hence limits its effective PDP. S13360-6025CS becomes the optimum choice for the low data rate VLC receiver.

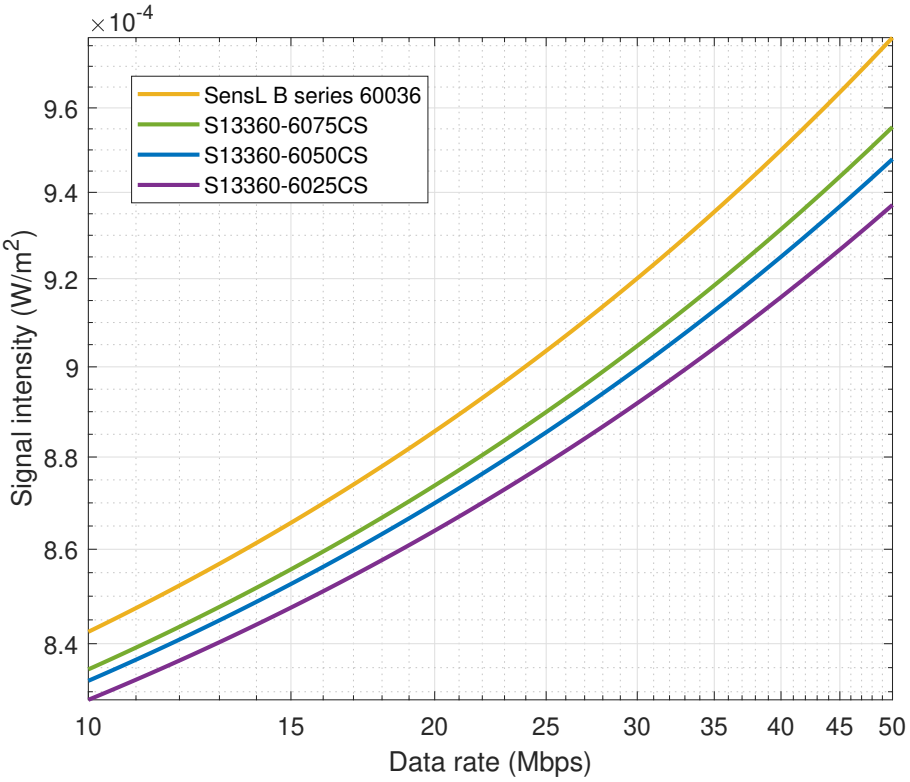


Figure 6.7: Signal intensities required by the SPAD arrays with the 36 mm^2 active area in table 1 in Appendix B to achieve a BER of 10^{-3} in the 500 lux ambient light condition below 50 Mbps.

Although S13360-6025CS has the lowest original PDP, due to it has the shortest dead time and the largest number of SPADs in this array, S13360-6025CS suffers from the smallest PDP reduction which results in the highest effective PDP.

For implementing a high-speed VLC receiver with high sensitivity, the desired SPAD array should have a large active area, short pulse time, high PDP, a large number of SPADs and short dead time. At the moment, the best choice are the S13360-6025CS and the SensL B 60036. Using equation (4.18), even at 1 Gbps data rate, it can be calculated that the Q of S13360-6025CS is approximately 3 times higher than the tested APD, assuming that the tested APD can be made with sufficient bandwidth. Since the sensitivity of SensL B 60036 is almost the same as S13360-6025CS at 1 Gbps, this result indicates that both the S13360-6025CS and SensL B

60036 can be used to create a more sensitive VLC receiver than the conventional APDs.

The estimation above is based on the average background counts generated in the 500 lux lighting condition at a wavelength of 400 nm. However, in the practical, there is a possibility that the SPAD-based receiver can suffer from higher background counts such as being operated in the brighter lighting conditions. The increased background counts may limit the data rate that can be achieved using the S13360-6025CS or the SensL B 60036. Since the dead time of SensL B 60036 is more than 10 times longer than the S13360-6025CS, it is expected that the SensL B 60036 will be more susceptible to the ambient light noise increment.

The solid curves in figure 6.8 represent the S13360-6025CS at higher ambient light conditions and the other three curves represent the SensL B 60036 at higher ambient light conditions. N_b refers to the average background counts generated in the 500 lux lighting condition at a wavelength of 400 nm. This result suggests that more power is required to compensate the increased background counts. However, the required signal intensity increases less quickly than the background counts. Moreover, as expected, the SensL B 60036 is more susceptible to the ambient light change. In fact, this figure shows that the SensL B 60036 cannot get the 1 Gbps data rate when the background counts are 2.5 times higher than the average background counts generated in the 500 lux lighting condition at a wavelength of 400 nm. For the S13360-6025CS, even the background counts are 10 times higher than the average background counts generated by the 500 lux lighting condition at a wavelength of 400 nm, it is still has the capability to support the 1 Gbps data rate. This result suggests that the S13360-6025CS is the optimum choice for implementing reliable high-data rate VLC receiver.

The results in figure 6.8 show that when the background counts is 15 times higher than the averaged background counts generated in the 500 lux ambient light condition

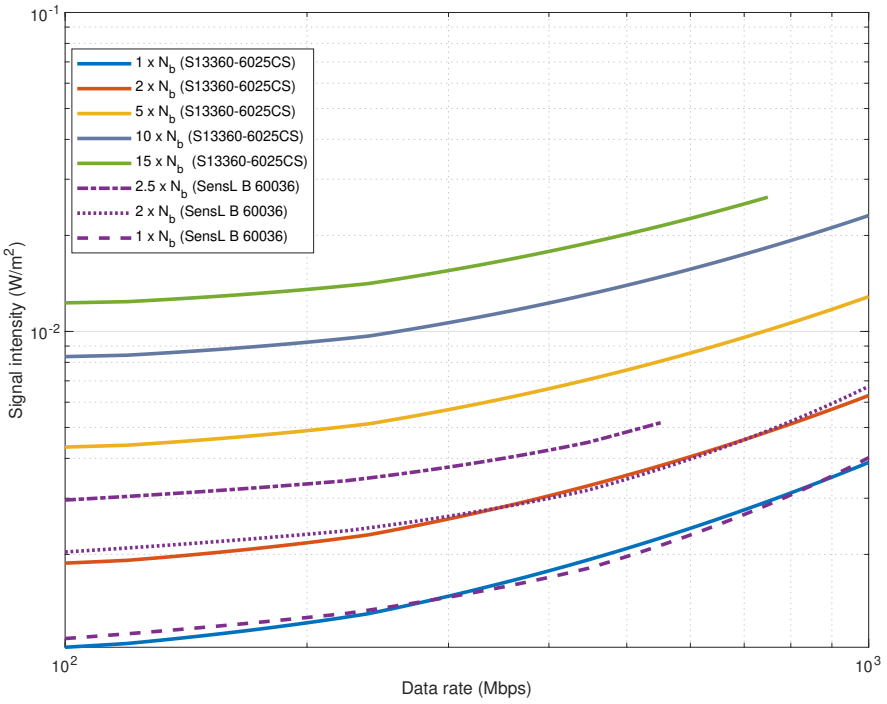


Figure 6.8: Signal intensities required by the S13360-6025CS and SensL B 60036 within higher ambient light conditions to achieve a target BER at different data rates. The symbol N_b in this figure refers to the averaged background counts generated in the 500 lux ambient light condition at a wavelength of 400 nm and the number in the legend refers to N times the averaged background counts generated in the 500 lux ambient light condition at a wavelength of 400 nm.

at a wavelength of 400 nm, the S13360-6025CS based receiver is unable to achieve the 1 Gbps data rate. To determine the highest background condition under which the S13360-6025CS based receiver is capable of supporting the 1 Gbps data rate, figure 6.9 is ploted which shows the data rate can be achieved with the S13360-6025CS based receiver at different background count conditions. The x-axis in figure 6.9 refers to the K times the averaged background counts generated by the 500 lux ambient light condition at a wavelength of 400 nm. This figure shows that the S13360-6025CS based receiver is capable of supporting a data rate of 1 Gbps until the background counts is 11.6 times higher than the background counts generated in the 500 lux typical lighting condition at a wavelength of 400 nm.

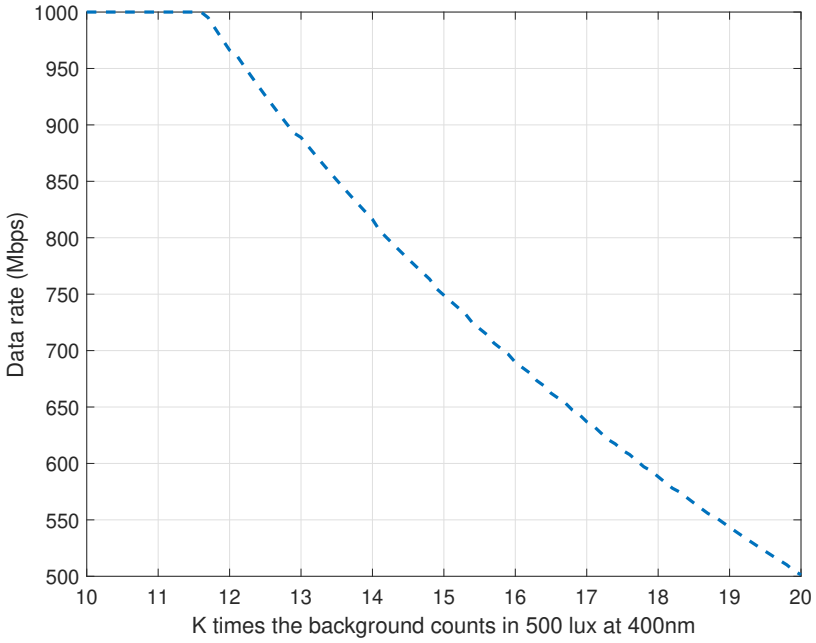


Figure 6.9: The data rate can be achieved by S13360-6025CS to get the target BER of 10^{-3} at different background conditions using OOK. The x-axis refers to the K times the averaged background counts generated in the 500 lux ambient light condition at a wavelength of 400 nm.

6.6 Potential of supporting M-PAM

Section 6.5 shows that the 1 Gbps data rate can be achieved using the SPAD-based receiver using OOK. Results in chapter 5 suggest that the higher order modulation scheme can be used to further push the data rate in a bandwidth limited channel. Based on the Poisson distribution, the BER for M-PAM can be expressed as

$$BER = \frac{1}{M \times log_2 M} \times \sum_{n=1}^{M-1} \left(\sum_{k=th_n+1}^{\infty} \frac{{N_{n-1}}^k}{k!} e^{-N_{n-1}} + \sum_{k=0}^{k=th_n} \frac{{N_n}^k}{k!} e^{-N_n} \right) \tag{6.10}$$

where M is the total number of PAM levels, N_{n-1} and N_n are the number of photons per symbol within symbol levels $level_{n-1}$ and $level_n$, and th_n is the optimum decision threshold between $level_{n-1}$ and $level_n$. Figure 6.10 shows the number of

SPADs required to generate the highest PAM symbol level to achieve a BER of 10^{-3} at different detected background counts per symbol calculated based on equation (6.10).

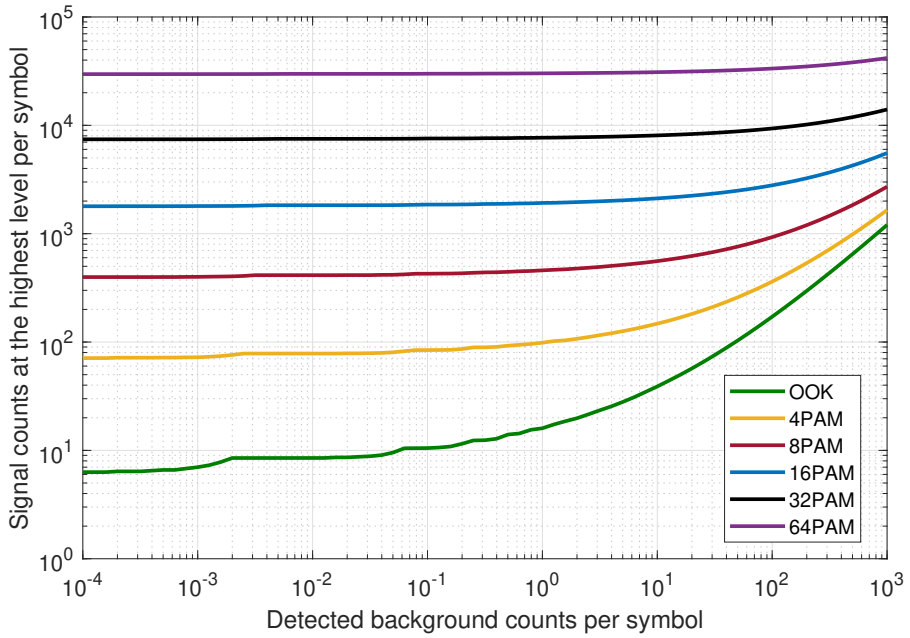


Figure 6.10: The highest signal level for different levels of PAM.

Figure 6.11 shows the operating range of the S13360-6025CS at 1 ns symbol time which is calculated based on equation (5.20). This result suggests that the maximum number of SPADs can be fired within 1 ns symbol time is approximately 700 for S13360-6025CS. For the purpose of using S13360-6025CS to support M-PAM at the 1 ns symbol time, the highest symbol level of M-PAM has to be within the operating range of S13360-6025CS. Result in figure 6.10 suggests that this device is unable to support 16-PAM, 32-PAM, and 64-PAM.

The feasibility of using the S13360-6025CS based receiver to support 4-PAM or 8-PAM at 1 ns symbol time is determined by the number of detected background counts per symbol. The method used to calculate the detected background counts per symbol is shown in figure 6.12. The method in figure 6.12 is the same as the method in figure 6.3 except the third step uses equation (6.10) to calculate N_s and the last step is to calculate the background counts with the effective PDP. Figure 6.13 shows the

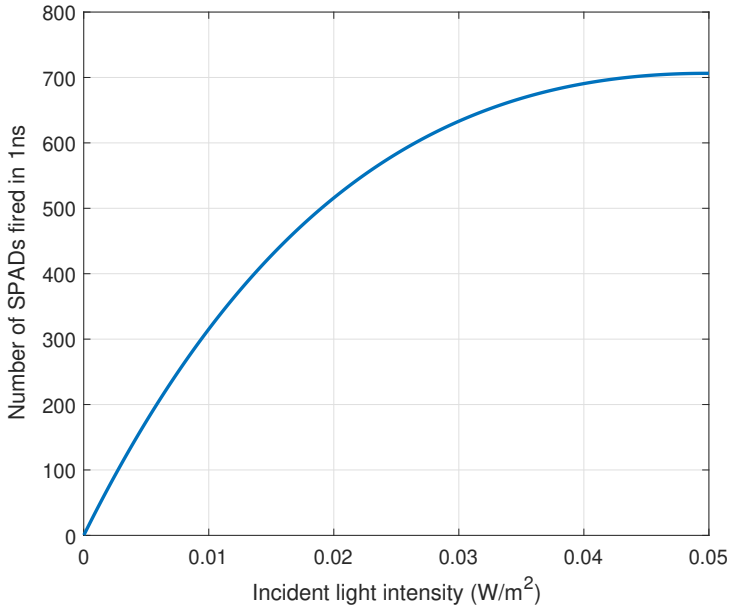


Figure 6.11: Operating range of S13360-6025CS.

detected background counts using S13360-6025CS based receiver at 1 ns symbol time with different ambient light conditions when 4-PAM is applied. Since the effective PDP decreases with the increase of incident background counts, the increment of the detected background counts per symbol is less than the increment of incident background counts. The pulse time of S13360-6025CS is 6 ns. At the 1 ns symbol time, the power penalty required to overcome the ISI is approximately 2.5 calculated by equation (6.6) and (6.7). Therefore, to reserve enough SPADs for compensating ISI, the signal counts per symbol required for generating the highest 4-PAM symbol without considering ISI penalty has to be less than 280 (700/2.5) counts per symbol. The results in figure 6.10 show that the corresponding detected background counts per symbol have to be less than 62 counts per symbol. From figure 6.13, it can be seen that the S13360-6025CS based receiver is capable of supporting 4-PAM and hence a 2 Gbps data rate when the background counts are less than 2.9 times the background counts generated by the 500 lux lighting condition at a wavelength of 400 nm.

Results in figure 6.10 show that, at very low ambient light condition which only

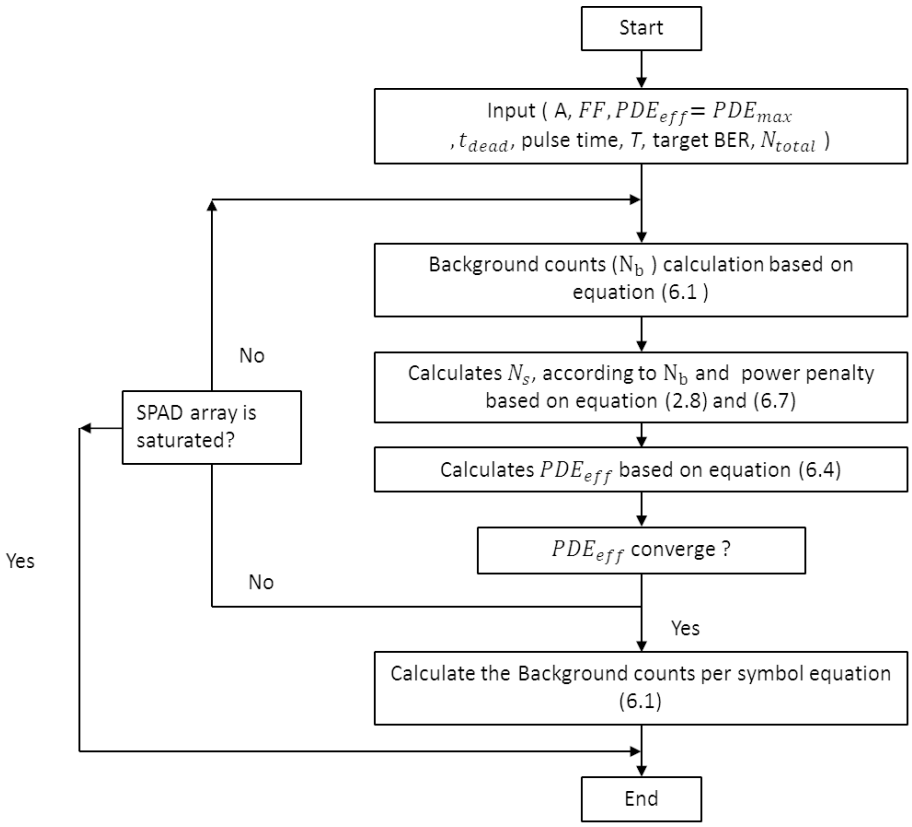


Figure 6.12: The method used to estimate background counts per symbol detected by a particular SPAD array.

generates 10^{-4} background counts per symbol, the number of signal counts required for generating the highest signal level for 8 PAM is 400 counts. Compare to 4-PAM, 8-PAM uses more symbol levels in the transmission. As a result, at the 1 ns symbol time, the ISI will become more significant than 4-PAM, and hence the power penalty required by 8-PAM has to be higher than 4-PAM. Even with the same power penalty required by 4-PAM, at the very low background counts condition, 8 PAM still requires 1000 SPADs to generate the highest symbol level, which has already exceeded the operating range of S13360-6025CS. Therefore, the S13360-6025CS is not capable of supporting 8 PAM at 1 ns symbol time in the typical ambient light condition.

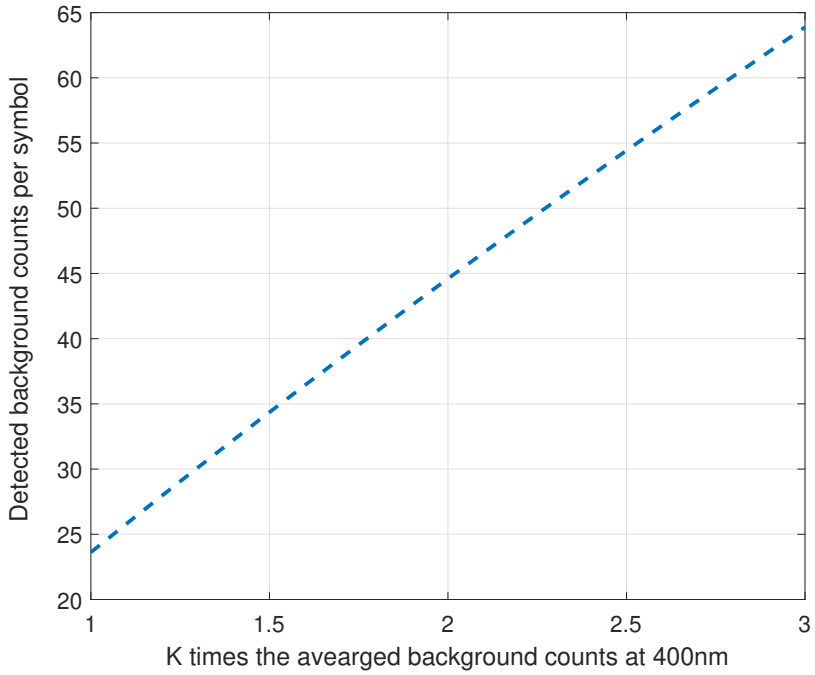


Figure 6.13: The number of background counts per symbol detected by S13360-6025CS at different background conditions using 4-PAM. The x-axis refers to the K times the averaged background counts generated in the 500 lux ambient light condition at a wavelength of 400 nm.

6.7 Summary

Due to the low PDE, the tested MPPC module (C11209-110) is not the optimum choice for implementing a high-speed VLC receiver. In this chapter, a general method for estimating the signal intensity required by a particular SPAD array to achieve a given BER under a given ambient light condition has been proposed.

Based on this method, a list of commercially available SPAD arrays which have higher PDE than C11209-110 are accessed. The estimation result suggests that the desired SPAD array for implementing high-speed VLC receiver should have a large active area, low pulse time, higher PDP, a large number of SPADs and short dead time. At the moment, the SPAD array S13360-6025CS is the optimum choice for the high-speed reliable VLC using OOK modulation.

Based on equation (4.18), it is estimated that the SPAD array S13360-6025CS is

3 times more sensitive than the typical APDs.

Moreover, the larger operating range makes S13360-6025CS potentially suitable for implementing higher order modulation. Estimation results show that S13360-6025CS is capable of supporting 4-PAM and hence the data rate of S13360-6025CS can be pushed to 2 Gbps until the background counts is more than 2.9 times the background counts generated by the typical ambient light condition at a wavelength of 400 nm. Therefore, the SPAD-based receiver is anticipated to support the Gbps data rate with a higher sensitivity than the APDs in the typical ambient light condition.

Chapter 7

Conclusion and Future work

7.1 Conclusion

In summary, the work discussed in this dissertation explores an appropriate SPAD array design guidelines for making the SPAD-based VLC receiver superior to the APD-based VLC receiver in the typical indoor environment. There is a special focus on developing analytical models to estimate the impact of the dead time, active area, PDE and background counts on the SPAD-based receiver, figuring out an efficient way of using the SPAD-based receiver to support 4-PAM, and investigating the feasibility of using currently available SPAD array to support Gbps data rate within the typical indoor ambient light condition.

A SPAD-based VLC receiver is anticipated to be more sensitive than an APD-based VLC receiver. However, the sensitivity of the current SPAD array is limited by the dead time, small active area, low fill-factor and the background counts. Through testing a small active quenched SPAD array with variable dead time, an analytical model based on the dead time, active area, PDE, dark counts, and the incident light intensity has been built to estimate the output response from an active quenched SPAD array. The OOK link results from this small array show that when this small

SPAD array is used in a VLC receiver, after EQ, the receiver only requires 1.57 times more photons than the Poisson limit. When only the detected photons per bit are considered, this small SPAD array requires 33 times fewer detected photons per bit than a typical APD. However, because the active area of the tested small SPAD array is 640 times smaller than the tested typical APD, the small SPAD array requires 160 times more incident photons per bit than the tested APD. This result suggests that a larger SPAD array has the potential to match the typical APD's performance.

At present, there are two widely used analytical models, the Gaussian model, and the Poisson model, for estimating the BER performance. Through testing the small SPAD array, the accuracy of using the two models are tested. Result suggests that the Poisson model is more accurate than the Gaussian model, and the Gaussian model is a good approximation to the Poisson model when the background counts per bit are higher than 2 counts per bit. This result suggests that the Q parameter can be used to accurately estimate the BER performance of the SPAD-based receiver when the background counts per bit are higher than 2 counts per bit.

The performance of a larger SPAD array has been tested by a commercially available large SPAD array (MPPC module C11209-110). The tested MPPC module includes a passive quenched SPAD array. There are two modes to process the output signal from the MPPC module. At low light levels, the output signals from the MPPC module are discrete pulses and hence the number of detected photons can be counted by counting pulses. Three photon counting methods, the peak counting method, the summation method, and the edge counting method have been compared. The result shows that the summation method is the optimum pulse counting method in the photon counting mode. When the incident light level is high enough, the pulses becomes indistinguishable. In this case, the analogue mode is preferred. The OOK link performance based on the photon counting mode and the analogue mode has been compared. Result suggests that the analogue mode is better when the data rate

is higher than 25 Mbps.

Based on the analogue mode, the sensitivity of the tested MPPC module at 100 Mbps has been tested both in the dark and in the typical indoor lighting environment (500 lux). Results show that the tested MPPC module is more sensitive than the conventional APD in the dark environment. However, due to the low PDE (8%) of this particular MPPC module, the tested MPPC module is still worse than the APD in the typical indoor lighting environment. In order to match the APD's sensitivity, the PDE of the tested MPPC has to be improved. Based on the Q parameter ratio between the SPAD array and the APD, the criterion (equation (4.18)) that determines when the SPAD array is more sensitive than the APD in the typical indoor environment has been presented. This criterion can be used as a guideline for designing or selecting a SPAD array that is more sensitive than a given APD in the typical indoor environment. Using this criterion and considering the power penalty required by the tested MPPC module to compensate ISI and additional noise, it is estimated that the tested MPPC module requires a PDE of 14.3% to match the sensitivity of the tested APD in the typical indoor ambient light condition. A newly released MPPC has already achieved a maximum PDE of 40%. It is estimated that a receiver using a SPAD array with a 40% PDE is anticipated to be significantly more sensitive than the typical APD-based receiver.

PAM is one of the most popular modulation schemes in VLC systems due to the simplicity in the transmitter and receiver design. The efficient way of using the SPAD-based receiver to support 4-PAM has been investigated. Based on ideal Poisson distribution, the optimum strategy to set the 4-PAM symbol levels has been investigated. Simulation results suggest that setting the 4-PAM symbol levels based on errors evenly distributed between the pairs of symbol levels is the optimum strategy in practical 4-PAM design. Based on this optimum strategy, the difference between using Gaussian model and Poisson model to estimate 4-PAM symbol levels has been

analysed. Results suggest that the Gaussian model is a good approximation to the Poisson model for 4-PAM when the background counts per symbol is higher than 2 counts per symbol. However, the output signal from the tested MPPC module (C11209-110) is neither perfect Poisson distribution nor Gaussian distribution. An accurate model (equation (5.9) and (5.10)) for estimating the required power levels for 4-PAM using the tested MPPC module has therefore been proposed. The accuracy of this model is tested at a data rate of 2 Mbps. The result shows that the measured symbol levels are within 2% of the levels estimated using this accurate model.

The 2 Mbps is useful for the low data rate VLC applications but not suitable for high-speed VLC applications. The OOK measurement result suggests that the ISI is tolerable when the symbol time is 10 ns. Therefore, a 200 Mbps data rate was tested. To check the feasibility of supporting the 200 Mbps 4-PAM using the tested MPPC module, the operating range of that module has been measured. Four empirical dead time models have been tested to fit the measured non-linear response of the tested MPPC module. Results show that both the paralyzable dead time model and the hybrid dead time model fit the measured non-saturated response of the tested MPPC module. Due to the VLC application only interests the non-saturated region, for simplicity, the paralyzable dead time model can be used to replace the hybrid dead time model to estimate the operating range of the passive quenched SPAD array. The power penalty required by the tested MPPC module to compensate ISI within 4-PAM symbol using DFE is estimated by a simple method which assuming the SPAD array within the tested MPPC module is a first order roll off low pass filter. Combining the estimated signal counts required to generated the highest 4-PAM symbol and the estimated power penalty, result shows that the operating range of the tested MPPC module is sufficient for supporting 200 Mbps 4-PAM. Despite the significant ISI within the system, a data rate of 200 Mbps has been achieved with a sensitivity of 43 photons per bit in the dark and 177 photons per bit in the 500 lux ambient

light condition. These results demonstrate the potential of using PAM to implement high-speed VLC link with a SPAD-based receiver. Additionally, results suggest that the power penalty required to support DFE to compensate ISI can be estimated using a simple method that assumes the response of the SPAD array is a first order roll-off low-pass filter.

The tested MPPC module (C11209-110) is not the optimum choice for implementing a high-speed VLC receiver because of its low PDE. SPAD arrays with higher PDE are now available. Based on the understanding of using the SPAD array as the VLC receiver, a method for estimating the sensitivity of a particular SPAD array at a given target BER under a given ambient light condition has been proposed. Using this method, a list of SPAD arrays with higher PDE than the C11209-110 has been assessed. Estimation result suggests that, for implementing high-speed VLC receiver, the desired SPAD array should have a large active area, short pulse time, high PDP, small dead time and a large number of SPADs. In a list of newly released SPAD arrays, the SPAD array S13360-6025CS is the optimum choice to achieve a data rate of 1 Gbps using OOK which is expected to have a sensitivity 3 times higher than the typical APDs in the typical indoor environment. Moreover, it is predicted that the S13360-6025CS is capable of supporting 4-PAM and hence the data rate of using S13360-6025CS can be pushed to 2 Gbps when the background counts are less than 2.9 times the background counts generated by the typical indoor ambient light condition at a wavelength of 400 nm. Therefore, a receiver based on the SPAD array has the potential to support Gbps data rate with a higher sensitivity than the typical APDs in the normal indoor environment.

7.2 Future Work

The SPAD-based receiver offers a promising future for the indoor VLC. The advantages of the SPAD-based receiver with respect to sensitivity, cost, and flexibility will continuously inspire more research interest in the area. As technology moves forward, increasing attention is received and more sensitive SPAD-based receiver will be discovered.

In this project, the effect of active area, pulse time, PDE, dead time, number of SPADs and background counts has been investigated using the available devices at the time. This investigation proposed a method for estimating the sensitivity of a given SPAD array at a given ambient light condition. At the end of this project, the sensitivities of a list of newly released SPAD arrays at Gbps data rate under the typical indoor ambient light condition have been predicted using the proposed method. The estimated sensitivities of those newly released SPAD arrays have to be experimentally confirmed with suitable equipment (fast AWG, appropriate light source, the SPAD arrays mentioned in Appendix B, appropriate optic filters, etc). Once the estimated result is confirmed, with the optimum SPAD array, a more advanced SPAD-based VLC link can be built and demonstrated in the future.

Further work on improving the sensitivity of the SPAD-based receiver can be done by combining the SPAD-based receiver with the fluorescent concentrator. At present, the small collection area of the SPAD array limits the sensitivity of the SPAD-based receiver. The fluorescent concentrator can absorb the incident light over a large collection area and concentrate the re-emitted light to its thin edge at a different wavelength [71,72]. By placing the SPAD array at the edge of the fluorescent concentrator, the collection area of the SPAD-based receiver can be significantly improved and hence the receiver sensitivity. Meanwhile, the fluorescent concentrator also increases the FOV of the detector and thus enhance the mobility of the SPAD-based receiver [73, 74]. Therefore, the performance of the SPAD-based receiver incorporat-

ing the fluorescent concentrator can be very attractive. However, the increased FOV will potentially bring more background counts from the ambient light. To address this challenge, the analytical model developed in this thesis has to be extended model to take the effect of the fluorescent concentrator into account in the future. With appropriate equipment, this extended is required to be confirmed through experiment. The validated new model will be used to investigate the optimum operation condition and determine the design guidelines for this new type of VLC receiver. Based on the proposed guidelines, a simple, fast, sensitive, low cost and easy-aligned VLC receiver will be developed. This new type of VLC receiver will significantly increase the opportunity for the VLC system to play a substantial role in the future indoor wireless network.

Additional research can be carried out focusing on applying the SPAD-based receiver to other applications such as underwater VLC, fiber-optic communication, and deep space optical communication, which also require highly sensitive receivers [43, 75, 76]. The appropriate design guideline for making the SPAD-based receiver to achieve the highest sensitivity within those applications is worthy of investigating.

Appendix A: Q_{APD} and Q_{SPAD} calculation

$$Q_{APD} = \frac{m.R.P_s}{\sqrt{2e.\left(R.\left(P_b + P_s\right)\right).bw.m^{x+2}} + \sqrt{2e.\left(R.P_b\right).bw.m^{x+2}}} \tag{1}$$

$$Q_{APD} = \frac{P_s.\sqrt{\frac{R}{m^x}}}{\sqrt{2e.bw}(\sqrt{(P_S + P_B)} + \sqrt{(P_B)})} \tag{2}$$

According to [77]

$$R = \frac{QE.\lambda}{1240} \tag{3}$$

$$Q_{APD} = \frac{P_s\sqrt{\frac{QE.\lambda}{1240.m^x}}}{\sqrt{2e.bw}.(\sqrt{(P_S + P_B)} + \sqrt{(P_B)})} \tag{4}$$

$$P_S = Int_S A_{APD} \tag{5}$$

$$P_b = Int_b A_{APD} \tag{6}$$

$$Q_{APD} = \frac{Int_S A_{APD}\sqrt{\frac{QE.\lambda}{1240.m^x}}}{\sqrt{2e.bw.A_{APD}}(\sqrt{(Int_S + Int_b)} + \sqrt{(Int_b)})} \tag{7}$$

$$Q_{APD} = \frac{Int_S\sqrt{\frac{QE.\lambda.A_{APD}}{1240.m^x}}}{\sqrt{2e.bw}(\sqrt{(Int_S + Int_b)} + \sqrt{(Int_b)})} \tag{8}$$

$$Q_{SPAD} = \frac{N_S}{\sqrt{N_S + N_B} + \sqrt{N_B}} \tag{9}$$

$$Q_{SPAD} = \frac{\frac{PDP.P_S.T}{E_{single_{photon}}}}{\sqrt{\frac{PDP.T(P_S+P_B)}{E_{single_{photon}}}} + \sqrt{\frac{PDP.T.P_B}{E_{single_{photon}}}}} \tag{10}$$

$$Q_{SPAD} = \frac{\frac{P_S.PDP.T}{E_{single_{photon}}}}{\sqrt{\frac{PDP.T}{E_{single_{photon}}}} * (\sqrt{(P_S+P_B)} + \sqrt{(P_B)})} = \frac{P_S.\sqrt{\frac{PDP.T}{E_{single_{photon}}}}}{\sqrt{(P_S+P_B)} + \sqrt{(P_B)}} \tag{11}$$

$$T = \frac{1}{2.bw} \tag{12}$$

$$Q_{SPAD} = \frac{P_S.\sqrt{PDP}}{\sqrt{2.bw.E_{single_{photon}}}.(\sqrt{(P_S+P_B)} + \sqrt{(P_B)})} \tag{13}$$

$$E_{single_{photon}} = \frac{1240}{\lambda}e \tag{14}$$

$$Q_{SPAD} = \frac{P_S.\sqrt{PDP}}{\sqrt{\frac{1240}{\lambda}.e.2.bw}.(\sqrt{(P_S+P_B)} + \sqrt{(P_B)})} \tag{15}$$

$$P_S = Int_S.A_{SPAD}.FF \tag{16}$$

$$P_b = Int_b.A_{SPAD}.FF \tag{17}$$

$$Q_{SPAD} = \frac{Int_S.\sqrt{PDP.A_{SPAD}.FF}}{\sqrt{\frac{1240}{\lambda}.e.2.bw}.(\sqrt{(Int_S+Int_b)} + \sqrt{(Int_b)})} \tag{18}$$

$$Q_{SPAD} = \frac{Int_S.\sqrt{PDE.A_{SPAD}}}{\sqrt{\frac{1240}{\lambda}.e.2bw}.(\sqrt{(Int_S+Int_b)} + \sqrt{(Int_b)})} \tag{19}$$

$$Q_{SPAD} = \frac{Int_S.\sqrt{\frac{PDE.\lambda.A_{SPAD}}{1240}}}{\sqrt{2ebw}.(\sqrt{(Int_S + Int_b)} + \sqrt{(Int_b)})} \tag{20}$$

Appendix B: A list of newly released SPAD arrays

Product Number	Dead time (ns)	Number of SPADs	Pulse time (ns)	PDE ~400 nm	FF	Active Area (mm^2)	DCR per mm^2
SensL B series 10010	19	2880	1	0.18	0.28	1	7.00E+05
SensL B series 10020	94	1296	1	0.31	0.48	1	7.00E+05
SensL B series 60036	411	18980	3.2	0.41	0.64	36	5.97E+05
S13360 1325CS	30	2668	6	0.25	0.47	1.69	4.14E+04
S13360 1350CS	62	667	12	0.40	0.74	1.69	5.33E+04
S13360 3050CS	62	3600	12	0.40	0.74	9	5.56E+04
S13360 3025CS	30	14400	6	0.25	0.47	9	4.44E+04
S13360 6050CS	62	14400	12	0.40	0.74	36	5.56E+04
S13360 1375CS	73	285	15	0.50	0.82	1.69	5.33E+04
S13360 3075CS	69	1600	13.8	0.50	0.82	9	5.56E+04
S13360 6025CS	30	57600	6	0.25	0.47	36	4.44E+04
S13360 6075CS	69	6400	13.8	0.50	0.82	36	5.56E+04
PM3315-WB	42	38800	8.4	0.31	0.82	9	1.00E+05

Table 1: A list of newly released SPAD arrays with better PDE than the tested MPPC. (*SensL B series has been obscured by the manufacturer recently) [78–80]

Appendix C: Effective PDE calculation

The effective PDE is given by

$$PDE_{eff} = \frac{N_{out_total}}{N_{incident}} \tag{21}$$

$$N_{out_total} = N_{SPADs} \times T \times \lambda_{in} e^{-\lambda_{in} \times t_{dead}} \tag{22}$$

$$\lambda_{in} = \frac{L \times A_SPAD_t \times PDE_{\max}}{E_p} \tag{23}$$

where A_SPAD_t refers to the total area of a single SPAD within the SPAD array.

$$N_{incident} = \frac{L \times A_SPAD_t \times N_{SPADs} \times T}{E_p} \tag{24}$$

$$PDE_{eff} = PDE_{\max} e^{-\lambda_{in} \times t_{dead}} \tag{25}$$

The average number of SPADs fired within a bit period at bit one can be calculated as

$$N_s = N_{SPADs} \times T \times \lambda_{in} \tag{26}$$

Therefore,

$$\lambda_{in} = \frac{N_s}{N_{SPADs} \times T} \tag{27}$$

Moreover,

$$\lambda_{in} = \frac{1}{t_{\mathrm{in}terphoton}} \tag{28}$$

where $t_{\mathrm{inter}photon}$ refers to the inter photon time.

let

$$x = \lambda_{in} \times t_{dead} \tag{29}$$

then

$$PDE_{eff} = PDE_{\max} e^{-x} \tag{30}$$

where

$$x = \frac{t_{dead}}{t_{\mathrm{inter}photon}} = \frac{t_{dead} \times N_s}{N_{SPADs} \times T} \tag{31}$$

References

[1] Cisco, "Cisco White Paper Global Mobile Data Traffic Forecast." https://www.cisco.com/c/en/us/solutions/collateral/service-provider/visual-networking-index-vni/white-paper-c11-741490.html,2017.

[2] Ericsson, "Ericsson Mobility Report." https://www.ericsson.com/en/mobility-report/reports,2018.

[3] Nokia, "Nokia White paper looking ahead to 5G." http://www.5gamericas.org/files/3614/3898/6583/Nokia_White_Paper_Looking_ahead_to_5G.pdf,2018.

[4] S. Dimitrov and H. Haas, *Principles of LED light communications: towards networked Li-Fi*. Cambridge University Press, 2015.

[5] D. Karunatilaka, F. Zafar, V. Kalavally, and R. Parthiban, "Led based indoor visible light communications: State of the art.," *IEEE communications surveys and tutorials*, vol. 17, no. 3, pp. 1649–1678, 2015.

[6] S. Arnon, *Visible light communication*. Cambridge University Press, 2015.

[7] Z. Wang, Q. Wang, W. Huang, and Z. Xu, *Visible Light Communications: Modulation and Signal Processing*. John Wiley & Sons, 2017.

[8] Z. Ghassemlooy, L. N. Alves, S. Zvanovec, and M.-A. Khalighi, *Visible light communications: theory and applications*. CRC Press, 2017.

[9] D. Tsonev, H. Chun, S. Rajbhandari, J. J. McKendry, S. Videv, E. Gu, M. Haji, S. Watson, A. E. Kelly, G. Faulkner, *et al.*, "A 3-gb/s single-led ofdm-based wireless vlc link using a gallium nitride μled," *IEEE Photon. Technol. Lett.*, vol. 26, no. 7, pp. 637–640, 2014.

[10] R. X. Ferreira, E. Xie, J. J. McKendry, S. Rajbhandari, H. Chun, G. Faulkner, S. Watson, A. E. Kelly, E. Gu, R. V. Penty, *et al.*, "High bandwidth gan-based micro-leds for multi-gb/s visible light communications," *IEEE Photonics Technology Letters*, vol. 28, no. 19, pp. 2023–2026, 2016.

[11] X. Li, N. Bamiedakis, X. Guo, J. McKendry, E. Xie, R. Ferreira, E. Gu, M. Dawson, R. Penty, and I. H. White, "Wireless visible light communications employing feed-forward pre-equalization and pam-4 modulation," *Journal of Lightwave Technology*, vol. 34, no. 8, pp. 2049–2055, 2016.

[12] N. Chi, H. Haas, M. Kavehrad, T. D. Little, and X.-L. Huang, "Visible light communications: demand factors, benefits and opportunities [guest editorial]," *IEEE Wireless Communications*, vol. 22, no. 2, pp. 5–7, 2015.

[13] H. Elgala, R. Mesleh, and H. Haas, "Indoor optical wireless communication: potential and state-of-the-art," *IEEE Communications Magazine*, vol. 49, no. 9, 2011.

[14] S. Rajbhandari, H. Chun, G. E. Faulkner, K. L. Cameron, A. V. Jalajakumari, R. K. Henderson, D. Tsonev, M. Ijaz, Z. Chen, H. Haas, *et al.*, "High-speed integrated visible light communication system: Device constraints and design considerations.," *IEEE Journal on Selected Areas in Communications*, vol. 33, no. 9, pp. 1750–1757, 2015.

[15] G. P. Agrawal, *Fiber-optic communication systems*, vol. 222. John Wiley & Sons, 2012.

[16] D. Renker, "New trends on photodetectors," *Nuclear Instruments and Methods in Physics Research Section A: Accelerators, Spectrometers, Detectors and Associated Equipment*, vol. 571, no. 1-2, pp. 1–6, 2007.

[17] D. Renker, "Geiger-mode avalanche photodiodes, history, properties and problems," *Nuclear Instruments and Methods in Physics Research Section A: Accelerators, Spectrometers, Detectors and Associated Equipment*, vol. 567, no. 1, pp. 48–56, 2006.

[18] J. M. Kahn, R. You, P. Djahani, A. G. Weisbin, B. K. Teik, and A. Tang, "Imaging diversity receivers for high-speed infrared wireless communication," *IEEE Communications Magazine*, vol. 36, no. 12, pp. 88–94, 1998.

[19] J. B. Carruthers, "Wireless infrared communications," *Wiley Encyclopedia of Telecommunications*, 2003.

[20] Z. Ghassemlooy, W. Popoola, and S. Rajbhandari, *Optical wireless communications: system and channel modelling with Matlab®*. CRC press, 2012.

[21] J. G. Proakis, *Digital communications*. McGraw-Hill, New York, 2007.

[22] D. Chitnis and S. Collins, "A spad-based photon detecting system for optical communications," *Journal of Lightwave Technology*, vol. 32, no. 10, pp. 2028–2034, 2014.

[23] D. Chitins, *Thesis: Single Photon Avalanche Diodes for Optical Communications*. University of Oxford, 2012.

[24] D. Hall, Y.-H. Liu, L. Yan, Y. Yu, and Y.-H. Lo, "Approaching the quantum limit of photodetection in solid-state photodetectors," *IEEE Transactions on Electron Devices*, vol. 64, no. 12, pp. 4812–4822, 2017.

[25] E. Fisher, I. Underwood, and R. Henderson, "A reconfigurable single-photon-counting integrating receiver for optical communications," *IEEE J. Solid-State Circuits*, vol. 48, no. 7, pp. 1638–1650, 2013.

[26] I. Alsolami, *Thesis: Visible Light Communications with Single-Photon Avalanche Diodes*. University of Oxford, 2014.

[27] C. Bosio, S. Gentile, E. Kuznetsova, and F. Meddi, "Silicon photomultiplier light response properties," *Nuclear Science Symposium Conference Record, 2007. NSS'07. IEEE*, vol. 3, pp. 2097–2098, 2007.

[28] M. Vitali, D. Bronzi, A. J. Krmpot, S. N. Nikolić, F.-J. Schmitt, C. Junghans, S. Tisa, T. Friedrich, V. Vukojević, L. Terenius, *et al.*, "A single-photon avalanche camera for fluorescence lifetime imaging microscopy and correlation spectroscopy," *IEEE Journal of Selected Topics in Quantum Electronics*, vol. 20, no. 6, pp. 344–353, 2014.

[29] K. Ehrlich, H. Fleming, S. McAughtrie, A. Kufcsák, N. Krstajić, C. Campbell, R. Henderson, K. Dhaliwal, R. Thomson, and M. Tanner, "Time-resolved single photon spectroscopy through a single optical fibre for miniaturised medical probe design," in *Biophotonics: Photonic Solutions for Better Health Care VI*, vol. 10685, p. 106850Q, International Society for Optics and Photonics, 2018.

[30] D. Bronzi, F. Villa, S. Tisa, A. Tosi, F. Zappa, D. Durini, S. Weyers, and W. Brockherde, "100 000 frames/s 64× 32 single-photon detector array for 2-d imaging and 3-d ranging," *IEEE journal of selected topics in quantum electronics*, vol. 20, no. 6, pp. 354–363, 2014.

[31] D. Bronzi, F. Villa, S. Tisa, A. Tosi, and F. Zappa, "Spad figures of merit for photon-counting, photon-timing, and imaging applications: A review," *IEEE Sensors Journal*, vol. 16, no. 1, pp. 3–12, 2016.

[32] S. Ito, S. Hiratsuka, M. Ohta, H. Matsubara, and M. Ogawa, "Spad dcnn: Localization with small imaging lidar and dcnn," in *Intelligent Robots and Systems (IROS), 2017 IEEE/RSJ International Conference on*, pp. 3312–3317, IEEE, 2017.

[33] SensL, "An Introduction to the Silicon Photomultiplier." http://www.sensl.com/downloads/ds/TN%20-%20Intro%20to%20SPM%20Tech.pdf,2011.

[34] B. Nabet, *Photodetectors: Materials, Devices and Applications*. Woodhead Publishing, 2015.

[35] R. J. Walker, E. A. Webster, J. Li, N. Massari, and R. K. Henderson, "High fill factor digital silicon photomultiplier structures in 130nm cmos imaging technology," in *Nuclear Science Symposium and Medical Imaging Conference (NSS/MIC), 2012 IEEE*, pp. 1945–1948, IEEE, 2012.

[36] E. Sarbazi and H. Haas, "Detection statistics and error performance of spad-based optical receivers," in *Personal, Indoor, and Mobile Radio Communications (PIMRC), 2015 IEEE 26th Annual International Symposium on*, pp. 830–834, IEEE, 2015.

[37] E. Sarbazi, M. Safari, and H. Haas, "Statistical modeling of single-photon avalanche diode receivers for optical wireless communications," *IEEE Transactions on Communications*, 2018.

[38] E. Sarbazi, M. Safari, and H. Haas, "Photon detection characteristics and error performance of spad array optical receivers.," in *IWOW*, pp. 132–136, 2015.

[39] Y. Li, M. Safari, R. Henderson, and H. Haas, "Optical ofdm with single-photon avalanche diode," *IEEE Photon. Technol. Lett.*, vol. 27, no. 9, pp. 943–946, 2015.

[40] Y. Li, S. Videv, M. Abdallah, K. Qaraqe, M. Uysal, and H. Haas, "Single photon avalanche diode (spad) vlc system and application to downhole monitoring," in *Global Communications Conference (GLOBECOM), 2014 IEEE*, pp. 2108–2113, IEEE, 2014.

[41] C. Wang, H.-Y. Yu, and Y.-J. Zhu, "A long distance underwater visible light communication system with single photon avalanche diode," *IEEE Photonics Journal*, vol. 8, no. 5, pp. 1–11, 2016.

[42] M.-A. Khalighi, T. Hamza, S. Bourennane, P. Léon, and J. Opderbecke, "Underwater wireless optical communications using silicon photo-multipliers," *IEEE Photonics Journal*, vol. 9, no. 4, pp. 1–10, 2017.

[43] T. Hamza, M.-A. Khalighi, S. Bourennane, P. Leon, and J. Opderbecke, "On the suitability of employing silicon photomultipliers for underwater wireless optical communication links," in *Communication Systems, Networks and Digital Signal Processing (CSNDSP), 2016 10th International Symposium on*, pp. 1–5, IEEE, 2016.

[44] D. Chitnis, L. Zhang, H. Chun, S. Rajbhandari, G. Faulkner, D. O'Brien, and S. Collins, "A 200 mb/s vlc demonstration with a spad based receiver," in *Summer Topicals Meeting Series (SUM), 2015*, pp. 226–227, IEEE, 2015.

[45] O. Almer, D. Tsonev, N. A. Dutton, T. Al Abbas, S. Videv, S. Gnecchi, H. Haas, and R. K. Henderson, "A spad-based visible light communications receiver employing higher order modulation," in *Global Communications Conference (GLOBECOM), 2015 IEEE*, pp. 1–6, IEEE, 2015.

[46] J. Kosman, O. Almer, A. V. Jalajakumari, S. Videv, H. Haas, and R. K. Henderson, "60 mb/s, 2 meters visible light communications in 1 klx ambient using

an unlensed cmos spad receiver," in *Photonics Society Summer Topical Meeting Series (SUM), 2016 IEEE*, pp. 171–172, IEEE, 2016.

[47] C. Wang, H.-Y. Yu, Y.-J. Zhu, T. Wang, and Y.-W. Ji, "Experimental study on spad-based vlc systems with an led status indicator," *Optics Express*, vol. 25, no. 23, pp. 28783–28793, 2017.

[48] E. F. Schubert, *Light-emitting diodes*. E. Fred Schubert, 2018.

[49] J. Litvik, J. Dubovan, D. Benedikovic, and M. Kuba, "Impact of impulse response of avalanche photodiode to eye-closure penalty," in *Telecommunications and Signal Processing (TSP), 2015 38th International Conference on*, pp. 1–4, IEEE, 2015.

[50] S. Cova, M. Ghioni, A. Lacaita, C. Samori, and F. Zappa, "Avalanche photodiodes and quenching circuits for single-photon detection," *Applied optics*, vol. 35, no. 12, pp. 1956–1976, 1996.

[51] S. Gnecchi, N. A. Dutton, L. Parmesan, B. R. Rae, S. Pellegrini, S. J. McLeod, L. A. Grant, and R. K. Henderson, "Analysis of photon detection efficiency and dynamic range in spad-based visible light receivers," *Journal of Lightwave Technology*, vol. 34, no. 11, pp. 2774–2781, 2016.

[52] S. Karlin, *A first course in stochastic processes*. Academic press, 2014.

[53] Hamamatsu, "Datasheet of MPPC S12571-010C/-015C." https://www.hamamatsu.com/resources/pdf/ssd/s12571-010_etc_kapd1044e.pdf,2015.

[54] Hamamatsu, "Datasheet of MPPC C11209-110." https://www.hamamatsu.com/resources/pdf/ssd/c11209-110_kacc1211e.pdf,2014.

[55] Hamamatsu, "MPPC technical note." https://www.hamamatsu.com/resources/pdf/ssd/mppc_kapd9005e.pdf,2017.

[56] F. Zappa, S. Tisa, A. Tosi, and S. Cova, "Principles and features of single-photon avalanche diode arrays," *Sensors and Actuators A: Physical*, vol. 140, no. 1, pp. 103–112, 2007.

[57] R. W. Boyd, "Radiometry and the detection of optical radiation," *New York, John Wiley and Sons, 1983, 261 p.*, 1983.

[58] G. Zhang, C. Yu, C. Zhu, and L. Liu, "Feasibility study of multi-pixel photon counter serving as the detector in digital optical communications," *Optik-International Journal for Light and Electron Optics*, vol. 124, no. 22, pp. 5781–5786, 2013.

[59] NOAO, "Recommended Light Levels." https://www.noao.edu/education/QLTkit/ACTIVITY_Documents/Safety/LightLevels_outdoor+indoor.pdf, Dec. 2015.

[60] A. Jovicic, J. Li, and T. Richardson, "Visible light communication: opportunities, challenges and the path to market," *IEEE Communications Magazine*, vol. 51, no. 12, pp. 26–32, 2013.

[61] S. Rajagopal, R. D. Roberts, and S.-K. Lim, "Ieee 802.15. 7 visible light communication: modulation schemes and dimming support," *IEEE Communications Magazine*, vol. 50, no. 3, 2012.

[62] F. Delgado, I. Quintana, J. Rufo, J. Rabadan, C. Quintana, and R. Perez-Jimenez, "Design and implementation of an ethernet-vlc interface for broadcast transmissions," *IEEE communications letters*, vol. 14, no. 12, pp. 1089–1091, 2010.

[63] G. Giambene, *Resource management in satellite networks: optimization and cross-layer design*. Springer Science & Business Media, 2007.

[64] Y. Li, M. Safari, R. Henderson, and H. Haas, "Nonlinear distortion in spad-based optical ofdm systems," pp. 1–6, 2015.

[65] A. Eisele, R. Henderson, B. Schmidtke, T. Funk, L. Grant, J. Richardson, and W. Freude, "185 mhz count rate, 139 db dynamic range single-photon avalanche diode with active quenching circuit in 130 nm cmos technology," in *Proc. Int. Image Sensor Workshop*, pp. 278–280, 2011.

[66] S. H. Lee and R. P. Gardner, "A new g–m counter dead time model," *Applied Radiation and Isotopes*, vol. 53, no. 4-5, pp. 731–737, 2000.

[67] L. Neri, S. Tudisco, F. Musumeci, A. Scordino, G. Fallica, M. Mazzillo, and M. Zimbone, "Note: Dead time causes and correction method for single photon avalanche diode devices," *Review of Scientific Instruments*, vol. 81, no. 8, p. 086102, 2010.

[68] "Optical signal-to-noise ratio and the q-factor in fiber-optic communication systems," *Maxim application note HFAN*, vol. 9, no. 2, 2008.

[69] Y. You, W. Zhang, L. Sun, J. Du, C. Liang, F. Yang, and Z. He, "Time skewing and amplitude nonlinearity mitigation by feedback equalization for 56 gbps vcsel-based pam-4 links," *Optics Communications*, vol. 410, pp. 909–915, 2018.

[70] M. CONNER, "Light spectrum/spectrometer charts and raw data for common lights," recommendation, Designing with LEDs, Jul. 2015.

[71] P. P. Manousiadis, S. Rajbhandari, R. Mulyawan, D. A. Vithanage, H. Chun, G. Faulkner, D. C. OBrien, G. A. Turnbull, S. Collins, and I. D. Samuel, "Wide field-of-view fluorescent antenna for visible light communications beyond the étendue limit," *Optica*, vol. 3, no. 7, pp. 702–706, 2016.

[72] R. Mulyawan, H. Chun, A. Gomez, S. Rajbhandari, G. Faulkner, P. P. Manousiadis, D. A. Vithanage, G. A. Turnbull, I. D. Samuel, S. Collins, *et al.*, "Mimo visible light communications using a wide field-of-view fluorescent concentrator," *IEEE Photonics Technology Letters*, vol. 29, no. 3, pp. 306–309, 2017.

[73] S. Collins, D. C. OBrien, and A. Watt, "High gain, wide field of view concentrator for optical communications," *Optics letters*, vol. 39, no. 7, pp. 1756–1759, 2014.

[74] C. Quintana, H. Chun, R. Mulyawan, G. Faulkner, S. Collins, D. C. O'Brien, E. Xie, J. J. McKendry, E. Gu, M. D. Dawson, *et al.*, "Ultra-wide coverage vlc system with alignment-free receiver," in *LIFI Congress (GLC), 2018 Global*, pp. 1–4, IEEE, 2018.

[75] H. Hemmati, *Deep space optical communications*, vol. 11. John Wiley & Sons, 2006.

[76] H. Zimmermann, B. Steindl, M. Hofbauer, and R. Enne, "Integrated fiber optical receiver reducing the gap to the quantum limit," *Scientific Reports*, vol. 7, no. 1, p. 2652, 2017.

[77] A. Rogalski, K. Adamiec, and J. Rutkowski, *Narrow-gap semiconductor photodiodes*, vol. 77. SPIE Press, 2000.

[78] SensL, "B-Series Fast, Blue-Sensitive Silicon Photomultiplier Sensors." http://www.sensl.com/downloads/ds/DS-MicroBseries.pdf,2013.

[79] Hamamatsu, "Mppcs for precision measurement." https://www.hamamatsu.com/eu/en/product/optical-sensors/mppc/mppc_single/mppc_for-precision-measurement/index.html,2016.

[80] KETEK, "SiPM Silicon Photomultiplier." https://www.ketek.net/sipm,2017.